

PATTERN RECONFIGURABLE ANTENNA DESIGNS IN SUB-6 GHz BAND
FOR 5G APPLICATIONS

A THESIS SUBMITTED TO
THE GRADUATE SCHOOL OF NATURAL AND APPLIED SCIENCES
OF
MIDDLE EAST TECHNICAL UNIVERSITY

BY

FEZA TURGAY ÇELİK

IN PARTIAL FULFILLMENT OF THE REQUIREMENTS
FOR
THE DEGREE OF MASTER OF SCIENCE
IN
ELECTRICAL AND ELECTRONIC ENGINEERING

FEBRUARY 2021

Approval of the thesis:

**PATTERN RECONFIGURABLE ANTENNA DESIGNS IN SUB-6
GHz BAND FOR 5G APPLICATIONS**

submitted by **FEZA TURGAY ÇELİK** in partial fulfillment of the requirements for
the degree of **Master of Science in Electrical and Electronic Engineering, Middle
East Technical University** by,

Prof. Dr. Halil Kalıpçılar
Dean, Graduate School of **Natural and Applied Sciences**

Prof. Dr. İlkey Ulusoy
Head of the Department, **Electrical and Electronics Engineering**

Prof. Dr. Özlem Aydın Çivi
Supervisor, **Electrical and Electronics Engineering**

Assoc. Prof. Dr. Lale Alatan
Co-Supervisor, **Electrical and Electronics Engineering**

Examining Committee Members:

Prof. Dr. Sencer Koç
Electrical and Electronics Engineering, METU

Prof. Dr. Özlem Aydın Çivi
Electrical and Electronics Engineering, METU

Assoc. Prof. Dr. Lale Alatan
Electrical and Electronics Engineering, METU

Prof. Dr. Gülbin Dural
Electrical and Electronics Engineering, METU

Prof. Dr. Vakur B. Ertürk
Electrical and Electronics Engineering, Bilkent University

Date: 08.02.2021

I hereby declare that all information in this document has been obtained and presented in accordance with academic rules and ethical conduct. I also declare that, as required by these rules and conduct, I have fully cited and referenced all material and results that are not original to this work.

Name Last name : Feza Turgay Çelik

Signature :

ABSTRACT

PATTERN RECONFIGURABLE ANTENNA DESIGNS IN SUB-6 GHz BAND FOR 5G APPLICATIONS

Çelik, Feza Turgay
Master of Science, Electrical and Electronic Engineering
Supervisor : Prof. Dr. Özlem Aydın Çivi
Co-Supervisor: Assoc. Prof. Dr. Lale Alatan

February 2021, 126 pages

In this thesis, design, simulations, fabrication, and radiation pattern measurements of reconfigurable antennas for sub-6GHz application of 5G protocol are presented. Mode analysis techniques and array theory are employed to have an understanding of the pattern reconfigurability concept of the designs.

As a first step, a dual-fed rectangular patch antenna is designed, simulated, fabricated, and then measured. Even and odd mode definitions on the rectangular patch antennas are employed in the design process. Designed antenna has a shorting plane located at its middle section. This shorting plane divides the antenna into two sub-elements that are independent of each other. As each sub-element has its own excitation port, it is possible to scan the main radiation direction of the antenna by applying phase differences between the ports. Designed antenna scans from -40° to $+40^{\circ}$ in the elevation plane, which is orthogonal to shorting plane.

Another printed antenna is designed based on the excitation of different modes of different resonators. Circular patch and ring-shaped resonators are employed to

create different radiation patterns. The cavity model is used to analyze and design radiators. The radiators are arranged so that they operate at different modes of cavity model. The ring is fed by two ports opposite to each other while the circular patch is parasitically excited. The applied phase difference between ports determines which radiator is excited more dominantly. Designed antenna also performs beam scanning from -40° to $+40^{\circ}$ in the elevation plane along the feeding ports. To miniaturize, the antenna is loaded by capacitors. Antenna is fabricated, and design is validated by measurements.

A rectangular patch antenna that includes four triangular sub-antenna elements is designed. This antenna employs the parasitic elements to steer its radiation direction. However, the phenomenon that results in beam scanning is not limited to the contributions of the parasitic elements. As the antenna consists of four independently excited elements, operation with multiple elements also effectively steer the radiation beam. This design is capable of steering the radiated beam from -40° to $+40^{\circ}$ in elevation plane.

Keywords: Pattern Diversity, Multi-Mode Antennas, Pattern Reconfigurability, Antenna Miniaturization, Cavity Model Analysis

ÖZ

5G PROTOKOLÜNÜN 6 GHz ALTI BANDI İÇİN IŞIMA ÖRÜNTÜSÜ YAPILANDIRILABİLEN ANTEN TASARIMLARI

Çelik, Feza Turgay
Yüksek Lisans, Elektrik ve Elektronik Mühendisliği
Tez Yöneticisi: Prof. Dr. Özlem Aydın Çivi
Ortak Tez Yöneticisi: Doç. Dr. Lale Alatan

Şubat 2021, 126 sayfa

Bu tez çalışmasında 5G protokolünün 6 GHz altındaki frekans bandı için, ışıma örüntüsü çeşitlendirilebilen antenlerin tasarımı, benzetimi, üretimi ve ölçüm sonuçları incelenmiştir. Işıma örüntüsünde yapılandırılabilme anlayışı, kovuk modeli kullanılarak tetkik edilmiştir.

İki beslemeye sahip kare şeklindeki mikro şerit anten tasarlanmış, benzetim sonuçları incelenmiş, üretim ve ölçüm sonuçları sunulmuştur. Anten kare şeklinde bir mikroşerit anten olup, anten yüzeyinin ortasına topraklama plakası çekilmiştir. Topraklama plakası anteni birbirinden bağımsız iki parçaya ayırmıştır. Bu parçalar bağımsız bir şekilde farklı besleme uçlarından uyarıldığı için ana huzme yönü beslemeler arasında faz farkı uygulayarak kaydırılmıştır. Anten, kare mikro şeritlerde uygulanan tek ve çift mod analizi kullanılarak tasarlanmıştır. Anten toprak plakasına dik olan yükseliş düzleminde -40^0 ile $+40^0$ arasını tarayabilecek bir başarıma sahiptir.

İki farklı ışına elemanına sahip bir antenin tasarımı için; benzetim, üretim ve ölçüm süreçleri ve süreçlerde elde edilen sonuçlar sunulmuştur. Bahsi geçen iki ışına elemanı anten kovuk modeli kullanarak tasarlanmıştır. Antende kullanılan dairesel ve yüzük şeklindeki yamalar, farklı kovuk model modlarında çalışacak şekilde tasarlanmıştır. Yüzük anten karşılıklı iki besleme ucu ile dairesel yama ise parazitik olarak uyarılmıştır. Besleme uçları arasındaki faz farkı hangi ışına elemanlarının daha baskın uyarıldığını belirlemektedir. Anten, besleme uçlarını içeren yükseliş düzleminde -40^0 ile $+40^0$ arasını tarayabilecek bir başarıma sahiptir.

Son olarak, dört bağımsız alt elemandan oluşan dikdörtgen yama anten tasarlanıp, benzetimi yapılmıştır. Bu anten ışına örüntüsünde çeşitliliği parazitik elemanlar sayesinde kazanmıştır. Fakat ışına örüntüsündeki çeşitliliğin tek sebebi parazitik elemanlar değildir. Anten dört bağımsız alt eleman içerdiği için, bu elemanların uyarılma sayıları ve sıraları, ışına örüntüsünün yönünde belirleyici etkilere sahiptir. Bu anten yükseliş düzleminde -40^0 ile $+40^0$ arasını tarayabilecek bir başarıma sahiptir.

Anahtar Kelimeler: Işına Örüntüsünde Çeşitlilik, Birden Fazla TM Mod Kullanan Antenler, Işına Örüntüsünde Yapılandırılabilme, Anten Minyatürleştirme, Kovuk Modelinde Analiz

To my family

ACKNOWLEDGMENTS

First of all, I would like to express my deep gratitude to my supervisor Prof. Dr. Özlem Aydın Çivi. Her assistance and entire support in all the thesis and research stages help me to conclude this thesis. Besides, I would like to thank my co-advisor Assoc. Prof. Dr. Lale Alatan for her help and affords. Not only she guided me on my research also, but she has also shown me how to look at the problems and deduce applicable and reasonable comments. Therefore, I present my appreciation to them.

During undergraduate and graduate education, I have met wonderful academicians in the area of mathematical physics and electrical engineering. I would like to thank Damla Alptekin, and Prof. Dr. Sibel Başkal from Middle East Technical University. I am very lucky that I met you.

I also acknowledge the members of my thesis jury for accepting this work for examination and thank them for their valuable comments and suggestions.

I would like to thank my beloved friends. Without them, I am sure that I will not able to finish this thesis. Especially for his valuable critics and comments, I would like to thank Kamil Karaçuha for his motivated and passionate approach to electromagnetics. I also would like to thank Gülfem Ceren Yavuz. They are always with me, and they know every hard step I have encountered throughout the thesis and they helped me a lot.

Finally, I would like to thank my family from my heart. I am very honored and happy that I am the son of Vildan and Zekeriya Çelik family. This thesis cannot be completed without the motivation and their guidance.

I want to thank the Scientific and Technological Research Council of Turkey (TÜBİTAK) for the financial support they provided through 2211-A National Scholarship Programme for M.S. Students.

TABLE OF CONTENTS

ABSTRACT.....	v
ÖZ.....	vii
ACKNOWLEDGMENTS	x
TABLE OF CONTENTS.....	xi
LIST OF TABLES	xiv
LIST OF FIGURES	xv
LIST OF ABBREVIATIONS.....	xx
LIST OF SYMBOLS	xxi
1 INTRODUCTION	1
1.1 Objectives and Structure of the Thesis.....	2
1.2 Array Factor and Its Evaluation at Different Scan Angles.....	5
1.3 Microstrip Patch Antenna.....	7
1.4 Literature review	11
2 ANALYSIS METHODS of PATCH ANTENNAS	19
2.1 Transmission Line Model.....	20
2.2 Cavity model	22
2.2.1 Cavity Model Analysis in Rectangular Patch Antenna.....	23
2.2.2 Cavity Model Analysis of Circular Microstrip Patch Antennas	27
2.2.3 Cavity Model Analysis of Ring-Shaped Microstrip Patch Antennas	31

3	DESIGN, FABRICATION, and MEASUREMENT RESULTS of RECTANGULAR SHORTED PATCH ANTENNA	35
3.1	Antenna Structure	36
3.2	Operation Principle and Even/Odd Mode Analysis.....	41
3.3	Simulations, Parametric Studies	45
3.4	Fabrication of the Antenna	48
3.5	Measurement Results of Fabricated Antenna	49
3.6	Summary and Discussion.....	56
4	DESIGN, FABRICATION, AND MEASUREMENT RESULTS OF RINGED CIRCULAR PATCH ANTENNA	57
4.1	Antenna Structure	59
4.1.1	Selection of Radiators and Geometry of the Antenna	60
4.1.2	Antenna Feed Structures and Their Optimization	62
4.2	Miniaturization of the Antenna.....	63
4.3	Simulations and Parametric Studies	66
4.4	Radiation and Beam Scanning Phenomenon of the Antenna	69
4.5	Isolation Considerations and Enhancement	77
4.6	Fabrication of a Prototype Antenna	81
4.7	Measurement Results	83
4.8	Summary and Discussion.....	89
5	DESIGN AND SIMULATION OF FOUR ELEMENT COMBINED TRIANGULAR PATCH ANTENNA.....	91
5.1	Antenna Structure and Performance Analysis	92
5.1.1	Triangular Element.....	93
5.1.2	Four Element Antenna.....	96

5.1.2.1	Single Port Excitation	98
5.1.2.2	Excitation of Two Neighboring Ports.....	100
5.1.2.3	Excitation of Opposite Two Ports	103
5.1.2.4	Four Ports Excitation	106
5.1.2.5	Summary of Different Feed Structures.....	106
5.2	Antenna Miniaturization Techniques	110
5.2.1	Miniaturizing the Inner Parasitic Rectangle	110
5.2.2	Slot Employment	115
5.3	Summary and Discussions	117
6	CONCLUSIONS AND FUTURE WORKS	119
	REFERENCES	123

LIST OF TABLES

TABLES

Table 2.1 Roots of derivative of Bessel function of the first kind	29
Table 2.2 The X_{nm} values for several TM modes for ring-shaped patch antenna ..	33
Table 3.1 Physical dimensions of the shorted patch antenna	37
Table 3.2 Direction of main beams at $\phi = 0$ plane when different phase combinations are applied from SMA#1 and SMA#2 ports	45
Table 4.1 Dimensions of the ringed circular patch antenna	60
Table 4.2: Dimensions of the miniaturized antenna and value of the capacitors	65
Table 4.3: List of steered beam directions.....	85
Table 4.4 Comparison of measured gain, simulated gain, and directivity values ...	89
Table 5.1 Physical dimensions of the antenna with the triangle radiator	94
Table 5.2 Main beam directions by employing different ports	98
Table 5.3 Main beam directions by employing neighboring port combinations... ..	100
Table 5.4 Main beam directions of different feed combinations.....	104
Table 5.5 Main beam directions when different phase differences applied between ports 1 and 3	104

LIST OF FIGURES

FIGURES

Figure 1.1 Normalized array factors when the radiated beam is steered to different directions.....	6
Figure 1.2 Cross-section of a microstrip structure and E-field lines. [3].....	8
Figure 1.3 Visualization of rectangular patch antenna (a) and the model of radiating edge (b) [3].....	8
Figure 1.4 Coaxial probe feed at the top view (upper) and side view (lower) [3]..	10
Figure 1.5 Aperture-coupled feed (a) and proximity-coupled feed (b) structures [3].	11
Figure 1.6 Geometry of the antennas with parasitic elements. (a)[4] switches are at the top, (b)[5] switches are at the bottom.....	13
Figure 1.7 Geometry of studies, a: [25] and b: [27].....	16
Figure 2.1 Transmission line model for a rectangular patch antenna.	21
Figure 2.2 E-field distribution within the cavity in TM_{01} mode.	24
Figure 2.3 Equivalent magnetic current densities (M_s) on the cavity.....	25
Figure 2.4 E-fields (a) and equivalent radiating currents (b) of rectangular patch antenna in TM_{02} mode of operation.	26
Figure 2.5 Radiation patterns of TM_{01} (a) and TM_{02} (b) modes.....	27
Figure 2.6 Geometry of circular patch antenna [29].....	27
Figure 2.7 Cavity model and equivalent magnetic surface currents for circular patch antenna [29].....	28
Figure 2.8 Electric, magnetic field patterns within the cavity and current distribution at the top plate of the circular patch [28],[29].	30
Figure 2.9 Top and side view of the ring patch antenna [28].	32
Figure 2.10 Magnetic field patterns within the cavity and current distribution at the top plate of the ring-shaped patch antenna.[28].....	34
Figure 3.1 Top view of the shorted patch antenna.	36
Figure 3.2 Side view of the shorted patch antenna.	37

Figure 3.3 Illustration of E_z field for rectangular microstrip antenna without shorting plane [3].....	38
Figure 3.4 Side view of the antenna and E-fields inside substrate for (a) even mode, (b) in the odd mode.....	39
Figure 3.5 Radiation patterns of (a) even and (b) odd mode of operation in rectangular patch antenna at $\phi=0^0$ plane.	40
Figure 3.6: Current distributions (on the left) and radiation patterns at $\phi=0^0$ plane (on the right) of the patch when different phase differences (β) are applied between ports. (a), (b), (c), (d), (e).	43
Figure 3.7 S parameters of a parametric study of x_{size}	46
Figure 3.8 Amplitude of the S parameters results of a parametric study of feed point ($d=2.6-4mm$).	47
Figure 3.9 Amplitude of the S parameters results of a parametric study of feed point ($d=4-6mm$).	47
Figure 3.10 Top view of the fabricated antenna.....	49
Figure 3.11 Measurement and simulation results of the S_{11} parameter of the antenna.....	50
Figure 3.12 Measurement and simulation results of the S_{21} parameter of the antenna.....	51
Figure 3.13 Measurement setup of the antenna in the anechoic chamber.	52
Figure 3.14 Simulation and measurement results of the antenna when 0^0 phase difference is applied.	53
Figure 3.15 Simulation and measurement results of the antenna when 30^0 phase difference is applied.	53
Figure 3.16 Simulation and measurement results of the antenna when 90^0 phase difference is applied.	54
Figure 3.17 Simulation and measurement results of the antenna when 120^0 phase difference is applied.	54
Figure 3.18 Simulation and measurement results of the antenna when 180^0 phase difference is applied.	55

Figure 4.1 Geometry of a ringed circular patch antenna.	59
Figure 4.2 Parametric study on the location of the SMA#1 port.	63
Figure 4.3 Top view of the ringed circular patch antenna.	64
Figure 4.4 S Parameters with respect to frequency when different capacitors (0-0.7 pF) are connected to the ring patch.	66
Figure 4.5 Scattering parameters (S_{11}) with respect to frequency for different distances between radiators (0.95-0.5 mm).	67
Figure 4.6 Scattering parameters (S_{11}) with respect to frequency for different distances between radiators (0.5-0.15 mm).	68
Figure 4.7 Current distributions on patches when distance radiators is 0.15 mm(a) and 0.5mm(b).	69
Figure 4.8 Radiation patterns of TM_{11} (a) and TM_{21} (b) modes in microstrip patch antennas in dB scale.	70
Figure 4.9 Current distributions (a) and resultant radiation pattern (b) when the phase difference between ports is arranged as 0^0	71
Figure 4.10 Current distributions (a) and resultant radiation pattern (b) when the phase difference between ports is 180^0	72
Figure 4.11 Current distributions (a) and resultant radiation pattern (b) when the phase difference between ports is 90^0	73
Figure 4.12: Current distributions of patches when different phase differences (β) are applied.	74
Figure 4.13 Radiation patterns of the antenna at $\phi = 00$ plane for various β values.	76
Figure 4.14 S_{11} and S_{21} parameters of the antenna.	77
Figure 4.15 Isometric view of the shorted antenna.	78
Figure 4.16 Top view of the antennas studied in the second and third isolation methods.	79
Figure 4.17 Comparison of S_{21} values of different isolation enhancement methods.	80
Figure 4.18 Fabricated prototype of the ringed circular patch antenna.	81

Figure 4.19 Representation of milling_error between circular and ring-shaped radiators.	82
Figure 4.20 Input return loss of the designed antenna and the antenna with 0.5 mm milling error.	82
Figure 4.21: Comparison of simulated and measured S_{11} values.	84
Figure 4.22 Measurement setup of the fabricated antenna.	85
Figure 4.23: Radiation Pattern Results of the Antenna at $\phi = 00^\circ$ Plane When 0° Phase Difference is Applied.	86
Figure 4.24: Radiation Pattern Results of the Antenna at $\phi = 00^\circ$ Plane When 30° Phase Difference is Applied.	86
Figure 4.25: Radiation Pattern Results of the Antenna at $\phi = 00^\circ$ Plane When 90° Phase Difference is Applied.	87
Figure 4.26: Radiation Pattern Results of the Antenna at $\phi = 00^\circ$ Plane When 120° Phase Difference is Applied.	87
Figure 4.27: Radiation Pattern Results of the Antenna at $\phi = 00^\circ$ Plane When 180° Phase Difference is Applied.	88
Figure 5.1 Top view of the antenna with four sub-elements in its corners [27].	92
Figure 5.2 Geometry of the triangular element.	93
Figure 5.3 Surface current distribution (a) and radiation pattern at $\phi = -45^\circ$ plane (b) of the single triangular element.	94
Figure 5.4 Input return loss of the triangular antenna element when the SMA port is located at different locations.	96
Figure 5.5 Top view of the antenna.	97
Figure 5.6 Radiation patterns of the antenna when only Port1(a), Port2(b), Port3(c), or Port4(d) is excited.	99
Figure 5.7 Radiation pattern at $\phi=90^\circ$ plane when ports 3 and 4 are excited.	101
Figure 5.8 Radiation patterns of co-polarized and cross-polarized fields when ports 1 and 2 are excited.	102
Figure 5.9 Heart shape 3D radiation pattern when ports 1&3 are fed in-phase.	103

Figure 5.10 Radiation patterns for different phase differences (β) 0^0 (a), 20^0 (b), 30^0 (c), 45^0 (d), 60^0 (e), 90^0 (f), 120^0 (g), 150^0 (h) and 180^0 (i).....	105
Figure 5.11 Beam steering directions when single and neighboring two ports are excited.	107
Figure 5.12 Surface current distributions when different ports are excited together; only port1 (a); ports 1&2 (b); ports 1,2 &3 (c) and all four ports (d).....	108
Figure 5.13 S_{21} , S_{31} , and S_{41} values of the antenna.	109
Figure 5.14 Top view of the miniaturized antenna with curved shorting plates...	111
Figure 5.15 Surface current distributions when port1 (a) and port 1&3 (b) are excited.	112
Figure 5.16 S_{21} Plots of the non-miniaturized and miniaturized antenna with curved planes.	112
Figure 5.17 Surface current distributions when only port 1 is excited.	113
Figure 5.18 S_{21} plots of the non-miniaturized, miniaturized antenna with curved planes and miniaturized antenna with slot application.	114
Figure 5.19 Top view of the antenna with slot and the surface current distribution when only port 1 is excited.	115
Figure 5.20 S_{11} parameters of original and miniaturized antenna designs.	116

LIST OF ABBREVIATIONS

ABBREVIATIONS

5G	Fifth Generation of Communications Protocols
E-field (\vec{E})	Electric Field
FEM	Finite Element Method
FDTD	Finite Difference Time Domain
H-field (\vec{H})	Magnetic Field
MIMO	Multi Input Multi Output
MoM	Method of Moments
PCB	Printed Circuit Board
PEC	Perfect Electric Conductor
PMC	Perfect Magnetic Conductor
S_{11}	Input Reflection Coefficient from port 1 [dB]
S_{22}	Input Reflection Coefficient from port 2 [dB]
S_{21}	Transmission Coefficient [dB]
SMA	SubMiniature version A
TCM	Theory of Characteristic Modes
TE	Transverse Electric
TEM	Transverse Electric and Magnetic
TM	Transverse Magnetic

LIST OF SYMBOLS

SYMBOLS

β	Phase difference [rad or degree]
θ	Elevation angle [degree]
ϕ	Azimuth angle [degree]
ω	Angular Frequency [rad/s]
λ_0	Wavelength in the free space [m]
λ_g	Wavelength in a dielectric [m]
J_s	Electric Current Density [A/m]
J_n	Bessel function of the first kind in n^{th} order
M_s	Magnetic Current Density [V/m]
Y_n	Bessel function of the second kind in n^{th} order
Y_s	Admittance of radiating edge of the patch [$1/\Omega$]
Y_0	Characteristic admittance of transmission line [$1/\Omega$]
μ_0	Permeability of free space [H/m]

CHAPTER 1

INTRODUCTION

The antenna is a crucial component of wireless communication systems. Wireless communication systems are preferred when there is a necessity to reach distant areas, where establishing the direct link is troublesome. This communication concept requires the usage of air as a conveying medium. The electromagnetic signal that includes the message must be coupled to the air to achieve propagation in the air. As the produced electromagnetic power is precious, the coupling phenomenon must be conducted efficiently. In this part of the system, antennas play the role of an efficient coupler. They are employed to match the impedance of the RF system to the air. In wireless communication systems, low-profile antennas are preferred due to their durability, low-cost, and fabrication ease.

This thesis study mainly focuses on the antennas that can be used in the fifth-generation (5G) applications of the wireless communication area. The 5G communication deviates from its predecessor protocols in several performance measures. The 5G protocol provides an advantage in latency, spectral and network energy efficiency, connection density, and peak data rate aspects.[1] In order to achieve these goals, apart from advanced communication techniques, the frequency band that is covered in the spectrum is changed compared to its predecessor protocols. The frequency band of the 5G is divided into many different bands. However, these bands can be classified into two main classes. The separation point of these main classes is selected as 6 GHz. In the scope of this thesis, the sub-6GHz band is studied. One of the most popular bands in sub-6GHz is called the n78 band [2]. This frequency band spans 3.3 to 3.8 GHz in both uplink and downlink processes. Apart from the sub-6GHz bands, to satisfy the harsh requirements of the

5G protocol, millimeter-wave frequency bands are introduced. The aim of operating in this band is to fulfill the performance constraints that cannot be achieved in sub-6GHz designs. One of the popular millimeter-wave band is designated as n527 and uses 26 GHz as its center frequency. This band spans the 25.5-29.5 GHz region in the spectrum[2].

The antennas designed in the scope of this thesis operate in the n78 band, and they are optimized for a center operating frequency of 3.6 GHz.

1.1 Objectives and Structure of the Thesis

The objective of the study is to develop low-profile antennas for a 5G communication system. These antennas operate in the n78 band in the sub-6GHz region of the spectrum. Apart from this operation frequency constraint, the antennas must satisfy the radiation pattern reconfigurability property. Moreover, the maximum physical dimension of the antennas should not exceed $\lambda_0/2$ (λ_0 is free-space wavelength) value as they will be used in a linear array. In the scope of the thesis, the studies conducted can be listed as follows;

- Antenna type is selected as microstrip patch since this structure provides a low profile, and it is easy to fabricate.
- Literature survey studies are conducted on element pattern reconfigurable antennas. In these studies, the operation principles of different structures that result in antenna pattern diversity are observed. Also, delicate points of these studies and problems are highlighted, and several solutions are developed to overcome them.
- Microstrip antennas are analyzed. In this analysis phase, cavity model analysis is employed for different microstrip patch geometries. Three different geometries, such as rectangle, circular and ring-shaped, are studied within this thesis.

- A rectangular patch antenna is designed to operate in the sub-6GHz band of the 5G protocol. This antenna is designed to operate with the ability to reconfigure its radiation beam without forming an array structure. The designed antenna has a novelty in its geometry. The antenna is divided into two independent regions by a conducting wall. The effects of this novelty is investigated with the help of the mod theory. After modeling, parametric analyses are conducted on the antenna. When the parametric analyses are completed, a prototype model is fabricated, and measurements are taken.
- Pattern reconfiguring problem is tried to be solved by introducing multiple radiators to an antenna element. Two different and independent metallic structures are used as a radiating element. In this design, concentric circular and ring-shaped structures are preferred as radiators. This design supports radiation beam scanning by employing two closely coupled radiators. As there is a close coupling, the circular radiator is excited without employing a direct port connection. Antenna operating in element pattern reconfigurable fashion is designed, fabricated, and measured. Parametric analysis is performed to understand the effect of antenna dimensions on its performance.
- Several antenna miniaturization techniques are studied. This procedure was a necessity as the designed antennas must be applicable in array structures. So, their size must be kept as small as possible.
- Finally, an element pattern reconfigurable rectangular microstrip antenna that employs four triangular sub-elements at its corners is designed. In the previous two designs, the main radiation direction could be steered only in one plane. This structure is investigated to explore whether it is possible to steer the main beam in 2D. The design procedure is completed by conducting several simulations and parametric studies.

In this study, all antenna simulations are done by a full-wave solver ANSYS HFSS while MATLAB is used for the array factor simulations and as a graphical interface. The content distribution among the chapters of the thesis can be listed as;

In Chapter 1, the objectives and structure of the thesis are given. The necessity of the element pattern reconfigurable antennas in a practical linear array is demonstrated. The concepts about microstrip patch antennas are explained, and examples from the related literature are given.

In Chapter 2, the microstrip patch antenna structure is investigated using transmission line and cavity models. This section details the cavity model, its operation conditions, equivalent fields, and the TM modes for different patch geometries.

In Chapter 3, the shorted rectangular patch antenna is introduced. The design and operation principle of the antenna are given. After design parts, parametric analysis on antenna size and feed point locations are illustrated. Finally, the fabrication process and measurement results are presented.

In Chapter 4, the ringed circular patch antenna is explained. This antenna consists of two different radiators that are placed concentrically. As there are two different radiating structures, their sizes should be chosen such that their resonance frequencies are equal to each other. A series of parametric studies are conducted to adjust precisely the same operation frequency for both radiators. Also, the antenna size reduction technique that is applied to the ringed circular patch antenna is discussed. The isolation performance of the antenna is illustrated, and this performance is tried to be improved. Finally, the fabrication and measurement results of the fabricated prototype are shared.

In Chapter 5, a rectangular microstrip antenna structure that uses four triangular sub-elements is illustrated. The operation principle and performance of the antenna are explained. Parametric studies are conducted on sub-elements of triangular regions and feed positions. After completing investigations on the unit element, the rectangular antenna and its beam steering performance are studied. As the dimensions of the rectangular design are large to form a linear array, different antenna minimization techniques are employed on the antenna. The results of performance analysis on these methods are shared.

In Chapter 6, discussions regarding three different patch antenna designs are made. Also, conclusions and future studies are conducted.

1.2 Array Factor and Its Evaluation at Different Scan Angles

In 5G applications, standard antenna solutions are not enough for the Multi-Input Multi-Output (MIMO) structure. In MIMO structure, massive array layouts are studied to shape the beam and direct the radiation to the desired users. Conventional arrays suffer from array factor reduction with respect to scan angle. This problem is accompanied by the element pattern limitations of the standard antennas. The beamforming problem of these massive arrays can be solved by applying various unconventional arraying combinations. However, each arraying structure suffers from some drawbacks. The common drawback of the array structures is the reduction of the radiation power with respect to scan angles. This problem can be explained as the difference between the transmitted power when the beam faces different angles. In order not to distract the reader with fancy arraying structures, inspecting linear array structure with progressive phase shift is preferred to explain the mentioned drawback of conventional linear arrays. In this array structure, each element has a progressive β phase shift with uniform amplitude. The normalized array factor of the mentioned array is given in (1.1) [3]. In this array structure, antenna elements are placed along the z-axis.

$$(AF)_n = \frac{1}{N} \left[\frac{\sin\left(\frac{N}{2}\psi\right)}{\sin\left(\frac{1}{2}\psi\right)} \right] \quad (1.1)$$

where $\psi = kdcos\theta + \beta$

In (1.1), ' k ' stands for wave number and ' d ' is inter-element spacing. In this linear array structure, the application of different β values results in beams that are directed to different directions.

To better understand the subject, several array factors directed to different θ angles of 7 element array will be investigated. In Figure 1.1, the array factors can be seen. The array factor for the broadside array is normalized, and a scaling factor is applied to the other two array factors so that same total power is radiated by each array.

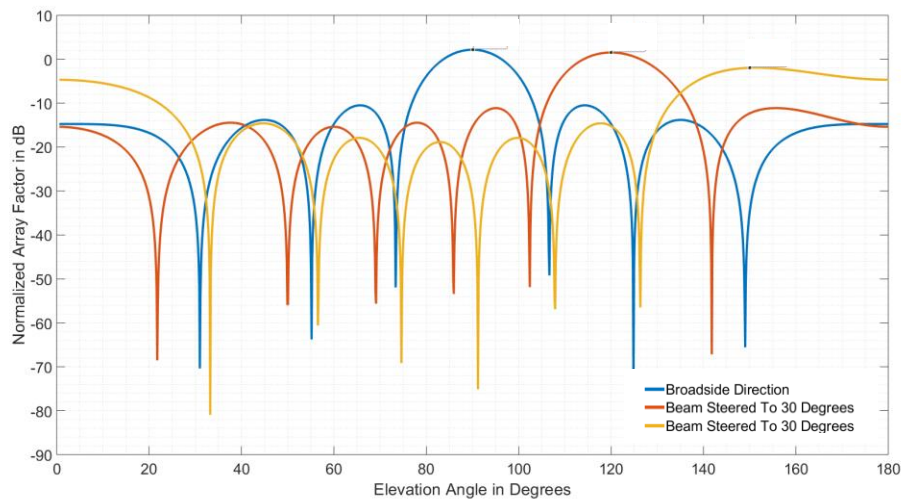


Figure 1.1 Normalized array factors when the radiated beam is steered to different directions.

As shown in Figure 1.1, there is a 0.633dB and 4.113 dB reduction in array factor when the beam is directed to 30 and 60 degrees, respectively. In addition to power reduction due to the array factor, the antenna element factor plays a critical role in reducing power at higher scan angles. A standard patch antenna has an element pattern in broadside direction. This means that it has low directivity at high scan angles, like $\theta = 40^\circ$. When effects of element patterns and array factors are combined, drops in the gain of the array are observed at high scan angles. A lower

gain when the array is directed to high scan angles is a problem that requires a solution.

The element factor of the designed antenna can solve the radiated power problem at high scan angles. The element factor can balance these reductions in the array factor. To achieve a constant radiated power, pattern reconfigurable antennas can be employed. Pattern reconfigurable antenna refers to an antenna element capable of steering its beam.

In this work, pattern reconfigurable antennas that operate at 3.6GHz are studied. The main challenge is to be able to steer the element pattern $\pm 40^\circ$ without affecting the resonance frequency. To satisfy these requirements, three different microstrip patch antenna structures are developed.

1.3 Microstrip Patch Antenna

Microstrip term refers to a layered structure in which conducting strips and/or patches are etched on grounded dielectric substrates. Generally, copper is selected as the conducting material. A potential difference must be applied between conductors on the top and the ground plane at the bottom by excitation port. The excited electromagnetic field is delivered to another port or radiated depending on the properties of the microstrip structure. In this thesis, antenna applications of the microstrip structure will be investigated.

Fabrication of the microstrip structure is conducted by a printed circuit board (PCB) fabrication technique. This technique prints the antenna by milling its shape on at least one of the conducting plates of a double-side grounded dielectric substrate. The antennas on the scope of this thesis are fabricated by milling only at the top plate, and the ground plate is left unmilled. As milling on the top plate creates a bounded surface, fringing fields occur at the edges of the top plate. These fields can be seen in Figure 1.2. Patch antenna only radiates from its edges where fringing fields occur.

Therefore, these fringing fields are essential to understand the radiation behavior of the antenna.

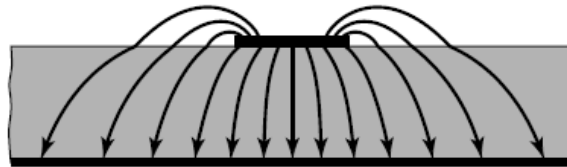


Figure 1.2 Cross-section of a microstrip structure and E-field lines. [3]

The idea of the radiation can be explained briefly by investigating a rectangular patch antenna. In this antenna, a rectangle-shaped patch is milled at the top conducting plate. The visualization of the antenna can be seen in Figure 1.3a.

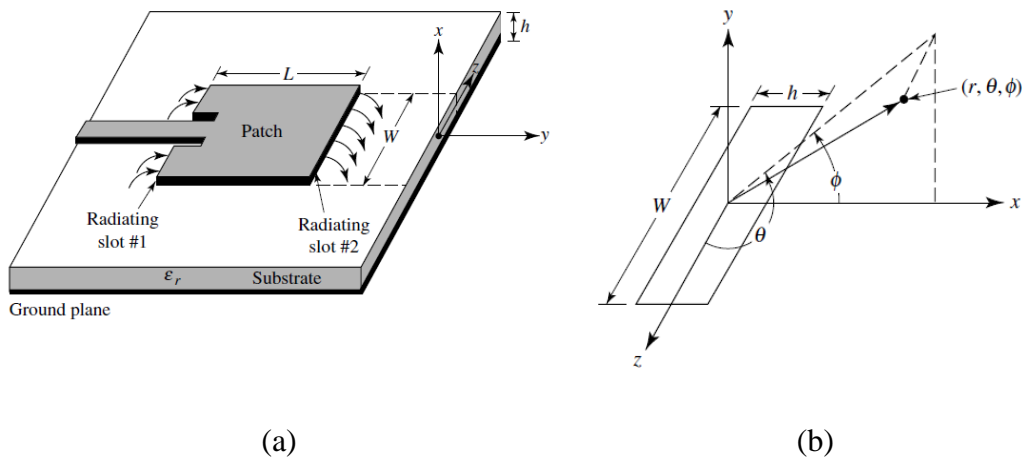


Figure 1.3 Visualization of rectangular patch antenna (a) and the model of radiating edge (b) [3].

The microstrip patch antenna radiates from its edge. These edges are modeled as rectangular slots where radiating fields exist, which are visualized in Figure 1.3b. A pair of radiating slots exist in a rectangular patch antenna. The superposition of these sources determines the overall radiation pattern.

After understanding the radiation mechanism of the antenna, inspecting feeding methods of a microstrip patch would provide a complete understanding of the antenna. There are four popular feeding mechanisms regarding the microstrip patch antenna. The first feeding mechanism is named a microstrip line feed. In this structure feeding line directly makes contact with the radiating edge of the patch. In Figure 1.3a, this feeding mechanism can be seen. This structure has benefits as it is easy to fabricate and simple to match. Matching is done by adjusting the depth of the feed line in the patch and the width of the slots at either side of the line. However, this method also has some significant drawbacks. This feed structure has a substantial bandwidth limitation of up to 2-5 %. This limitation occurs due to an increase in spurious field radiation and surface wave interference caused by the thicker substrates used to widen the bandwidth [3].

Another feeding method of the patch antenna is named coaxial probe feed. In this feeding structure, a coaxial cable is employed. The inner conductor of the coaxial cable is soldered to the top patch, while the outer conductor is connected to the ground plate at the bottom. Visualization of this feed structure can be seen in Figure 1.4.

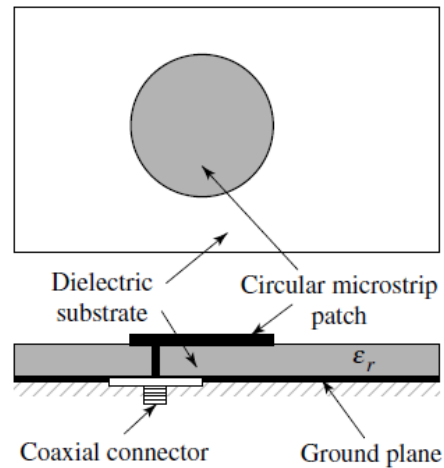


Figure 1.4 Coaxial probe feed at the top view (upper) and side view (lower) [3].

The fabrication of this connection requires drilling through the substrate. The inner conductor is connected to the top patch while avoiding connection with other elements in the antenna from the drilled point. This connection model is preferable, as it is easy to fabricate and easy to match. The matching procedure of this feed structure will be explained in the transmission line model analysis section in chapter 2.

The third and fourth feeding mechanisms do not excite the radiating patch by making a direct connection. Both of them are multilayered structures where feed line and patch are placed on separate substrates. As can be seen in Figure 1.5a, in the aperture coupled configuration, the coupling between the line and the patch is achieved through a slot in the ground plane placed between the substrates of the line and the patch. Fabrication of the aperture coupled structure is challenging as it requires milling at three plates and precision in aligning the layers. Nevertheless, this structure enables the designer to optimize the feeding structure and the patch independently.

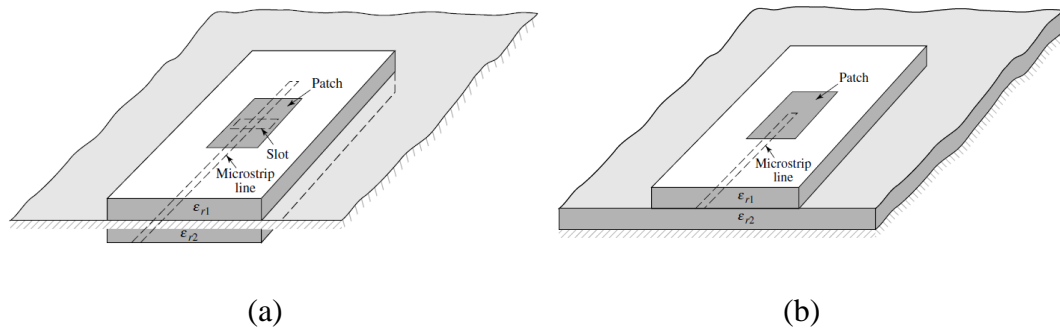


Figure 1.5 Aperture-coupled feed (a) and proximity-coupled feed (b) structures [3].

Lastly, a proximity-coupled feed structure can be used to feed an antenna as an alternative to the aperture-coupling feed. Unlike aperture-coupling, this structure does not employ a slot to couple input electromagnetic energy. Instead, the microstrip line is directly coupled to the radiating patch. The input impedance of the antenna is controlled by the width and length of the microstrip line in both aperture and proximity coupled feed cases. In aperture coupled structure, slot length is also used to control the input impedance of the antenna.

In this thesis, the coaxial probe feed technique is studied on the designed antennas. This technique is chosen as it is easy to implement, arrange a position to match the antenna and apply phase differences between different ports.

1.4 Literature review

The pattern steering phenomena of the antenna are a long-term problem for antenna designers. Therefore, there is extensive literature regarding this subject. As this thesis is focused on single-layered microstrip patch structures, the structures that can shape the beam using only one microstrip layer are investigated, and literature on this type of pattern reconfigurable antennas are shared.

When the literature is investigated, design ideas about pattern reconfigurability by employing a single-layered patch antenna converge to three branches. The first

branch relies on the idea of the parasitic elements to steer the beam. In this method, by placing different parasitic elements, the radiation beam is shaped within an antenna element. The second branch employs different cavity or characteristic modes of the antenna to achieve pattern diversity. The different modes of the patch antenna create different radiation patterns. However, as resonance frequencies of different modes are far away from each other, they cannot be used with simple excitation configurations. This branch studies different modes of operation and tries to obtain different modes at the same frequency band. Multiple radiating elements that operate in different modes can also be used to design pattern reconfigurable antennas. The third branch of the methods employs multiple radiators for pattern reconfiguration. These multiple radiators are referred to as sub-elements, and they perform beamforming in 2D. The challenge of this method is to provide radiation at sub-elements that are electrically smaller than the conventional designs.

Some of the noticeable studies conducted in the first branch employ parasitic elements in the antenna design. The parasitic elements denote the metallic structures placed around the patch antenna but do not have any direct connection with the excited patch. Depending on the size and distance from the radiating patch, the behavior of the parasitic elements changes. If the size of the parasitic element is smaller than the radiator and the distance between them is sufficient, the parasitic element concentrates the main radiation direction of the antenna towards itself. In this case, the parasitic metal is called a director. On the other hand, when an electrically large parasitic conductor is placed close to the radiating antenna, it reflects the radiated fields towards its direction. Therefore, the radiation pattern shifts away from the parasitic structure. When the parasitic element directs the radiating beam away from itself, it is called a reflector. The director-reflector phenomenon of the parasitic elements is used to perform beam steering within a single antenna element. In studies [4] – [7], different antenna-parasitic element topologies are studied, as shown in Figure 1.6, in [4] and [5].

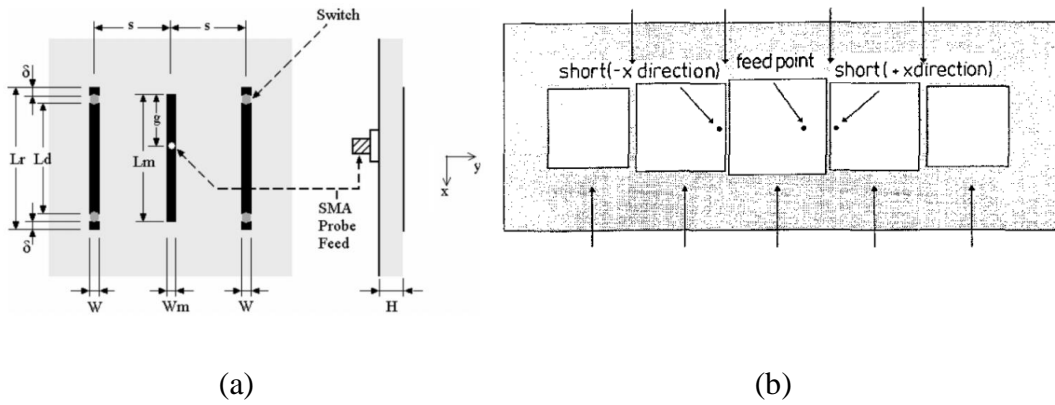


Figure 1.6 Geometry of the antennas with parasitic elements. (a)[4] switches are at the top, (b)[5] switches are at the bottom.

In [4], parasitic strips are located at either side of a printed antenna. The lengths of these parasitic structures can be adjusted by employing switches. When the length of the parasitic element is smaller than the radiating element, it behaves like a director. The opposite phenomenon occurs in the reflector case. By changing the lengths of these parasitic elements, the radiation beam is scanned in the $x=0$ plane. Another study employs the idea of shorted (connected to ground) parasitic elements [5]. The geometry of the antenna can be seen in Figure 1.6b. In this antenna, the parasitic elements are connected to the ground plane through a switching mechanism on the backside of the patch. Depending on the shorted element configuration, the radiation beam of the antenna can be switched. Parasitic elements illustrate satisfactory results when the only performance measure is the radiation direction. However, these structures have significant drawbacks when efficiency and physical size are considered. As they require additional metallic structures, the efficiency of the antenna is reduced. Also, the parasitic elements increase the size of the antenna element and create interference problems at array structures [6].

Apart from the employment of parasitic elements, operating in different microstrip patch modes is an excellent candidate to steer the element pattern of the antenna. In this study, the constraint on beam steering is selected as scanning $\pm 40^\circ$ in the elevation plane. The requirement of radiation at 40° in elevation can be supported by

a monopole-like radiation pattern. Microstrip antennas are also able to create monopole-like radiation, which is also called as conical-shaped beam. One option to create a conical beam in a patch antenna is to construct a top-loaded monopole antenna structure as in [8] and [9]. Another approach to operate a patch antenna with a conical beam is to use shorting pins in the patch antenna. This type of patch antennas are referred as monopolar patch antennas. In [10] and [11], RLC loads are introduced at the edges of a rectangular patch, and shorting pins are employed in the middle section. Thanks to the switchable operation of RLC load, the radiating structure can be switched between monopolar patch mode and conventional patch antenna mode. This phenomenon creates pattern reconfiguration between the conical beam and the broadside radiation.

In rectangular antennas, even and odd modes of operation can also be used to create different radiation beams. [12] investigates the shorting plane usage to divide the antenna into two different radiators. By exciting radiators separately, this antenna can switch between conical and broadside radiation patterns.

Another method to create monopole-like radiation in microstrip antennas is to operate antenna at different Transverse Magnetic (TM) modes of the patch structure. For example, the TM_{02} mode of a rectangular patch and the TM_{21} mode of a circular or ring-shaped patch provide conical beams. In [13], different modes of a rectangular patch are investigated.

The researchers studying multi-mode antennas are more focused on the circular and ring-shaped structures as they offer more symmetrical patterns in the azimuth plane compared to rectangular geometries. The geometry of a circular patch is preferred in studies [14]-[17]. In [14], resonance frequencies of TM_{01} and TM_{02} modes tried to get closer by employing shorting pins. This study optimizes the location and the number of the shorting pins. The study [15] aims to operate TM_{01} and TM_{11} modes of the circular-shaped structure. In order to achieve this goal, it employs switchable RLC loading systems. The study [16] uses a circular patch and an arc-shaped structure to excite different TM modes. This study employs distributed switches to

control which resonator to be excited. Additional resonator idea can be broadened by adding another layer to the microstrip patch structure. The study [17] focuses on the multilayer structures to excite different modes.

Also, the ring-shaped resonators are studied to create different radiation patterns. As the ring-shaped structures have more degrees of freedom than the circular patch, they are more commonly employed in dual TM mode operations. TM_{01} mode of circular or ring-shaped patches also results in a conical beam. However, it is difficult to excite this mode in a circular patch. Whereas it can be conveniently excited in a ring-shaped patch. In [18] and [9], TM_{01} mode excitation of the ring structure is studied.

In [19]-[22], various pattern reconfigurable antenna structures employing circular and ring patches are proposed, which utilize different TM modes of these radiators. [21] uses TM_{11} , TM_{21} , and TM_{31} modes of ring-shaped structures.

Another option to achieve beam steering in an antenna element is the superposition of the multiple sub-elements. Studies under this sub-section use two-dimensional space (2D) to steer radiation beam, unlike studies mentioned previously. The studies [19] and [23]-[27] focus on independent radiating structures with independent feeding solutions. In these studies, the overall radiation pattern is created by the superposition of different and independent patches. The antenna structures studied in [23] and [27] can be seen in Figure 1.7.

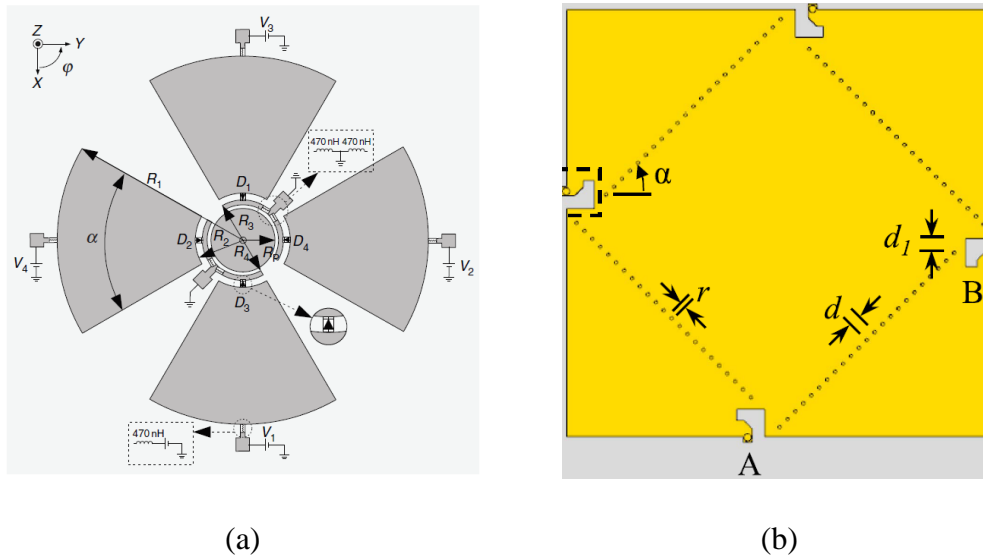


Figure 1.7 Geometry of studies, a: [25] and b: [27].

As shown in Figure 1.7, the study [23] employs four different ring portions as a top plate. These portions can be fed independently; therefore, they possess beam steering property in the azimuth plane. The studies [24] and [27] share the same idea. Multi radiator phenomena are used in [27] by four triangle-like structures to perform beam steering.

In this thesis, three different pattern reconfigurable antenna structures are studied and presented in Chapter 3 to Chapter 5. The design illustrated in Chapter 3 employs a single rectangular microstrip patch antenna. It was inspired by the study in [12]. This antenna employs the idea of different operational modes to create pattern diversity. The structure is separated into two independent portions to achieve different modes, and independent coaxial probes feed each portion. The operational modes mentioned here are not cavity model modes. Independent feed structure enables the employment of even and odd modes. Pattern switching between two modes proposed in [12] is extended to achieve continuous beam steering by applying a phase difference between excitation ports. The amount of applied phase difference arranges the weights of the even and odd modes and enables beam-steering towards multiple angles.

The second antenna that is covered in the thesis uses multiple radiators. In [21], concentric patches are studied. In this work, the aim was to achieve pattern reconfiguration by exciting higher order TM modes as well as fundamental TM mode. The structure of the antenna consists of two rings and one circular patch antenna whose center lies at the same point. Therefore, the antenna contains three different radiating structures. SubMiniature version A (SMA) type connectors independently feed each patch. The circular patch radiates dominant TM_{11} mode while the inner and outer ring operates at TM_{21} and TM_{31} modes, respectively. This antenna structure can independently operate in three modes thanks to multiple feeds at each structure. Although the performance of this antenna is satisfactory, it suffers from a significant drawback. In order to form a conventional linear array, the maximum size of the antenna must be smaller than $0.5\lambda_0$ to avoid grating lobes. But the largest size of this antenna is $0.9\lambda_0$ so, the size of the antenna prevents the formation of regular linear and rectangular arrays. As this study prioritizes antenna elements to be used in an array configuration, the physical size of the antenna gains a vital role. Therefore, this study employs miniaturization techniques.

Finally, the third antenna designed within this thesis accomplishes pattern diversity by using four sub-elements as radiators. The inspiration of this operation is taken from [27]. However, complex matching structure, the large electrical size of the antenna, and employment of several vias are evaluated to be the problematic issues in [27]. In Chapter 5, these problems are discussed, and solution methods by introducing different feeding structures and by employing various miniaturization techniques are presented.

CHAPTER 2

ANALYSIS METHODS of PATCH ANTENNAS

In order to explain the operation of the microstrip patch antenna, several models are developed. Each model has a different advantage to understand the properties of the patch structure. The popular methods that explain the microstrip antenna characteristics can be listed as; transmission line model, cavity model, the theory of characteristic modes, and full-wave methods.

Among those methods, the full-wave method provides the most accurate result about microstrip antennas. In the full-wave approach, the boundary value problem, defined by Maxwell's equations and boundary conditions, is solved numerically. Some of the well-known numerical methods that are employed in computational electromagnetics can be listed as; Method of Moments (MoM), Finite Element Method (FEM), and Finite Difference Time Domain (FDTD). Thanks to advancements in computational power, full-wave methods are widely used to analyze electromagnetic structures. However, these methods do not help a designer to understand electromagnetic phenomena corresponding to a geometry. In order to understand the physical phenomenon, other methods should be studied in the antenna design procedure.

The theory of characteristic modes (TCM) provides an orthogonal set of surface current modes that can be excited on an arbitrarily shaped conductor. These currents are called as characteristic currents, and their distributions depend on the geometry and dimension of the conductor. The position or type of the feed determines only the excitation coefficient of these modes.

In this thesis study, the antennas are designed by employing the transmission line and cavity models. Therefore, in the following sections, these models will be investigated in detail.

2.1 Transmission Line Model

The transmission line model focuses on the radiating open-circuited edges of the patch structure, as shown in Figure 2.1. These edges are modeled as radiators, and they pose an impedance value. The admittance value of the edge (Y_s) can be expressed as in terms of its conductance (G_s) and susceptance (B_s) parts in (2.1) [29].

$$Y_s = G_s + jB_s \quad (2.1)$$

The notation j is used to illustrate an imaginary unit ($j = \sqrt{-1}$). In (2.1), the conductance value is associated with the power radiated from the radiating edge. In contrast, the susceptance value stands for the energy stored in the fringing field near the edge.

The two radiating edges, which are separated by a distance L , are connected to each other with a transmission line of width W . The circuit model used in the transmission line model can be seen in Figure 2.1.

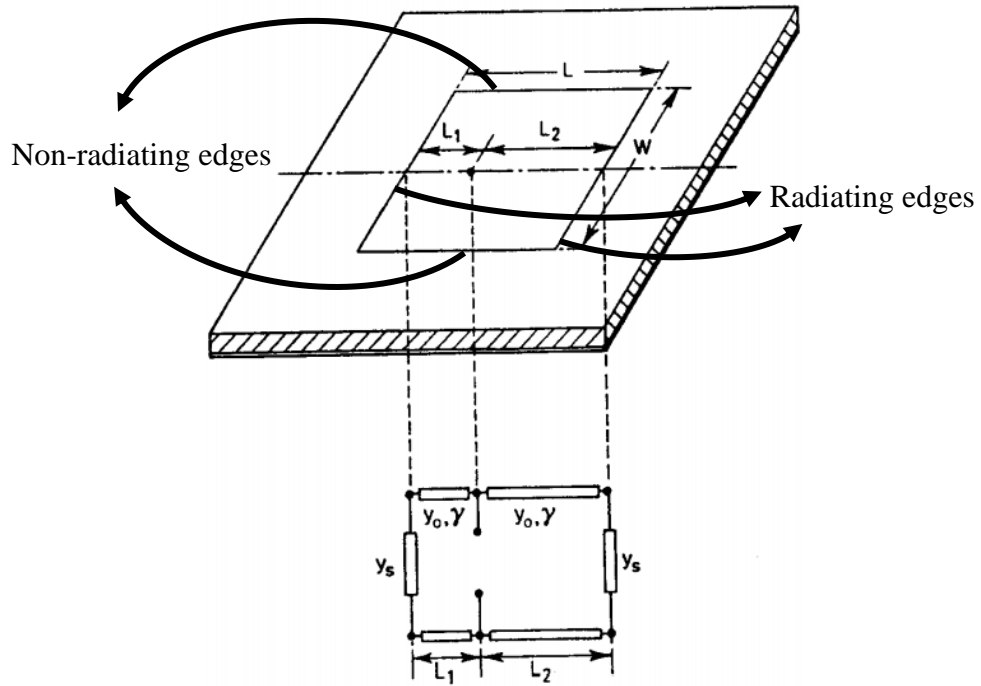


Figure 2.1 Transmission line model for a rectangular patch antenna.

By employing the model illustrated in Figure 2.1 and Telegrapher's equations for the transmission line, the input admittance seen by the coaxial probe feed can be expressed as (2.2) [29].

$$Y_{in} = Y_0 \left[\frac{Y_0 + jY_s \tan(\beta L_1)}{Y_s + jY_0 \tan(\beta L_1)} + \frac{Y_0 + jY_s \tan(\beta L_2)}{Y_s + jY_0 \tan(\beta L_2)} \right] + jX_f \quad (2.2)$$

Where X_f , β and Y_0 are susceptance of the feed, wave number in dielectric and characteristic admittance of the transmission line, respectively. From (2.2), it is understood that the admittance values of radiating edges (Y_s) play an essential role in input impedance. This knowledge enables antenna miniaturization by changing the Y_s value.

The transmission line model can also be used to explain the radiation mechanism and obtain radiated fields. However, in this thesis, pattern reconfiguration is done by switching between different modes of the cavity model. Therefore, using the cavity model to explain the shape and structure of the radiated fields would be more convenient.

2.2 Cavity model

The cavity model is another model used to explain the radiation mechanism and calculate the parameters of a microstrip antenna. As its name implies, this model treats microstrip antennas as a cavity and finds the surface currents on the surface of the cavity that result in radiated fields. In order to apply the cavity model, an antenna must satisfy three crucial assumptions. The first assumption is that the electric field (E-field) inside the substrate does not vary in the z-direction. As the height of the antenna is very small compared to its length and width for most of the microstrip antennas, E-fields do not vary in the z-direction. The second assumption is that the E-field is z-directed. This statement means the E-fields start at the bottom plate and end at the top plate. The third assumption is about H-fields. The tangential component of the H-fields is negligible at the edges. This result is obtained as the electric current in the microstrip has no components normal to the edge at any point on edge. The negligible tangential H-field assumption enables us to replace the periphery of the antenna with magnetic walls.

Mentioned properties convert the patch antenna to a cavity whose side walls are Perfect Magnetic Conductor (PMC), and upper & bottom walls are Perfect Electric Conductor (PEC) [3].

2.2.1 Cavity Model Analysis in Rectangular Patch Antenna

After using the properties mentioned in the previous section, the microstrip patch antenna is modeled as a rectangular closed cavity with PEC walls at the top and bottom and PMC walls at sides. Using the method of separation of variables, the vector potential within the cavity can be expressed in terms of sinusoids in x,y, and z directions. As the thickness of the cavity is very small compared to its width, z variation can be ignored. After deriving E and H fields from vector potential and applying boundary conditions, fields are found as in (2.3) [3]. In this equation, W represents the width of the patch, and L represents the length of it.

$$\begin{aligned}
 E_z &= E_0 \cos\left(\frac{\pi n x'}{L}\right) \cos\left(\frac{\pi m y'}{W}\right) \\
 H_y &= H_0 \sin\left(\frac{\pi n x'}{L}\right) \sin\left(\frac{\pi m y'}{W}\right) \\
 E_x &= E_y = H_x = H_z = 0 \\
 \text{where } x' &= x + \frac{L}{2}, y' = y + \frac{W}{2}
 \end{aligned} \tag{2.3}$$

In (2.3), n and m are integers (0,1,2,3...), but they cannot be equal to 0 simultaneously. (2.3) has multiple solutions depending on the integer values of n and m. These different solution sets are named as Transverse Magnetic (TM) modes of the microstrip antenna and denoted as TM_{mn} .

While investigating TM modes, firstly, the fundamental mode TM_{01} will be studied to understand the radiation mechanism of the antenna. For this mode, m=0 and n=1. After inserting these values, the E-field become as in (2.4)

$$E_z = E_0 \cos\left(\frac{\pi x'}{L}\right) \quad \text{where } E_0 \text{ is a constant} \tag{2.4}$$

When (2.4) is plotted inside the cavity, the E-fields within the microstrip patch antenna are observed as in Figure 2.2. As can be seen from this figure, in the x-direction, E-field has a maximum amplitude at the edges while it is zero at the middle of the rectangular patch antenna. On the other hand, E-field is constant along the y-direction.

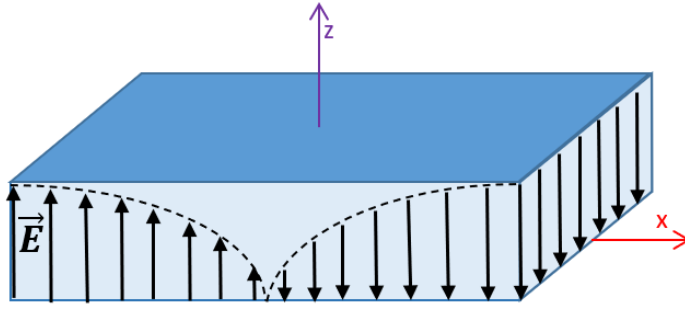


Figure 2.2 E-field distribution within the cavity in TM_{01} mode.

To understand the radiation characteristic of the antenna in TM_{01} mode, surface currents must be found. As mentioned previously, the top and bottom walls of the cavity are modeled as PEC. Therefore, only electric-type surface currents (J_s) can exist on these walls. On the other hand, as the side walls are PMC, magnetic type surface currents (M_s) have significance on these walls. The radiated fields will be calculated by employing these equivalent currents. The equivalent currents can be found by (2.5).

$$\begin{aligned}\bar{J}_s &= \hat{n} \times \bar{H} \\ \bar{M}_s &= -\hat{n} \times \bar{E}\end{aligned}\quad (2.5)$$

In (2.5), \times is the cross-product, and n is the outward unit normal vector to the surface. In (2.5), the E and H fields at the surfaces are used. This means E and H

fields at the boundaries must be evaluated. Equivalent magnetic surface currents of the cavity can be seen in Figure 2.3.

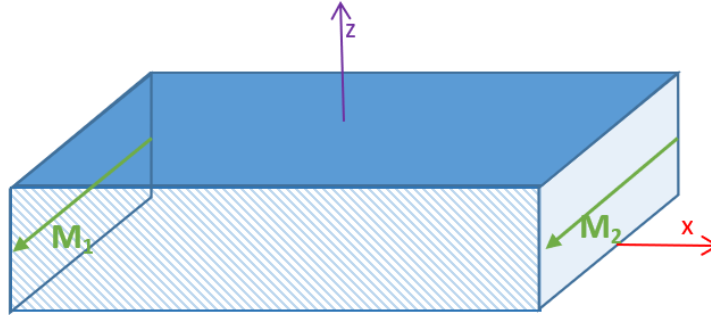


Figure 2.3 Equivalent magnetic current densities (M_s) on the cavity.

M_1 and M_2 currents have the same amplitude due to the symmetry of the E-fields inside the cavity. As can be seen from Figure 2.3, M_1 and M_2 current densities flow in the same direction. Therefore, the radiated fields create constructive interference at broadside direction. This results in maximum radiation in the broadside direction. That is why these edges are called as radiating edges in the transmission line model.

As the main subject of this thesis is to create an antenna that is capable of radiating in different directions, using only TM_{01} mode is insufficient. In order to have radiation at $\pm 40^\circ$, second TM mode of the rectangular antenna must be excited.

In TM_{02} mode, a different set of solutions are obtained for E and H fields within the cavity. To get these solutions $n=2, m=0$ is substituted in expressions in (2.4). Then the fields within the cavity become (2.6).

$$E_z = E_0 \cos\left(\frac{2\pi x'}{L}\right) \quad \text{and} \quad H_y = H_0 \sin\left(\frac{2\pi x'}{L}\right) \quad (2.6)$$

$$\text{while } E_x = E_y = H_x = H_z = 0$$

As shown in (2.6), the period of the E and H fields is changed. These changes illustrate themselves, as seen in Figure 2.4a.

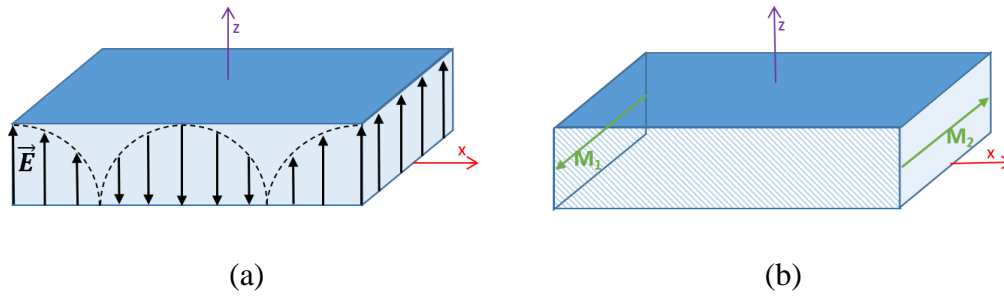


Figure 2.4 E-fields (a) and equivalent radiating currents (b) of rectangular patch antenna in TM_{02} mode of operation.

The change in the E-field period inside the cavity also changed the directions of E-fields at the radiating edges. At these edges ($x=-L/2$ and $x=L/2$), E-fields have the same direction. Therefore, the surface currents derived from these E-fields at the radiating edges are in reverse directions, as seen in Figure 2.4b. When radiated fields are calculated by employing M_1 and M_2 currents in Figure 2.4b, a null is observed in the broadside direction. The null at the $\theta = 0^\circ$ direction yields a conical shaped beam for TM_{02} mode of operation.

Since the objective of the study is to create an antenna that can scan the beam between 0 to 40 degrees in elevation, using TM_{01} and TM_{02} modes of a rectangular patch enables us to have beams at these two limit angles. The 3D radiation patterns of TM_{01} and TM_{02} modes can be seen in Figure 2.5.

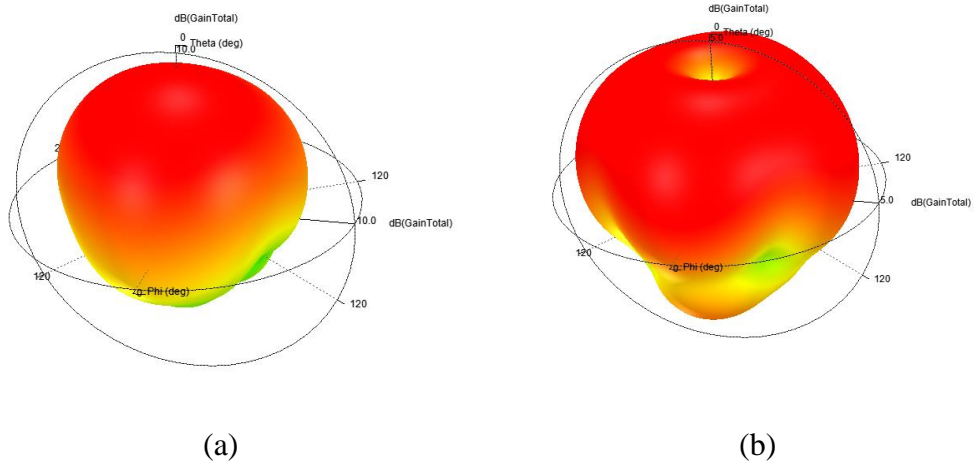


Figure 2.5 Radiation patterns of TM_{01} (a) and TM_{02} (b) modes.

2.2.2 Cavity Model Analysis of Circular Microstrip Patch Antennas

In this subsection, circular disk-shaped microstrip antennas will be investigated by employing cavity model analysis. The performance of the antenna illustrates a remarkable resemblance with the rectangular patch. The only difference between the rectangular patch is the shape of the top plate. The visualization of the circular patch antenna can be seen in Figure 2.6.

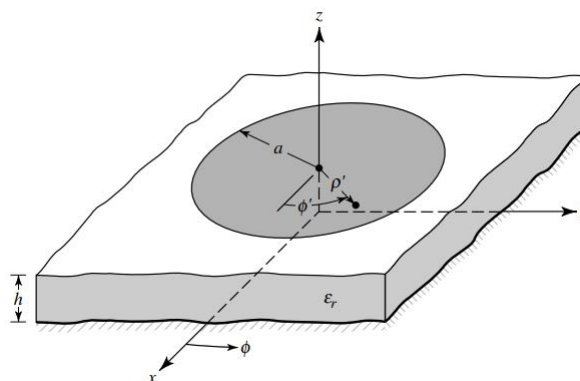


Figure 2.6 Geometry of circular patch antenna [29].

In this analysis, ϕ denotes the angle from the x-axis in XY-plane (azimuth angle), and ρ denotes the radial distance of a point on the patch structure.

The cavity model is also applicable for the circular patch antenna as the height of the substrate is very small compared to its radius. The top and bottom plates are modeled as PEC as they are made of the metallic structure. The peripheral wall of the antenna can be modeled as a PMC wall as the tangential components of the H-field at this wall are negligible. These boundary conditions reduce the antenna to the cylindrical cavity. The illustration of this cavity and its boundaries can be seen in Figure 2.7.

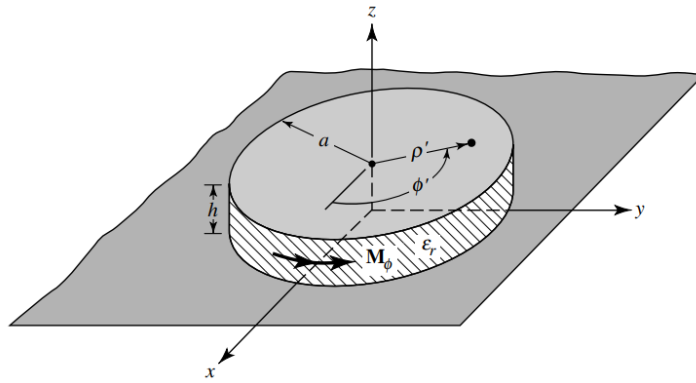


Figure 2.7 Cavity model and equivalent magnetic surface currents for circular patch antenna [29].

The model contains a single magnetic current M_ϕ as a radiating source. The radiation pattern of the antenna is determined by the direction and structure of the M_ϕ source. The E-field within the substrate creates this M_ϕ source at $\rho = a$ boundary of the cavity by following the relation presented in (2.5). E and H fields are obtained as in (2.7).

$$\begin{aligned}
E_z &= E_0 J_n(k\rho) \cos(n\phi) \\
H_\rho &= -j \frac{E_0}{\omega\mu_0} \frac{1}{\rho} J_n(k\rho) \sin(n\phi) \\
H_\phi &= -j \frac{E_0 k}{\omega\mu_0} J'_n(k\rho) \cos(n\phi) \\
E_\rho &= E_\theta = H_z = 0
\end{aligned}
\tag{2.7}[29]$$

In (2.7), the term J_n defines the Bessel function of the first kind in n^{th} order. Besides, the notation J'_n defines the partial differentiation of the Bessel function with respect to ρ variable. The PMC type boundary condition constraints the values that wavenumber (k) may take. This constraint can be expressed as;

$$H_\phi|_{\rho=a} = j \frac{E_0 k}{\omega\mu_0} J'_n(ka) \cos(n\phi) = 0 \quad \text{for all } \phi$$

To satisfy this boundary condition, $J'_n(ka) = 0$ must be satisfied. m^{th} root of the derivative of the n^{th} order Bessel function corresponds to the TM_{nm} mode of the cavity. Some TM modes and corresponding roots are tabulated in Table 2.1.

Table 2.1 Roots of derivative of Bessel function of the first kind

Mode (n,m)	ka
1,1	1.841
2,1	3.054
0,2	3.831

The resonance frequency of a mode can be calculated from the corresponding ka value. As can be understood from the table, TM_{11} has the lowest resonance frequency. TM_{21} and TM_{02} modes follow it.

The n and m values determine the period of the E and H fields inside the cavity. At the rectangular patch antennas mentioned in section 2.2.1, n is related to the E-field distribution period on the x -axis, and m is related to the H-field distribution period on the y -axis. Likely, for circular patch antennas, n is related with the E-field period in ϕ direction while m is related with the fields period in ρ direction. Directions of E-field within the cavity can be seen in Figure 2.8 [29].

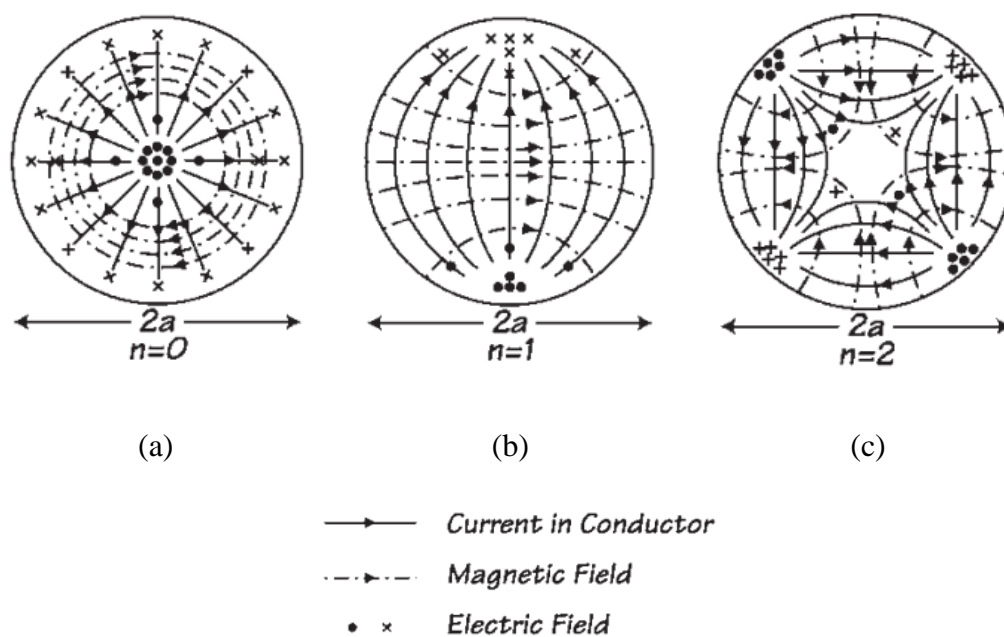


Figure 2.8 Electric, magnetic field patterns within the cavity and current distribution at the top plate of the circular patch [28],[29].

The radiation pattern of the lowest order mode, TM_{11} , is analogous to the lowest order mode of the rectangular microstrip antenna. Figure 2.8b shows the electric field concentrated at each end of the antenna for the $n = 1$ mode. The mode number n corresponds to the number of sign reversals in π radians of ϕ . The next resonant mode is the TM_{21} mode. Figure 2.8c shows the electric field distribution for the $n = 2$ mode. Note that as there are two sign reversals for each π , the E-field has four extremum points on the antenna. This mode is the first of a family of modes that are used to create a monopole-like pattern (conical beam). The third mode is the TM_{02} mode. In this situation, the mode index n is zero, which implies that no sign reversals occur because the cosine in (2.7) becomes unity for all values of ϕ . Therefore, it is independent of the angle ϕ . Figure 2.8a shows the $n = 0$ modes and illustrates the uniform electric field around the periphery of the circular antenna. This mode also radiates a monopole-like pattern.

2.2.3 Cavity Model Analysis of Ring-Shaped Microstrip Patch Antennas

In the scope of this thesis work, a ring-shaped patch antenna is also studied. This antenna satisfies all properties of the microstrip structure. The operation principle and notation of TM modes that can be excited within it, has the same properties as the circular patch antenna. However, it has a different geometry of the top plate. The geometry of the antenna can be seen in Figure 2.9.

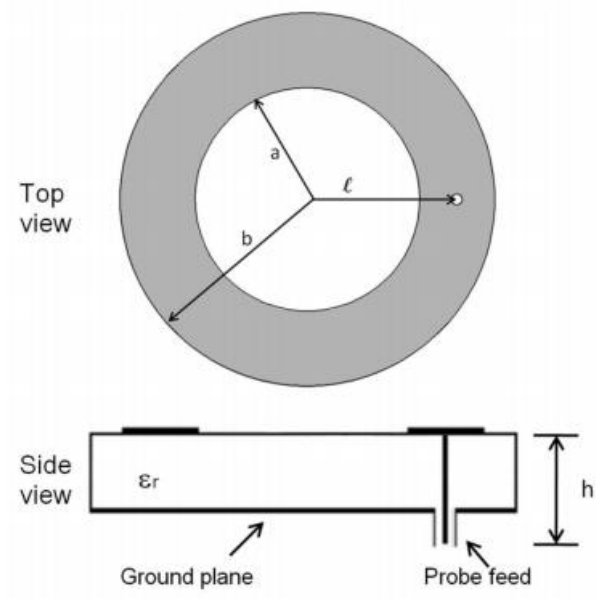


Figure 2.9 Top and side view of the ring patch antenna [28].

Although the ring-shaped antenna shares many properties with the circular patch antenna, like symmetry in ϕ direction and TM mode of operation, it has different boundary conditions. The solution procedure of the ring-shaped patch is the same as the circular patch antenna; so, (2.7) also applies. However, for a ring-shaped patch antenna, there is an additional PMC boundary condition at $\rho = a$. Additional boundary condition affects the E_z expression. The E and H field expressions within the ring-shaped cavity are given in (2.8)

$$\begin{aligned}
 E_z &= E_0[J_n(k\rho)Y'_n(k\rho) - J'_n(k\rho)Y_n(k\rho)]\cos(n\phi) \\
 H_\rho &= j\frac{\omega\epsilon}{k^2}\frac{1}{\rho}\frac{\partial E_z}{\partial\phi} \\
 H_\phi &= -j\frac{\omega\epsilon}{k^2}\frac{\partial E_z}{\partial\rho} \\
 E_\rho &= E_\theta = H_z = 0
 \end{aligned}
 \tag{2.8}[29]$$

Due to additional boundary condition, E_z expression includes the Bessel function of the second kind in n^{th} order (Y_n). In (2.8), prime (') notation denotes partial derivation with respect to ρ variable. When the boundary conditions for H_ϕ are imposed, the following equation needs to be satisfied;

$$J'_n(X_{nm})Y'_n(X_{nm}) - J'_n(X_{nm})Y'_n(X_{nm}) = 0$$

where

$$X_{nm} = k_{nm}a = 2an/(a + b)$$

The equation can be satisfied by several X values. These values determine the TM mode at which the antenna operates. The several roots of this equation can be found in Table 2.2.

Table 2.2 The X_{nm} values for several TM modes for ring-shaped patch antenna

Mode (n,m)	X_{nm}
1,1	0.6773
2,1	1.3406
3,1	1.9789

The explanations for the TM mode operation of a ring-shaped antenna are same as the circular patch antenna. In TM_{nm} notation, n is related to the E-field period in ϕ direction while m is related to the fields period in ρ direction. TM_{11} mode is the dominant mode of the antenna as it has the smallest resonance frequency. This mode radiates in a broadside direction, just like the fundamental mode of the circular patch. TM_{11} mode is followed by TM_{21} mode. This mode concentrates currents to four points of the antenna. Therefore, radiated fields occur in a conical beam fashion. The

radiation pattern of this mode and operation principle is identical to the TM_{21} mode of the circular patch antenna. The current distributions on the top plate of the ring-shaped patch antenna can be seen in Figure 2.10.

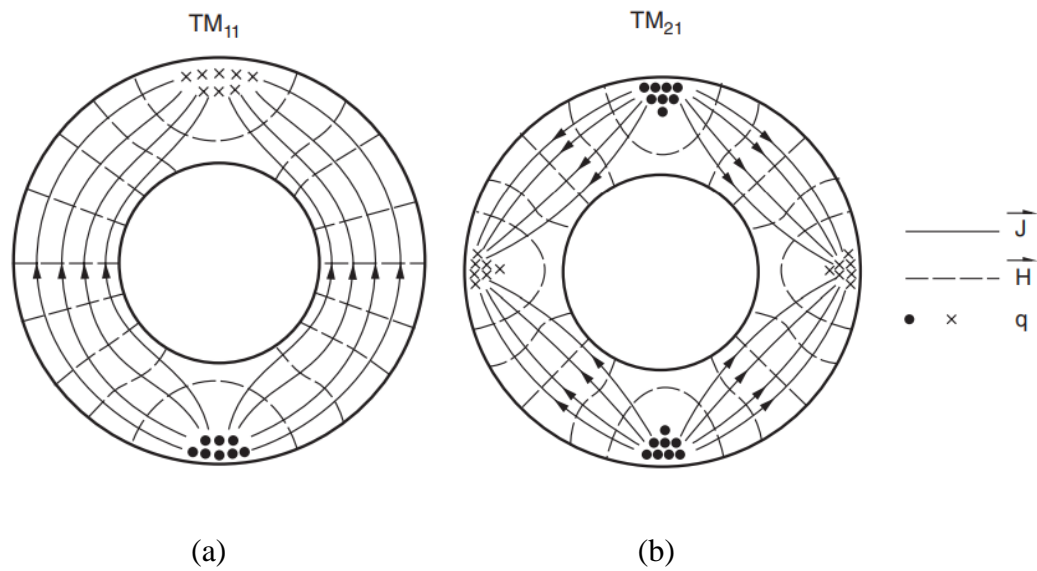


Figure 2.10 Magnetic field patterns within the cavity and current distribution at the top plate of the ring-shaped patch antenna.[28]

CHAPTER 3

DESIGN, FABRICATION, and MEASUREMENT RESULTS of RECTANGULAR SHORTED PATCH ANTENNA

As mentioned in Chapter 1, the beam scanning array structures suffer from gain reduction at low scan angles due to the fixed radiation pattern of the array element. The arrays that will be employed in 5G applications will also suffer from this problem. A pattern reconfigurable antenna element that resonates at 3.6 GHz will be introduced in this chapter to propose a solution to this problem. In the literature, several studies are conducted on rectangular patch structures to achieve rotation on the radiated beam. Several studies tried to match the operating frequency of two different TM modes by applying variable RLC loading to the antenna [10]. Another approach was made use of a single radiating mode by applying two different feed points [12].

While designing rectangular shorted patch antenna, ideas illustrated in [12] are followed. [12] illustrates even and odd modes of operations and explains their behaviors. The antenna that will be explained in this chapter also employs even/odd modes. However, this study introduces a more efficient feeding structure and a radiation pattern performance. Also, the pattern reconfiguring performance of [12] is improved, and beam scanning in multi-direction is achieved with the rectangular shorted patch antenna.

In this chapter, a pattern reconfigurable rectangular microstrip type antenna is investigated. First, the geometry of the antenna and its deviations from the standard square patch antenna is explained. After determining the antenna geometry, characteristics that enable the pattern reconfigurability properties are introduced.

Distinct operational modes (even-odd) and their combinations are studied. After having a theoretical background on the subject, dimensions of the antenna and their importance are highlighted by performing parametric studies. Then beam steering performance is investigated. The fabrication process and prototype antenna were introduced. Lastly, the measurement results are discussed in comparison with simulation outcomes.

3.1 Antenna Structure

In this design, a square patch is employed. This patch is divided into two symmetrical portions with the help of a shorting plane. Two different fed ports (SMA) are employed. The illustration of the antenna can be found in Figure 3.1 and Figure 3.2.

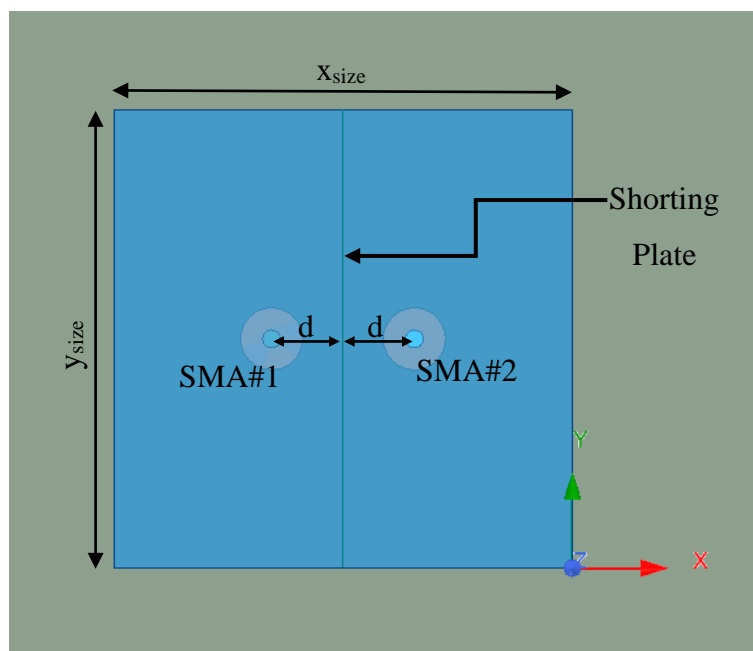


Figure 3.1 Top view of the shorted patch antenna.

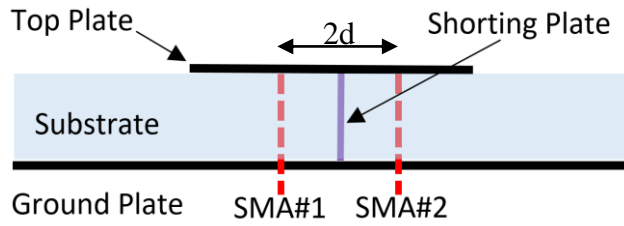


Figure 3.2 Side view of the shorted patch antenna.

In this antenna, a probe-fed single-layer microstrip patch configuration is employed. As a substrate, Rogers 5880 laminates ($\epsilon_r=2.2$) are used. SMA connectors are preferred at the feeding ports.

The shorting plane divides the top plate into symmetrical parts. The division is conducted by a copper plane, and it connects the middle section of the top plate with the ground plate. Due to this connection, the antenna always achieves zero potential at its middle section. The connection of the shorting plane and SMA ports was visualized in Figure 3.2. The physical dimensions of the antenna are given in Table 3.1. The variables used for the dimensions of the antenna are defined in Figure 3.1.

Table 3.1 Physical dimensions of the shorted patch antenna

Variable	Value (in mm)
x_{size}	25.7
y_{size}	25.7
d	4
Substrate size	100 x 100
Substrate thickness	1.575

If the shorting plane and second excitation port of the antenna were removed, the antenna would radiate in its TM_{01} mode. To better understand the subject, one must investigate the cavity model for the microstrip antenna. When the concepts presented in Chapter 2 are revisited, the E-field beneath the radiator can be found as in (3.1).

$$E_z = E_0 \cos\left(\frac{\pi}{x_{size}} x\right) \quad (3.1)$$

When (3.1) is investigated, E_z fields have maximum amplitudes at the top plate edges and have zero amplitude in the middle of the top plate. This phenomenon is illustrated in Figure 3.3.

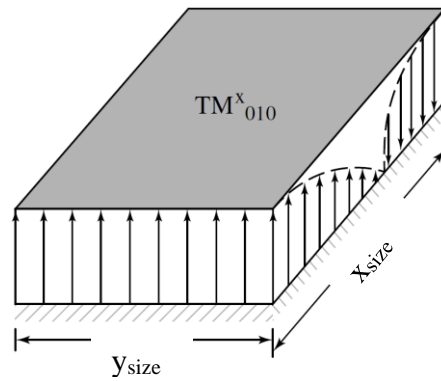


Figure 3.3 Illustration of E_z field for rectangular microstrip antenna without shorting plane [3].

The E-field distribution seen in Figure 3.3 emphasizes the planes where E-field does not exist. These null points reside in $x = x_{size}/2$ plane. Therefore, connecting this plane to voltage zero reference does not affect the distribution of the remaining E-field. In a shorted rectangular patch antenna, this idea is followed. By placing

conducting sheet between the top plate and bottom plate at $x = x_{\text{size}}/2$ plane, the E-field and radiation characteristics of the TM_{01} mode are not disturbed.

The addition of the conducting plane in the middle of the patch yields a different feeding opportunity. As the antenna is separated from its middle, feeding the second part of the antenna independently becomes possible. As the primary purpose of the antenna is to rotate the radiation pattern between $0^\circ - 40^\circ$ in elevation, an operational mode that radiates conically is necessary. This conical radiation pattern is created by feeding the second half of the patch with an identical signal to the first half of the patch. This identical feeding mechanism creates E-fields beneath the top plate in the same direction. Under these circumstances, the operation will be named the odd mode since the equivalent magnetic currents at the radiating edges will be out of phase.

Even mode application is obtained when SMA#1 and SMA#2 are fed with signals that have 180° phase difference. E-field occurs in reverse directions within two halves of the antenna. The E-field distribution of even mode is identical to the TM_{01} mode, so the equivalent magnetic currents at the radiating edges are in phase. The visualization of these modes and their E-fields can be seen in Figure 3.4.

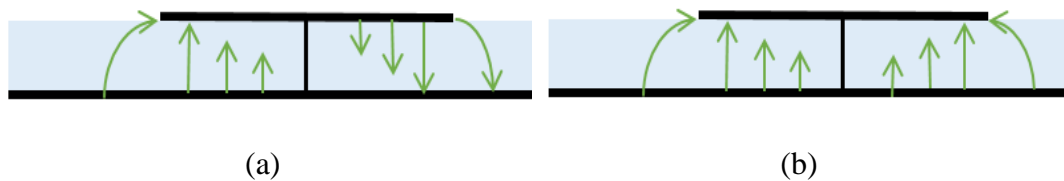


Figure 3.4 Side view of the antenna and E-fields inside substrate for (a) even mode, (b) in the odd mode.

In Figure 3.4, green arrows represent the magnitude and direction of the E-field within the cavity under the patch antenna. As can be understood from the figure, field distributions in even mode occur in the same fashion when the antenna is fed

from only one port, and the shorting plane is not present (Figure 3.3). As this E-field distribution is same as the TM_{01} mode, the resultant radiation pattern would be in the boreside direction. On the other hand, in the odd mode of operation, the E-field beneath the second half of the patch antenna has the same direction as the first half of the antenna. This type of E-field distribution creates a radiation null at the center of the antenna. Therefore, the resultant radiation pattern is in a conical fashion. The radiation patterns of both even and odd modes are illustrated in Figure 3.5.

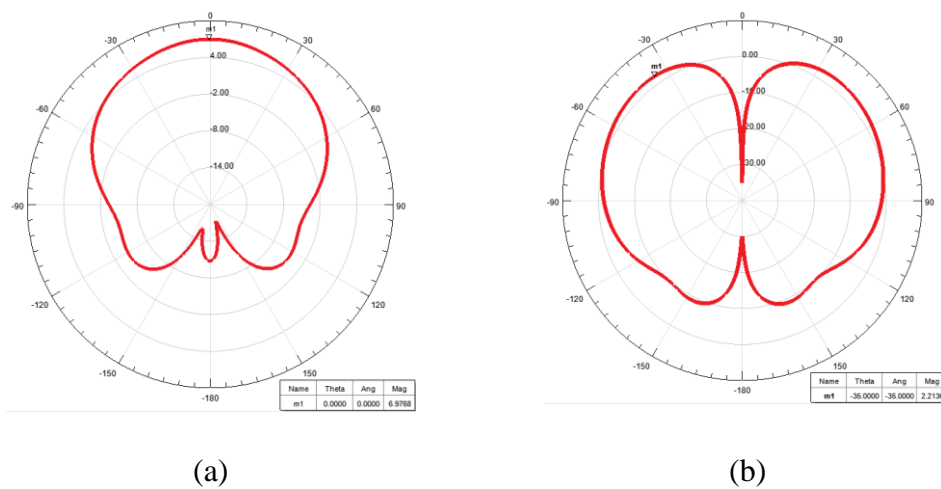


Figure 3.5 Radiation patterns of (a) even and (b) odd mode of operation in rectangular patch antenna at $\phi=0^0$ plane.

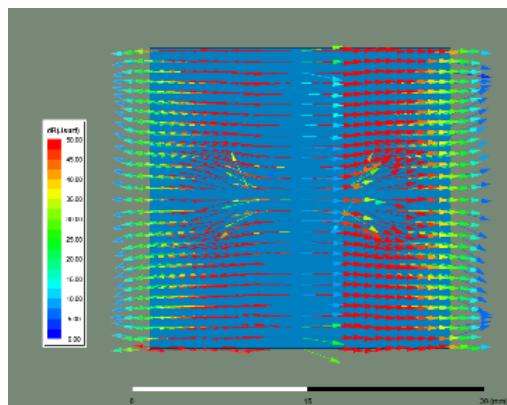
Different radiation patterns can be achieved from a single radiator by exciting different operation modes. The selection of operating mode is determined by the phase difference between two SMA ports. When two ports operate under identical phase, both edges experience E-field maximum instantaneously. This excitation yields an odd mode of operation. However, when there exists an 180^0 phase difference between excitations, E-field distributions also have an 180^0 shift, which means when the first half of the patch edge experiences E-field max, the second half

of the antenna edge experiences E-field minimum. This creates an even mode of operation.

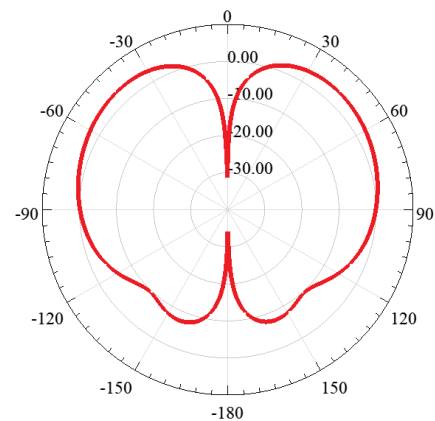
The ability to operate in two different modes results in two very distinct radiation patterns. However, to be able to scan the entire $0^{\circ} - 40^{\circ}$ radiation range, shorted patch antenna must be able to scan other angles within the range. To do this, an intermediate phase difference should be applied between SMA probes. Variation of the main beam direction with the applied phase difference will be studied in the following sections.

3.2 Operation Principle and Even/Odd Mode Analysis

The operation principle of the antenna was explained as a combination of the even and odd modes. This behavior can be understood more clearly by inspecting the current densities on the surface of the antenna. In Figure 9, current densities on the patch surface can be seen when 0° , 30° , 90° , 120° , and 180° phase differences (β) are applied between ports.

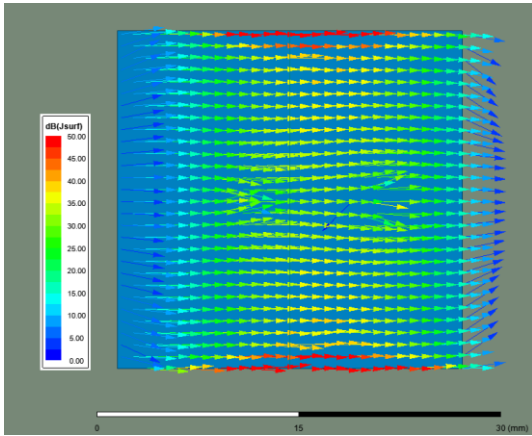


(a1)



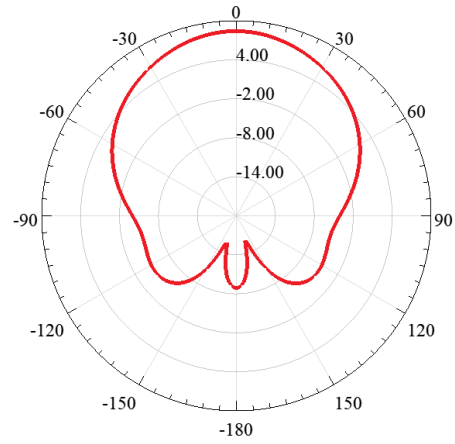
(a2)

$\beta = 0^{\circ}$

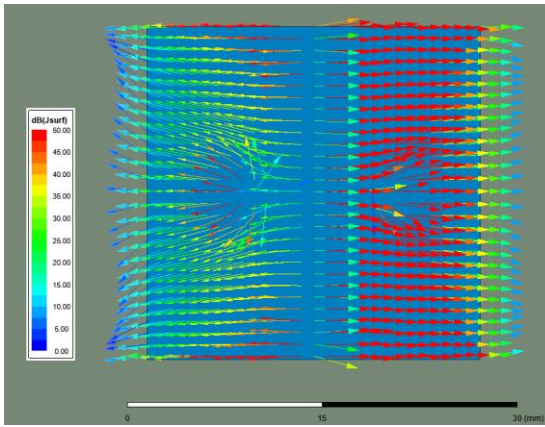


(b1)

$\beta = 180^\circ$

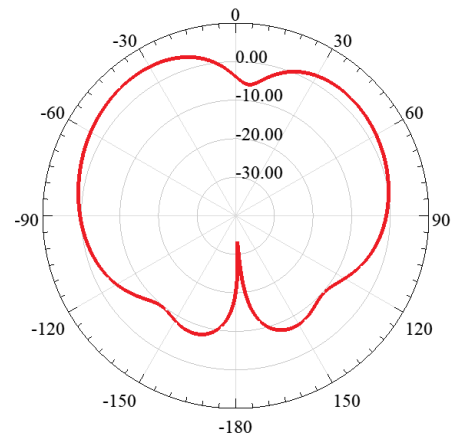


(b2)

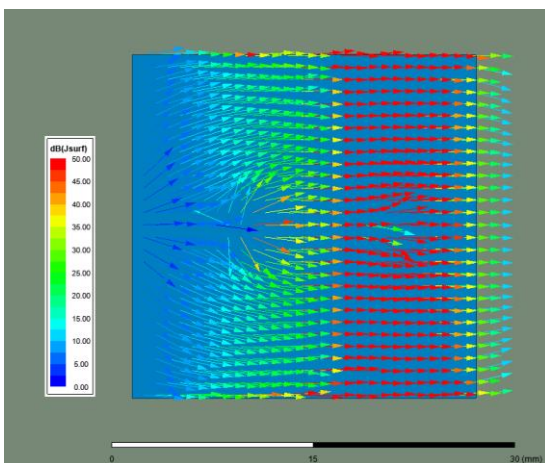


(c1)

$\beta = 30^\circ$

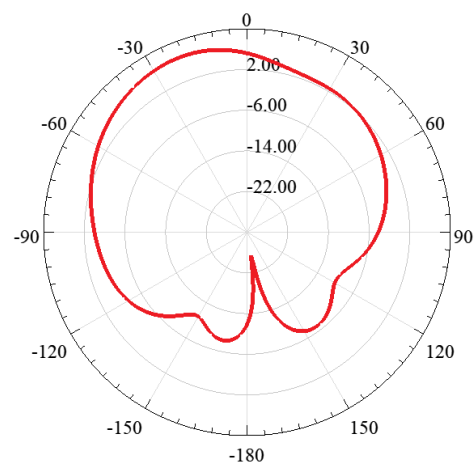


(c2)



(d1)

$\beta = 90^\circ$



(d2)

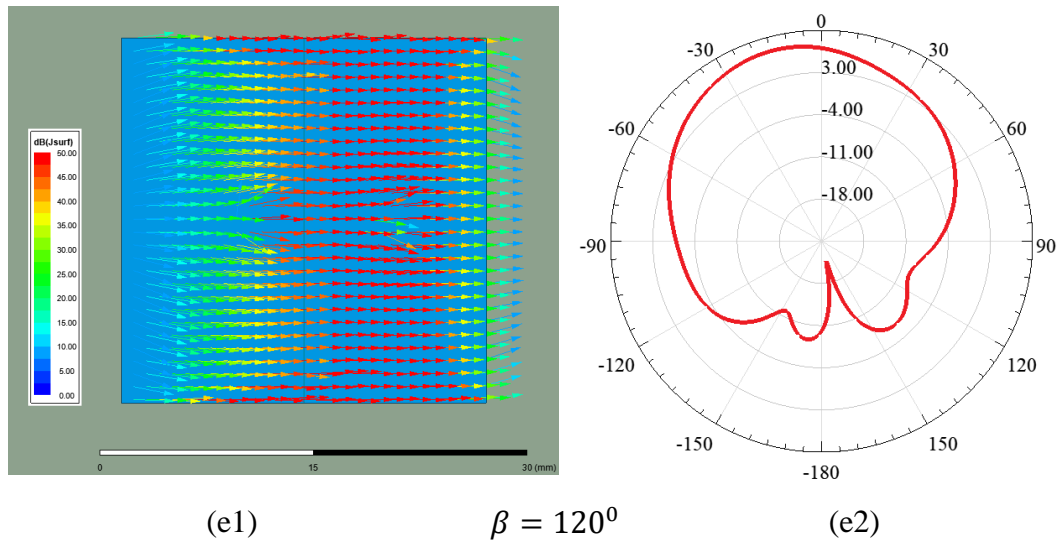


Figure 3.6: Current distributions (on the left) and radiation patterns at $\phi=0^\circ$ plane (on the right) of the patch when different phase differences (β) are applied between ports. (a), (b), (c), (d), (e).

When 180° phase is applied to SMA#1 excitation, the input signal entering SMA#1 port lags the signal sent from SMA#2 by 180° . The sign of the phase difference determines the direction of the radiation pattern. The radiation pattern is directed towards the antenna section that lags. In the examples illustrated in Figure 3.6, SMA#1 port lags. Therefore, the radiation beam is directed to $-\theta$ degrees (negative elevation angles).

When the SMA ports are excited in-phase, as in Figure 9a, oppositely directed currents are observed at the right and left halves of the antenna, which indicates that they are out of phase. The out-of-phase currents result in destructive interference in the broadside direction. Therefore, a null point occurs at the radiation pattern at broadside direction. This behavior is the odd mode operation. So the radiation pattern will be conical. The current distribution and radiation pattern of the investigated case can be seen in Figure 3.6 (a1) and Figure 3.6 (a2), respectively.

Unlike the operation with in-phase excitation, when the patch is fed by applying 180° phase from SMA#1, the antenna behaves like a single rectangular piece radiating at TM_{01} and operates in its even mode. So the resultant radiation pattern is directed to the boreside, as seen in Figure 3.6 (b2).

The operation of the antenna, when different phase differences are applied, can be explained as the superposition of even and odd modes with different weights. For instance, when 30° phase difference is applied from SMA#1, the resultant radiation pattern has a maximum at $\theta = -30^\circ$ direction, as seen in Figure 3.6 (c2). This scan angle is closer to the scan angle of the odd mode operation case ($\theta = \pm 40^\circ$).

Other operation modes that are illustrated in Figure 3.6 also work with the same idea. In 90° phase difference application, the surface currents on the left-hand side are very weak. This small amplitude occurs due to the phase shift. This feeding structure puts the antenna in a situation right between even and odd modes of operation. Therefore, the angle of the main beam is also located between even and odd mode cases. As it can be seen from Figure 3.6(d2), radiation direction is $\theta = -21^\circ$. Another operational mode that steers the beam to smaller angles can be seen in Figure 3.6(e1 and e2). In this case, the applied phase difference is 120° , which is closer to 180° . Therefore, the operation mode is closer to the even mode. This phenomenon pronounces the component that results in radiation towards broadside direction. Due to this component, the main beam scans a smaller angle such as $\theta = -13^\circ$.

The direction of the main beam when different phase combinations are applied to each port are tabulated in Table 3.2.

Table 3.2 Direction of main beams at $\phi = 0$ plane when different phase combinations are applied from SMA#1 and SMA#2 ports

Applied Phase from SMA#1 (in deg)	Applied Phase from SMA#2 (in deg)	Main Beam Direction at $\phi = 0^\circ$ plane
0	0	$\theta = \pm 40^\circ$
30	0	$\theta = -30^\circ$
90	0	$\theta = -21^\circ$
120	0	$\theta = -13^\circ$
0	30	$\theta = 30^\circ$
0	90	$\theta = 21^\circ$
0	120	$\theta = 13^\circ$
180	0	$\theta = 0^\circ$

3.3 Simulations, Parametric Studies

The electromagnetic simulations of the shorted microstrip patch antenna are done in ANSYS HFSS. The shorted microstrip antenna has variables like feed position and patch length that affect performance significantly and must be determined precisely with simulations. In the following text, these parameters and their effects on the resonance frequency will be investigated.

The conventional rectangular patch antennas are designed so that their length between two radiating edges is $0.5\lambda_g$. As the substrate medium is denser than the air, a wave propagating inside the substrate has a different wavelength than the free space one. This different wavelength is named as guided wavelength (λ_g), and it can be found by dividing λ_0 to the square root of effective permittivity [30].

After determination of the patch dimensions by using $0.5\lambda_g$, it is observed by simulations that the resonance occurs at a lower frequency. Therefore, a parametric

study is conducted on x_{size} to find the actual resonant length. When the parametric analysis is studied around this length, the desired resonance occurs when x_{size} is 25.7 mm. The parametric study of x_{size} can be seen in Figure 3.7. In this figure, the lines represent both S_{11} and S_{22} values. As the antenna has a symmetrical geometry, reflection values have the same value for both ports.

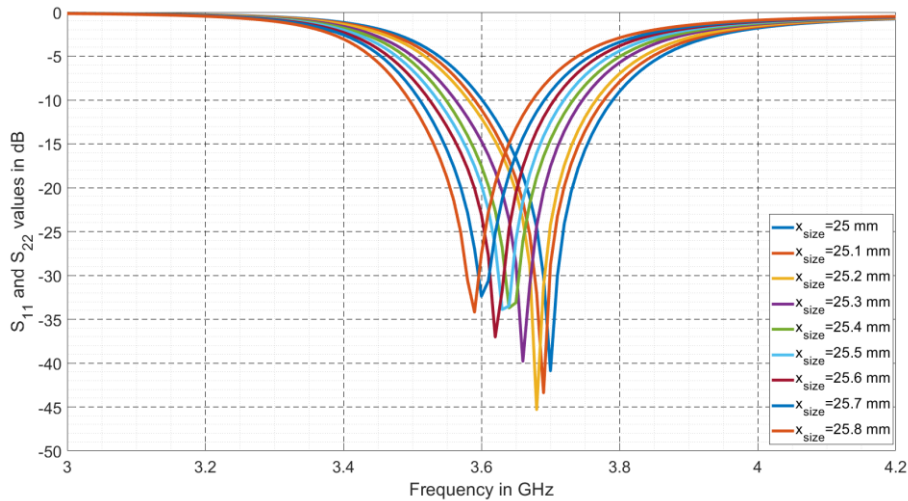


Figure 3.7 S parameters of a parametric study of x_{size} .

As shown in Figure 3.7, the relation between x_{size} and the resonance frequency is inversely proportional. When x_{size} increase the resonant frequency decrease. This result matches with theoretical expectations.

Another discussion about the shorted patch antenna can be conducted by inspecting the feed position (d). As the coaxial feed probe is used, the soldering point gains importance in reflection characteristics. An optimal feed connection position can be found by analyzing the antenna using the transmission line model. As explained in Chapter 2, the transmission line model assumes that the antenna is composed of transmission lines and load impedances located at radiating edges. Antenna transforms these impedances at the edges according to the position of the coaxial probe feed. The coaxial probe must be connected to the point where the impedance

is close to 50 Ohm. The optimum point for coaxial probe connection is determined after employing a parametric analysis. The results of this analysis can be seen in Figure 3.8 and Figure 3.9. As a large number of different d values are considered, results of parametric studies are illustrated in two different figures. Like Figure 3.7, in Figure 3.8 and Figure 3.9, only S_{11} are plotted.

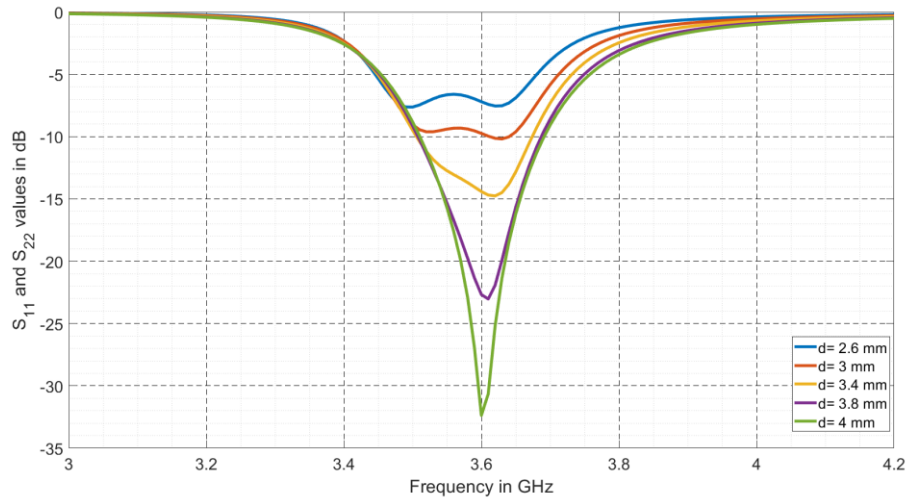


Figure 3.8 Amplitude of the S parameters results of a parametric study of feed point ($d=2.6-4\text{mm}$).

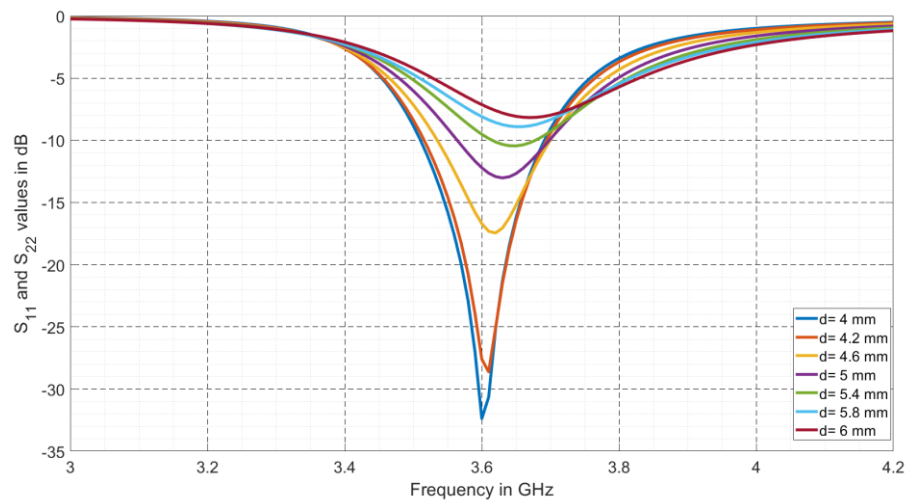


Figure 3.9 Amplitude of the S parameters results of a parametric study of feed point ($d=4-6\text{mm}$).

In Figure 3.8, parametric studies are illustrated where the position of the coaxial probe is scanned in a range that is close to the shorting plane ($d \leq 4\text{mm}$). Likewise, in Figure 3.9, parametric studies are done in a range where the coaxial probe is close to the center of the 1st half of the patch antenna ($d \geq 4\text{mm}$). As can be seen from both figures, the optimized point of the coaxial feed is between the shorting plane and the center of the half patch.

3.4 Fabrication of the Antenna

The designed antenna is fabricated by employing a circuit board plotter machine (LPKF ProtoMat H100). This equipment is used for prototyping PCB projects. ProtoMat H100 creates the desired microstrip patch antenna by employing milling. The device contains several sensitive drills. The system operates on dielectric substrates, whose surfaces are coated with thin copper. To print the designed antenna, drills rub out the empty part of the designed antenna by milling the copper coating. The prototype antenna that is fabricated by employing this technique can be seen in Figure 3.10.

In the fabrication process, substrate material yielded difficulties. As Rogers 5880 is chosen as a substrate, milling must be done onto this material. However, due to the sticky nature of the material, milling it was a challenge. Another difficulty is experienced while inserting the shorting wall located at the middle section of the antenna. As this plate is soldered manually, height adjustment has crucial importance.

A panel-type SMA connectors are used to feed the antenna. The ground plane of the antenna is soldered to the flat surface of the connector carefully. Simultaneously, the inner conductors of the SMA connections are soldered to the upper plates.



Figure 3.10 Top view of the fabricated antenna.

3.5 Measurement Results of Fabricated Antenna

In this part, the measured reflection coefficient, radiation pattern, and gain values of the shorted patch antenna will be shared. Reflection coefficients of the antenna are measured by employing a network analyzer (Keysight E5071C), and they are presented in Figure 3.11.

SMA#1 and SMA#2 ports' behaviors are the same as the antenna has a symmetric topology. Therefore, investigating only one port is sufficient to understand matching performance. The measurement and the simulation results for S_{11} are compared in Figure 3.11.

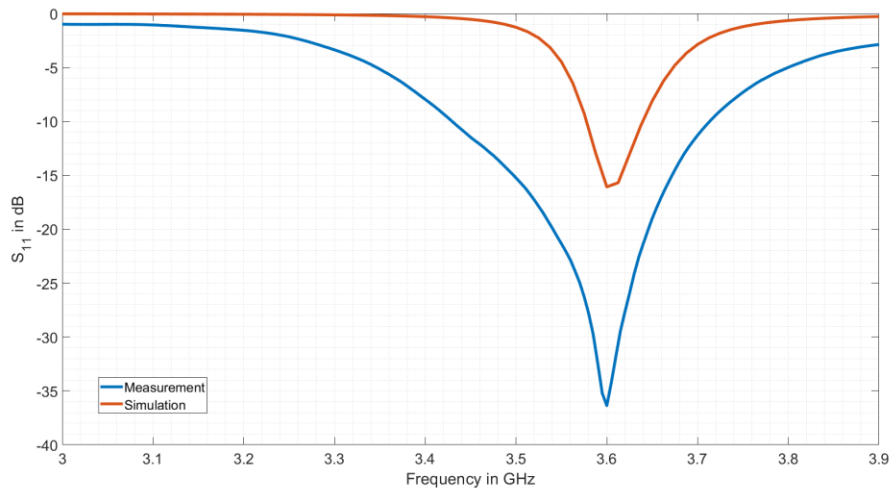


Figure 3.11 Measurement and simulation results of the S_{11} parameter of the antenna.

When S_{11} graph is examined, it is observed that the antenna resonates at 3.6 GHz. The resonance frequency of a fabricated antenna illustrates a remarkable resemblance with the simulation values. However, the measured bandwidth of the antenna is wider. The broadening of the bandwidth is due to the additional losses at the prototype antenna. As shown in Figure 3.10, the fabrication procedure adds a tremendous amount of solder metal on top of the antenna. This soldering was inevitable as it connects the shorting plane to the top plate. However, the additional metal due to soldering introduces additional losses. These losses reduce the value of S_{11} parameter and make the characteristic to look like more broadband.

The isolation performance of the antenna can be understood by inspecting the S_{21} values. The graph of measured and simulated values of S_{21} can be seen in Figure 3.12.

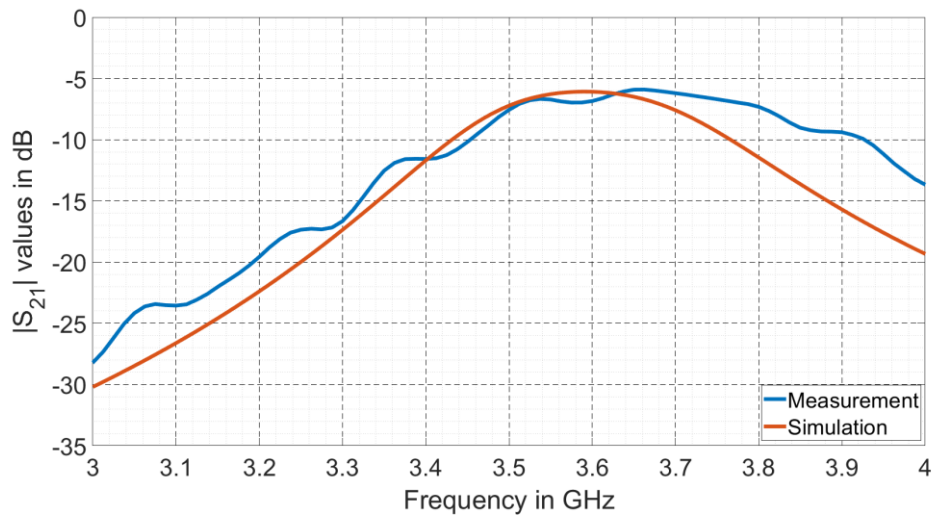


Figure 3.12 Measurement and simulation results of the S_{21} parameter of the antenna.

The fabricated antenna provides -7.5 dB isolation at 3.6 GHz frequency. The measured isolation value is enough to obtain reasonable gain values. The behavior of the S_{21} of the fabricated antenna matches with the simulation.

To fully understand the performance of the element pattern reconfigurable antenna, radiation patterns must be investigated in addition to reflection coefficients. The radiation pattern of the manufactured prototype antenna is measured at the anechoic chamber located at Middle East Technical University, Microwave and Antennas Laboratory. The visualization of the measurement setup and fabricated antenna can be seen in Figure 3.13.



Figure 3.13 Measurement setup of the antenna in the anechoic chamber.

The measurement results obtained are illustrated in Figure 3.14 to Figure 3.18 for different phase differences between ports. These figures illustrate radiation patterns at $\phi = 0^\circ$ plane when the antenna is placed in zx -plane as shown in Figure 3.13. In this placement configuration, radiation towards $\theta = 90^\circ$ corresponds the broadside direction. The antenna operates with linear polarization and only co-polarization results are illustrated.

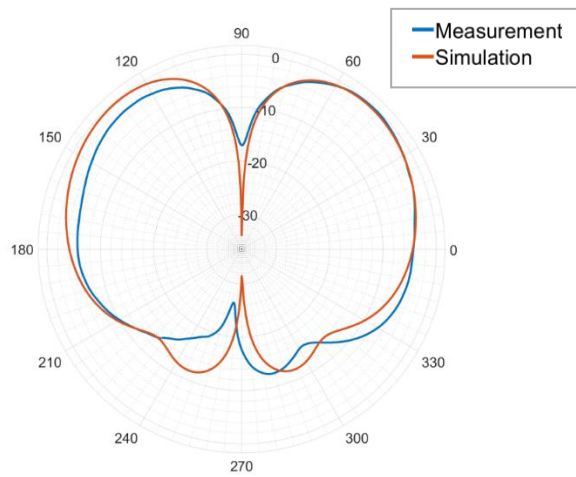


Figure 3.14 Simulation and measurement results of the antenna when 0° phase difference is applied.

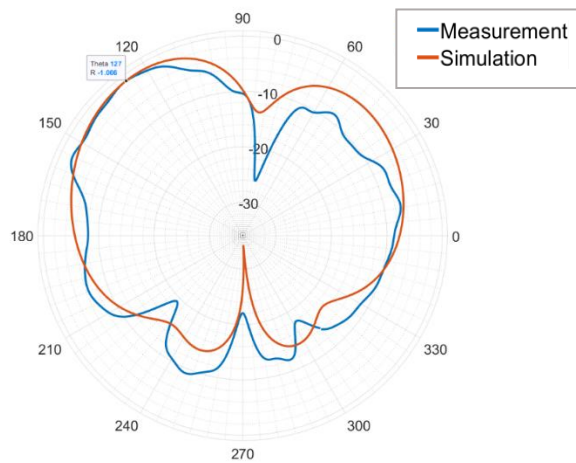


Figure 3.15 Simulation and measurement results of the antenna when 30° phase difference is applied.

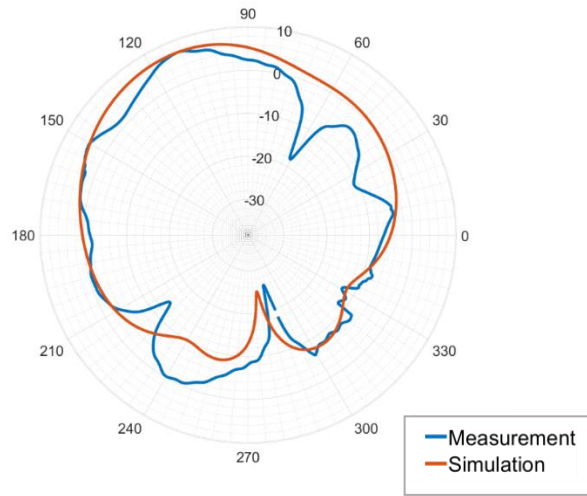


Figure 3.16 Simulation and measurement results of the antenna when 90° phase difference is applied.

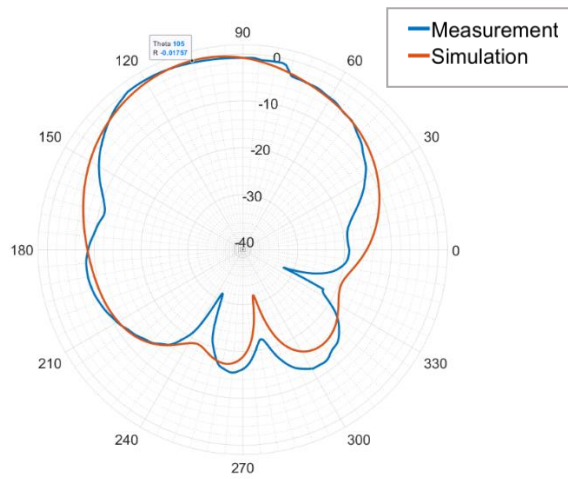


Figure 3.17 Simulation and measurement results of the antenna when 120° phase difference is applied.

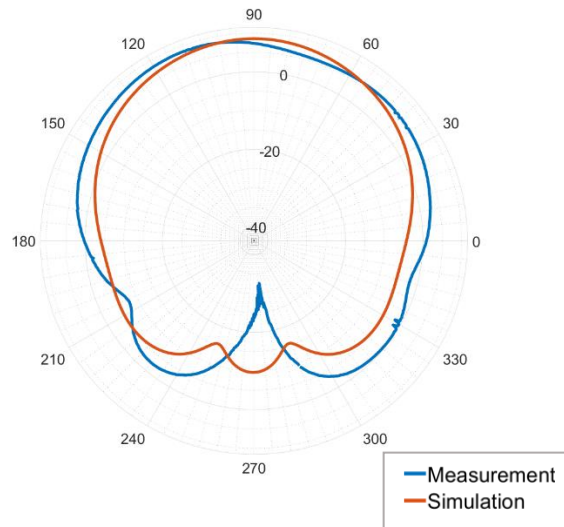


Figure 3.18 Simulation and measurement results of the antenna when 180° phase difference is applied.

When the radiation pattern measurements are examined, the pattern reconfiguring capability of the antenna element can be observed clearly. The main beam directions of the measured prototype antenna are in good agreement with the simulation results. Also, the cases where intermediate angles are scanned illustrates good agreement with the simulation results. In measurement data, there are some fluctuations and ripples in Figure 3.15 and Figure 3.16. These errors occur due to measurement setup. In the measurement chamber, the motor that rotates the antenna under test may produce unwanted physical vibrations. These vibrations result in some ripples or fluctuations in the measurement data.

In addition to the radiation pattern measurements, the maximum gains of the antenna are measured. In the gain measurements, substitution method is employed with a standard gain antenna. The gain of the antenna when for 180° phase difference is measured as 8.48 dB. The gain value in the simulation was 8.53 dB for this excitation combination. The results of the measurement illustrate a good agreement with the simulation results. The gain measurement is also done for the excitation combination when 0° phase difference is applied between ports. In this case, the measured and

simulated gains were found as; 3.83 dB and 3.85 dB, respectively. There is a perfect agreement between measured and simulated gain values.

3.6 Summary and Discussion

In this chapter, a square shorted patch antenna that is capable of pattern diversity is discussed. The presented antenna is inspired by the study in [12]. In this study, the possibility of even and odd modes were mentioned, and their characteristic properties were illustrated. However, the study [12] has drawbacks in pattern reconfiguring capability. It only investigates radiation in broadside or conical beam fashion. Within this thesis study, multiple scan angles are introduced by applying different phase differences between coaxial ports. Applying variable phase difference between ports requires a more robust feeding mechanism; so, designed antennas employ coaxial probe-type excitation.

The designed antenna consists of two sub-elements that can be excited independently. The antenna is capable of operating in two different modes as even and odd mode. One of these modes has a radiation pattern in a broadside direction, while the other one creates a conical beam. By adjusting the weights of these modes, through the applied phase difference, shorted rectangular antenna scans the main beam between 0° and 40° . As only two radiating structures are combined, beam scanning can only be done in a single plane ($\phi = 0^{\circ}$). Therefore, this design is more suitable for linear arrays.

In this chapter, design, analyses, simulation, fabrication, and measurement of the antenna are presented. Scattering parameters, radiation pattern, and gain measurements of the antenna are conducted. Good agreement between measurement and simulation results are observed.

CHAPTER 4

DESIGN, FABRICATION, AND MEASUREMENT RESULTS OF RINGED CIRCULAR PATCH ANTENNA

In this chapter, the antenna element that is capable of steering radiation beam in $\phi = 0^\circ$ plane will be discussed. The antenna in this chapter is developed so that it can employ different cavity modes simultaneously. As mentioned in Chapter 2, employing different cavity modes in a microstrip patch type antenna provides different radiation patterns. One of the radiation patterns that is directed to large elevation angles is a conical beam (monopole-like) pattern. Depending on the excited cavity mode, a planar antenna such as a microstrip patch can create a monopole-like radiation pattern. Thus, it is very charming to employ it on an element pattern reconfigurable antenna.

Microstrip patch antennas that employ different modes within a single element are discussed in the literature [21]-[24]. This chapter has inspired the studies presented in [21]. At [21], three different radiators are employed within the same antenna element. These independent radiators enable the antenna to benefit from three different TM modes. However, as this antenna must excite each radiator separately, it requires six different coaxial feed probe connectors. This number of connectors prevents the practical fabrication of the antenna and puts a minimum dimension limit to the design. The antenna studied in this chapter is created by applying important modifications to the antenna structure proposed in [21]. As the designed antenna aims to steer its radiation beam from 0° to 40° , switching between two cavity modes and their different combinations are sufficient. Therefore, the third resonator presented in [21] is removed, and the design is based on two radiators. The large number of feed points in [21] has a fabrication problem and increases the cost of the

antenna. So, the antenna designed in this thesis reduces the number of excitation ports. To be able to reduce the number of ports, an alternative method is developed. In this method, the distance between radiators is kept small so that the coupling between them would be significant. Due to the coupling between radiators, one of the radiators can be excited parasitically. Another difference from this study is made in the beam scanning capability of the antenna. The antenna presented in [21] is capable of creating two different radiation beams. The designed antenna introduces the multiple radiation beam direction with the application of phase difference between excitation ports. Also, to enable array formation with the studied antenna, this chapter focuses on antenna miniaturization techniques.

In this chapter, a ringed circular patch antenna is introduced. The radiation mechanism of the antenna is explained by revisiting TM mode concept. Also, the beam steering capability and its scan angle limits are mentioned. Then an antenna miniaturization technique is presented. Employment of this technique makes the ringed circular patch antenna a better fit for the antenna array formation. After the theoretical concepts are discussed, parametric analyses on the size of the patch structures and lumped elements are conducted. The antenna is optimized based on the experience by parametric studies. Fabrication of the prototype antenna and its performance measures are also discussed in this chapter.

The full-wave simulation software ANSYS HFSS is used to simulate and analyze antenna structures.

4.1 Antenna Structure

The ringed circular patch antenna is a microstrip patch type antenna that consists of two different radiators, which are co-centrally placed, a ring and a circular patch. Pattern diversity is obtained by exciting different TM modes for different radiators. The main challenge in the design was to coincide the operating frequency bands of these different TM modes. The geometry of a ringed circular patch antenna can be seen in Figure 4.1.

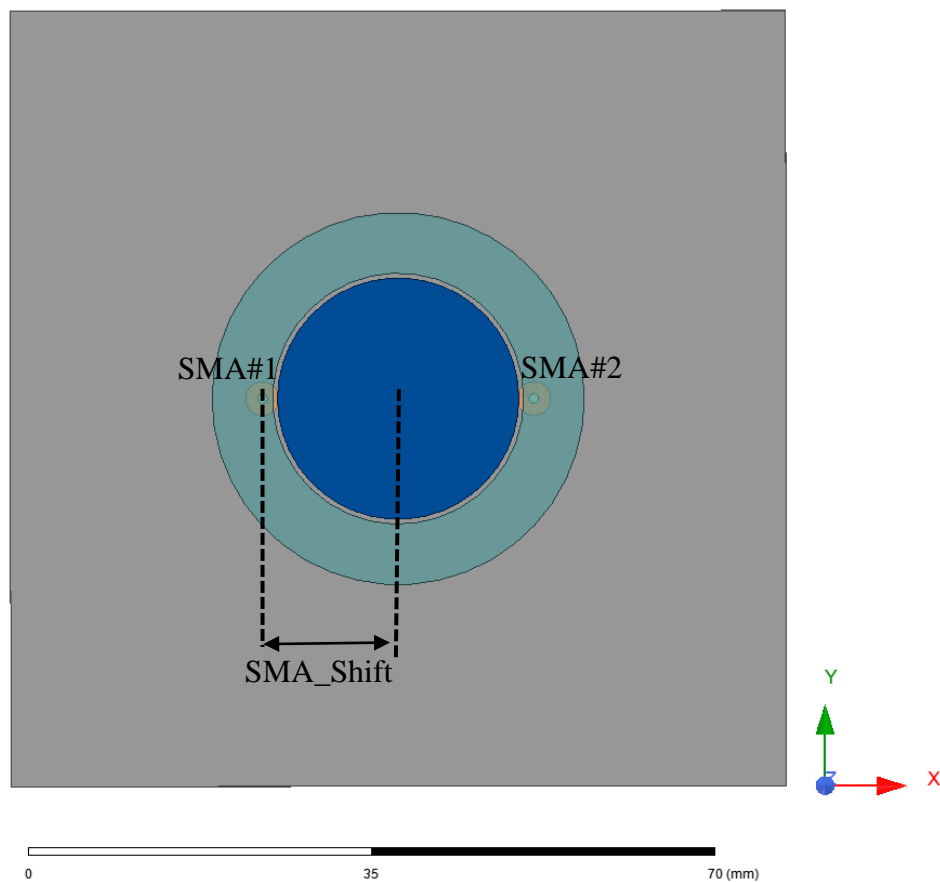


Figure 4.1 Geometry of a ringed circular patch antenna.

The dimensions of the antenna are optimized to excite the appropriate TM mode for each resonator. The physical dimensions of the optimized antenna are summarized in Table 4.1.

Table 4.1 Dimensions of the ringed circular patch antenna

Parameter	Value
Circle_Patch_Radius	12.45 mm
Ring_Patch_Inner_Radius	12.95 mm
Ring_Patch_Outer_Radius	19.5 mm
SMA_Shift	15.75 mm
Substrate Size	80mm x 80mm
Substrate Height	1.524 mm
Substrate Material	Rogers 4003 ($\epsilon_r = 3.38$)

4.1.1 Selection of Radiators and Geometry of the Antenna

The antenna contains circular and ring-shaped patch structures. The first step in the design was to determine the size of the circular patch antenna. The antenna is required to excite TM_{11} mode at 3.6 GHz. The following formulas given in [3] are used to determine the radius of the circular patch antenna.

$$r = \frac{F}{\left\{1 + \frac{2h}{\pi\epsilon_r F} \left[\ln\left(\frac{\pi F}{2h}\right) + 1.7726 \right] \right\}^{0.5}} \quad \text{where } F = \frac{8.791}{f_r \sqrt{\epsilon_r}} \quad (4.1)$$

In this equation r , f_r , ϵ_r and h denotes; the radius of the circular patch, resonance frequency in GHz, the dielectric constant of the substrate, and thickness of the substrate in cm, respectively. When the formulation is applied for the Rogers 4003 substrate ($\epsilon_r=3.38$) radius of the circular patch is found as 12.69 mm. In the simulation environment, this radius value results in a slight deviation in the resonance frequency. The radius of the circular patch is optimized to be 12.45 mm after conducting parametric studies on this dimension.

The second resonator that is designed is a ring-shaped patch structure. In order to create pattern diversity, monopole-like (conical beam) radiation performance is desired from this radiator. The conical beam performance is obtained when the ring patch is excited in its TM_{21} mode. The antenna design and its dimensions are conducted to obtain the TM_{21} mode of operation. Since the antenna contains only one layer, the inner radius of the ring antenna depends on the radius of the circular patch antenna. Otherwise, they coincide. The radius of the circular patch antenna was determined as 12.45 mm. As the close coupling between the ring and circular patch antenna is desired, the distance between radiators is kept small. The distance between radiators is selected as 0.5mm. This distance between radiators is studied parametrically, and 0.5mm is the optimal point for efficient coupling. The results of these parametric studies will be presented in the following sections. After determining the inner radius of the ring-shaped patch antenna as 12.95 mm, a set of approximate formulas are employed to determine the outer radius of the ring-shaped patch antenna. The formulations taken from [29] can be shown as;

$$k = \frac{2n}{a + b} \quad \text{and} \quad f_r = \frac{ck}{2\pi\sqrt{\epsilon_{eff}}} \quad (4.2)$$

In this formula, abbreviations n , a , b , c , k and ϵ_{eff} represents; TM mode number, the inner radius of the ring patch, outer radius of the ring patch, speed of light, wave

number, and effective dielectric constant of the substrate, respectively. Since the TM_{21} mode is desired for the ring resonator, n is selected as 2. The inner radius of the patch and the speed of the light were predefined quantities, and the effective dielectric constant is calculated by employing the formula in reference [3]. The outer radius of the ring-shaped patch remains only unknown in (4.2). When the equations are solved for the outer radius of the ring patch, b is obtained as 18.86 mm. The outer radius of the ring patch also illustrates a minor frequency shift in the simulation environment. The resonance point of the ring patch is adjusted to 3.6 GHz by conducting a parametric study. The outer radius of the ring antenna is obtained as 19.5 mm as a result of this parametric study.

4.1.2 Antenna Feed Structures and Their Optimization

One of the critical points of this antenna design is concentrically having two radiators. The structure of the concentric alignment of the radiators enables excitation of the circular patch with coupling. The circular patch does not have any direct excitation connection. This patch is excited parasitically by two probes connected to the outer ring. Therefore, the antenna has only two excitation ports.

The ringed circular patch antenna is fed by coaxial probes. These coaxial probes can be seen in Figure 4.1 with SMA#1 and SMA#2 notations. The position of the SMA port on the ring-shaped patch plays a vital role in the matching performance of the antenna. The location of the feed point on the x-axis determines the S parameters of the related port. The parametric study on S_{11} is illustrated in Figure 4.2.

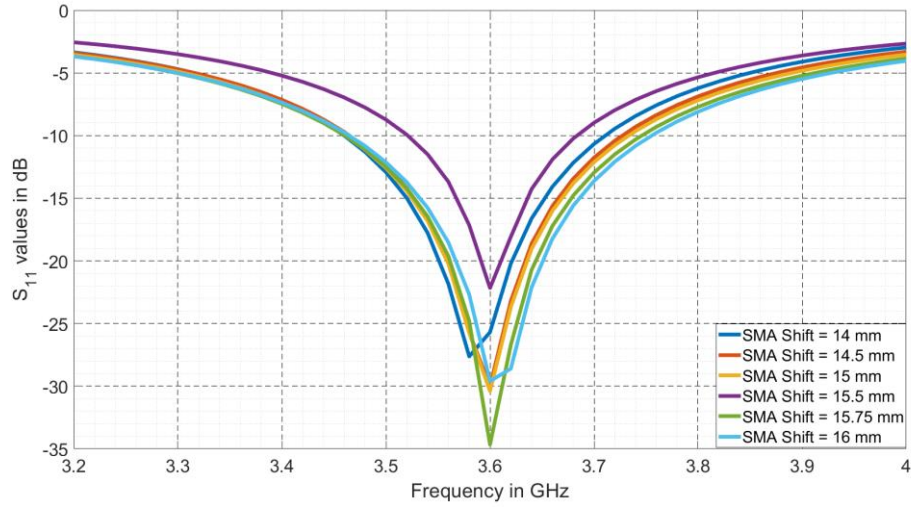


Figure 4.2 Parametric study on the location of the SMA#1 port.

In this study, the SMA_Shift variable represents the position of the SMA ports with respect to the center of the patch. In light of this parametric study, the SMA_Shift is selected as 15.75 mm as it results in minimum reflection from ports.

Apart from the matching performance of the antenna, positions of SMA ports with respect to each other also have importance. SMA ports are connected to the ring-shaped resonator so that they make 180° angles with respect to each other, as shown in Figure 4.1.

4.2 Miniaturization of the Antenna

The ringed circular patch antenna has an outstanding performance in pattern reconfiguring property. However, the overall size of the antenna is large for array applications. The maximum dimension of the antenna is $0.46\lambda_0$. As at conventional array structures, the inter-element separation should not be larger than $0.5\lambda_0$, this antenna needs to be miniaturized. Although the size of the antenna is smaller than

the limitations, due to interference problems, this antenna is not the right candidate for arrays. In this part, the method that can reduce the size of the antenna will be discussed. Also, the simulation and measurement results of the miniaturized antenna will be presented.

Antenna miniaturization is achieved by connecting lumped capacitors to the ring-shaped patch antenna. Connection of the capacitors is conducted so that one port of the lumped capacitor touches to the ring patch while the other port of the capacitor is connected to the ground plane with a via structure. The top view of the miniaturized antenna can be seen in Figure 4.3.

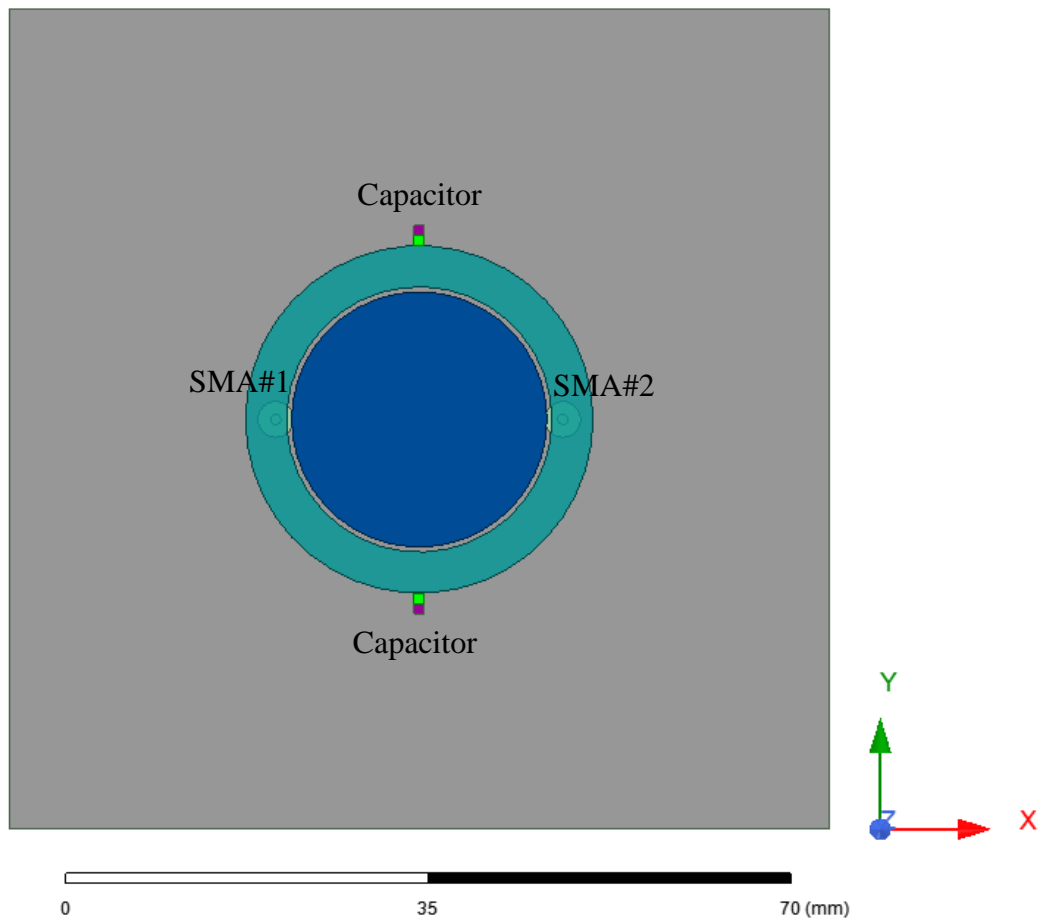


Figure 4.3 Top view of the ringed circular patch antenna.

Like a non-miniaturized antenna, two connectors feed the antenna structure. These connectors can be seen in Figure 4.3 as SMA#1 and SMA#2. Also, chip capacitors are connected to the outer ring structure. These capacitors are denoted as Caps. The physical sizes of the miniaturized antenna structure and capacitor values are given in Table 4.2.

Table 4.2: Dimensions of the miniaturized antenna and value of the capacitors

Name of the quantity	Value
Circle_Patch_Radius	12.45 mm
Ring_Patch_Inner_Radius	12.95 mm
Ring_Patch_Outer_Radius	17 mm
Caps	0.68 pF
Substrate Size	80mm x 80mm
Substrate Height	1.524 mm
Substrate Material	Rogers 4003

The main idea behind antenna miniaturization can be explained by the transmission line model. According to the transmission line model, radiating edges of the antenna can be modeled as impedance surfaces. The input impedance of the antenna depends on the impedance value of these edges. Adding chip capacitors to the radiating edge modifies this impedance value. The capacitor value can be tuned to obtain a smaller-sized antenna.

The ring antenna that initially resonates at a higher frequency is tuned to resonate at a lower frequency with the help of the capacitors. The capacitors that are mentioned are connected to the upper and lower sides of the ring-shaped antenna and are shown in Figure 4.3.

Corresponding capacitor values affect the resonance frequency of the antenna. The effect of the lumped capacitor is that the higher the capacitance value is used, the

lower the resonance frequency can be obtained. This phenomenon can be seen in Figure 4.4.

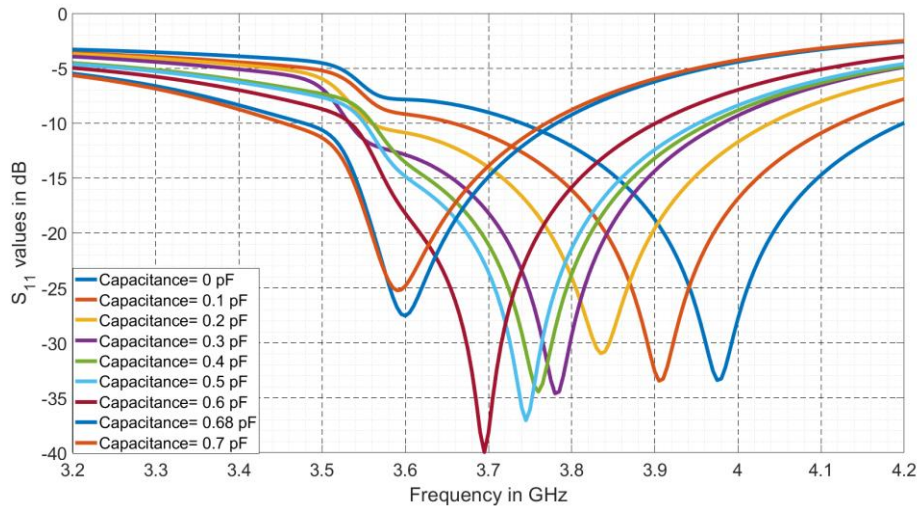


Figure 4.4 S Parameters with respect to frequency when different capacitors (0-0.7 pF) are connected to the ring patch.

As shown in Figure 4.4, when the capacitance value is increased, the resonance frequency of the antenna reduces. By connecting 0.68pF to the antenna, the outer radius of the antenna is reduced to its 88%.

4.3 Simulations and Parametric Studies

The performance of the designed concentric antenna is dramatically affected by the changes in the antenna dimensions. The resonance frequency of a circular patch antenna is determined by the radius of the conductor and the permittivity of the substrate. However, as the circular patch is excited parasitically, the resonance

frequency of the antenna also depends on the separation between the ring and circular patches.

The effect of the distance between radiators is observed by inspecting different separation distances. In this parametric study, the inner and outer radius of the ring patch are kept constant while the radius of the circular patch is swept. Inter element distance is arranged with the radii of the circular patch. Figure 4.5 and Figure 4.6 show the S_{11} parameters. This parametric study is plotted on two different graphs. Figure 4.5 illustrates the S_{11} results when the distance between radiators is larger than 0.5 mm. While in Figure 4.6, the distance between radiators that is smaller than 0.5 mm is investigated.

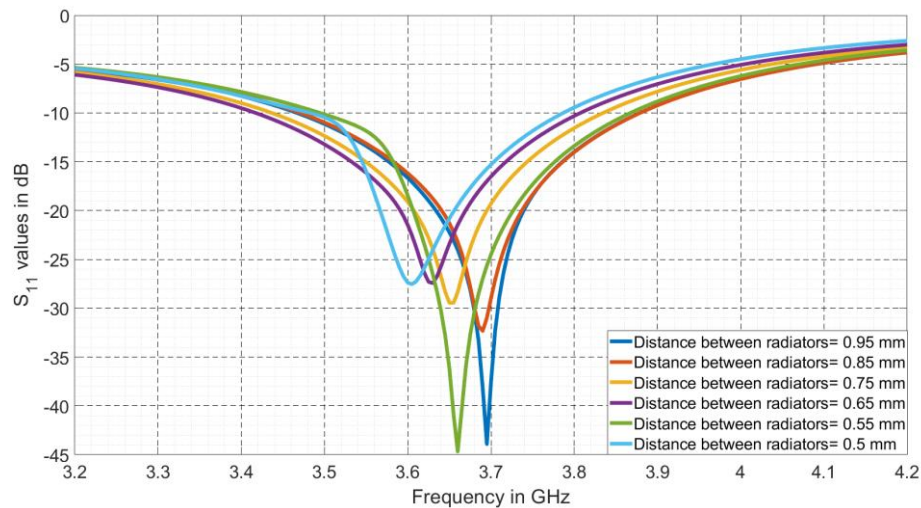


Figure 4.5 Scattering parameters (S_{11}) with respect to frequency for different distances between radiators (0.95-0.5 mm).

In this figure, the effect of the radius of the circular patch on the resonance frequency can be observed. When the size of the antenna is increased, the resonance frequency decreases. This result meets with expectations.

Figure 4.5 shows that desired resonance frequency is achieved when the separation between radiators is 0.5mm. This value has a vital role in our design. If the separation

between circular and ring patch is shrunken further, a large shift at the resonance frequency is observed.

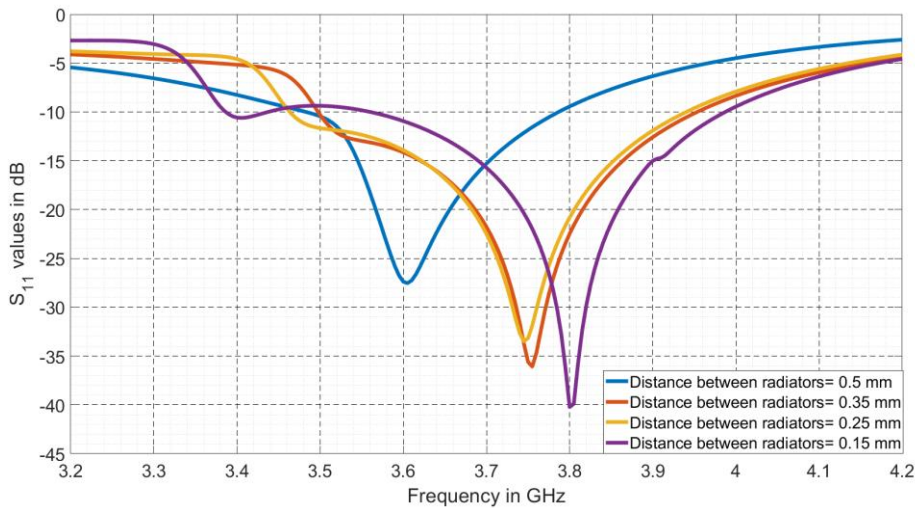


Figure 4.6 Scattering parameters (S_{11}) with respect to frequency for different distances between radiators (0.5-0.15 mm).

The large shift in resonance frequency can be explained by extensive coupling between radiators. When the separation between radiators is larger than 0.5mm, the ring couples its currents to the circular patch successfully. However, when the separation between ring and circular structure is too small, they tightly couple to each other. This strong coupling limits the current flow of the circular patch. The current distributions on the circular patch are reduced. The current distributions of this tight coupling can be seen in Figure 4.7a. In comparison, the current distributions of the optimized antenna with a 0.5mm distance between radiators are illustrated in Figure 4.7b.

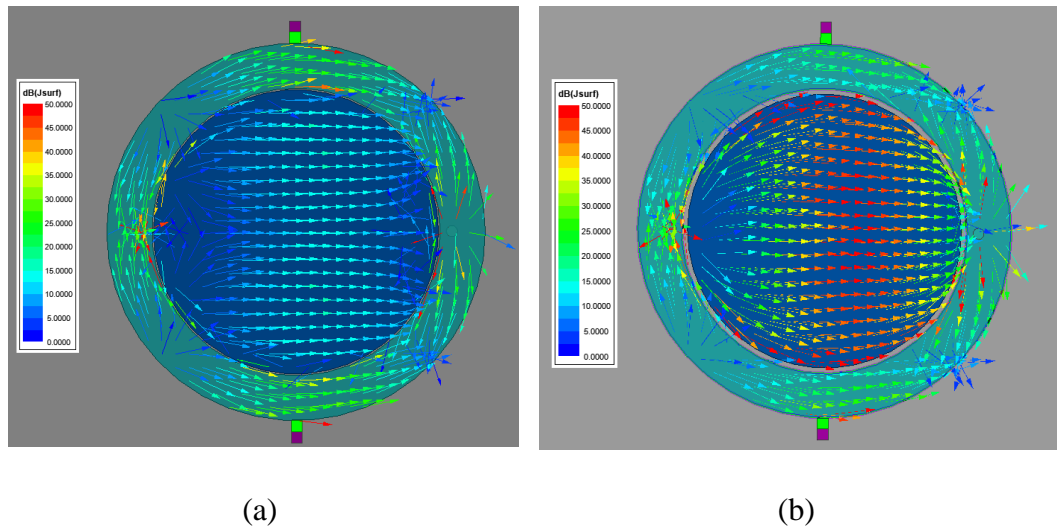


Figure 4.7 Current distributions on patches when distance radiators is 0.15 mm(a) and 0.5mm(b).

The induced surface currents have lower amplitude when the separation between circular and ring-shaped antennas is made smaller than 0.5 mm. The reduction in the amplitude of the currents can be seen in Figure 4.7a. Therefore, distances smaller than 0.5 mm is not preferable.

4.4 Radiation and Beam Scanning Phenomenon of the Antenna

Another critical achievement of the design is observed at the resonance frequency of the patch structures. The desired modes would be TM_{21} for ring-shaped and TM_{11} mode for the circular-shaped patch. In other words, this antenna simultaneously operates with two different resonators, one of them operates in TM_{11} and the other one operates in TM_{21} mode. While providing this operation, the TM modes resonate precisely at the same frequency. Radiation patterns of TM_{11} and TM_{21} can be seen in Figure 4.8.

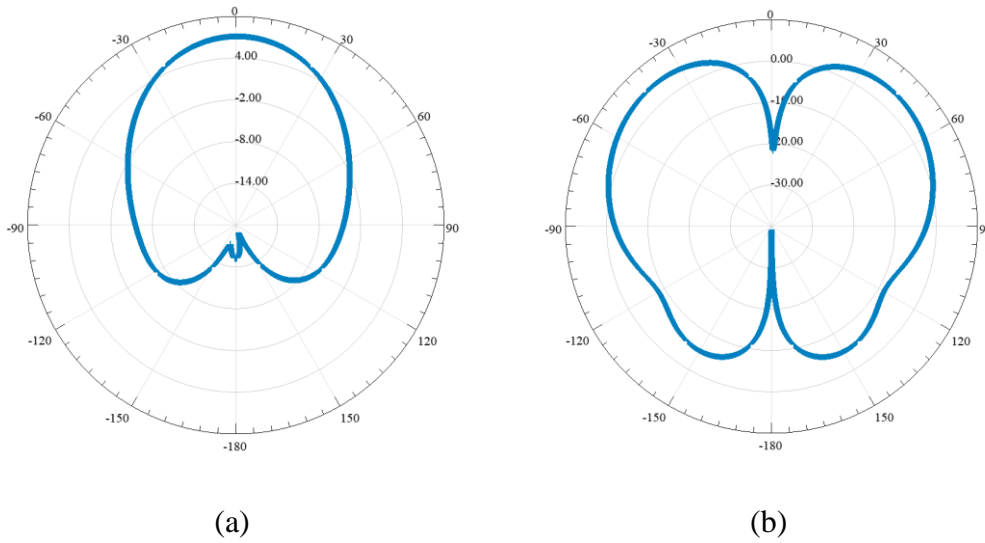


Figure 4.8 Radiation patterns of TM_{11} (a) and TM_{21} (b) modes in microstrip patch antennas in dB scale.

It is shown in Figure 4.8 that TM_{11} mode directs its beam to the broadside direction ($\theta = 0^\circ$) while TM_{21} creates a conical beam in which the maximum radiation direction is $\theta = 40^\circ$. Switching between these two modes enables the beam steering to either $\theta = 0^\circ$ or $\theta = 40^\circ$ angles. However, an element pattern steerable antenna must be able to direct its radiation beam towards all angles that reside within its range. Therefore, the designed antenna must also scan the angles between $\theta = 0^\circ$ and $\theta = \pm 40^\circ$. To achieve scanning towards intermediate angles, different combinations of the TM modes are necessary. These combinations not only include amplitude differences between modes, but they also involve phase differences between them. The phase difference between TM_{11} and TM_{21} modes forms a superposition of two-element where the element patterns are different. This relationship enables a user to steer the beam in any direction between $\theta = 0^\circ - \pm 40^\circ$ range.

The two independent feed port structure enables control of both phase and amplitude on the TM_{11} and TM_{21} modes. For example, when no phase difference is applied between SMA#1 and SMA#2, only the ring structure is excited. The induced currents on the circular patch oppose each other. Therefore, the net current on the circular patch sums to negligible values. The current distribution of this excitation can be observed in Figure 4.9a.

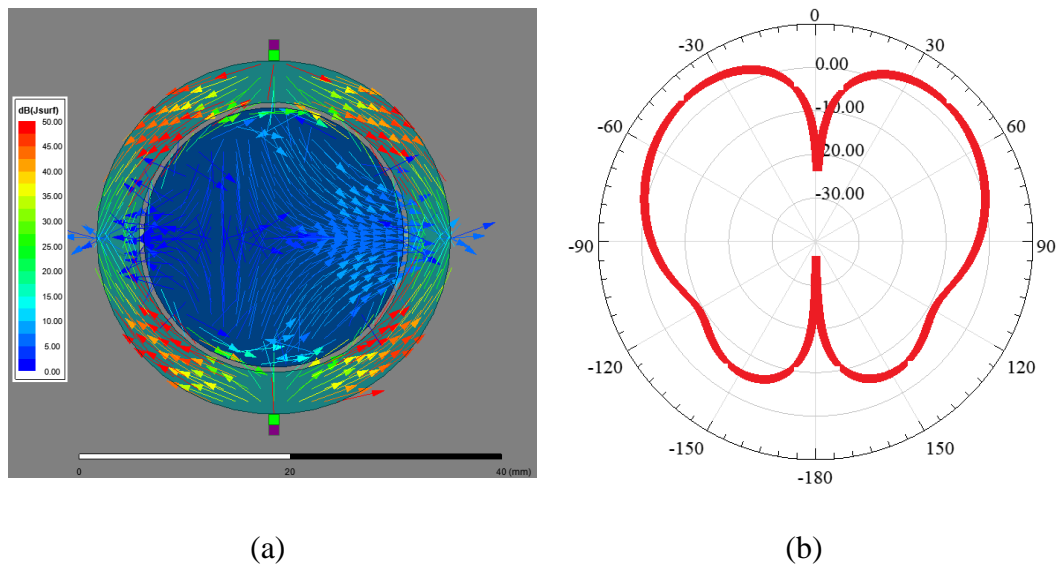


Figure 4.9 Current distributions (a) and resultant radiation pattern (b) when the phase difference between ports is arranged as 0° .

On the other hand, the antennas pronounce the TM_{11} mode of the circular patch when the applied phase difference between SMA#1 and SMA#2 is 180° . When the ports are excited in out of phase manner, the current null points on the ring patch are shifted. As the null points shift, the currents on the ring-shaped patch also change their direction. At this point, the ring patch does not have a specific TM mode as the feed points distort the current distribution of TM_{21} . The radiation characteristic of

the ring-shaped patch is distorted. However, this feeding scheme creates an advantage to the circular-shaped patch. By benefiting from the absence of the TM_{21} currents on the ring patch, the circular patch can now induce a net current on itself. The induced current illustrates the characteristics of the TM_{11} mode of the circular structure. So the radiated field of the antenna would be in the broadside direction. The illustration of the current distributions on the antenna element and the resultant radiation pattern can be found in Figure 4.10.

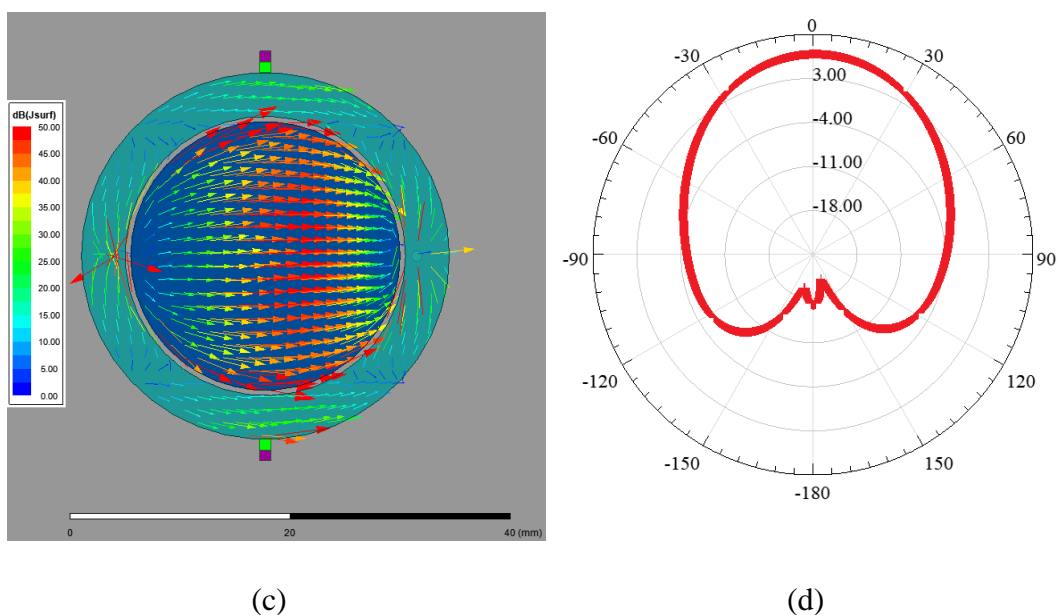


Figure 4.10 Current distributions (a) and resultant radiation pattern (b) when the phase difference between ports is 180° .

In order to scan the angles between 40 and 0 degrees, intermediate phase values will be applied. In this study, SMA#2 is kept at zero phase, and the phase difference is applied to SMA#1.

In order to better understand the phase concept, investigating the case where the input of SMA#1 lags 90° should be discussed. In this case, as there is a phase difference between the ports, the ring structure would not have a perfect TM_{21} mode of

excitation. The disturbance at the TM_{21} mode enables the inner circle to excite itself with a net surface current. As mentioned above, the central circle operates at TM_{11} mode due to its radius, no matter how it is excited. If the two sources mentioned above are expressed separately, the overall antenna can be modeled as two sources with different excitation amplitude and phase. As the left portion of the ring-shaped patch lags, the overall pattern is directed towards the lagging port direction. The visualization of this phenomenon can be found in Figure 4.11a. As can be seen in the current distribution, the circular patch is excited parasitically. Due to the phase difference between excitations, the phase of surface currents also changes. The radiation pattern of antenna element when 90° phase difference is applied can be seen in Figure 4.11b.

The different combinations of TM_{11} and TM_{21} modes can be understood by inspecting their surface current densities. In Figure 4.12, current distributions of several feeding combinations are illustrated.

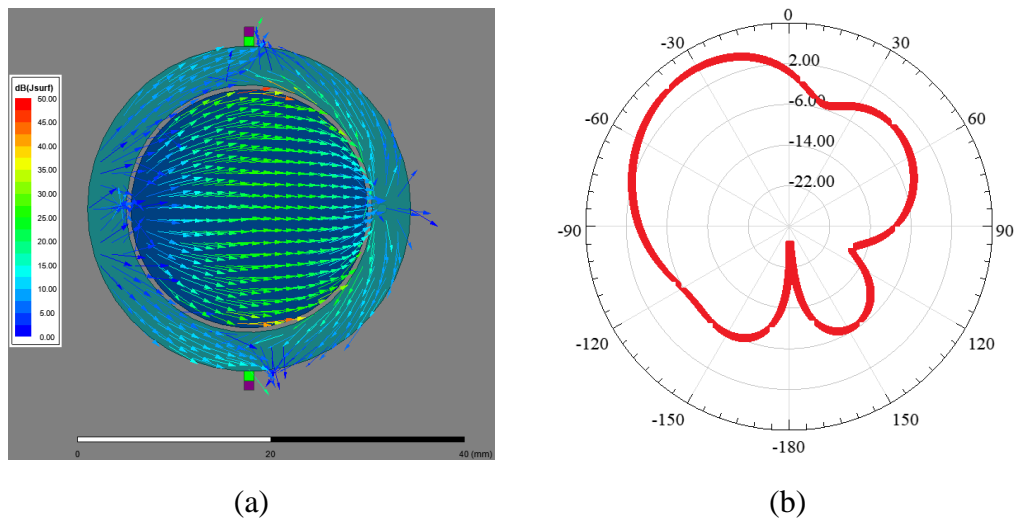
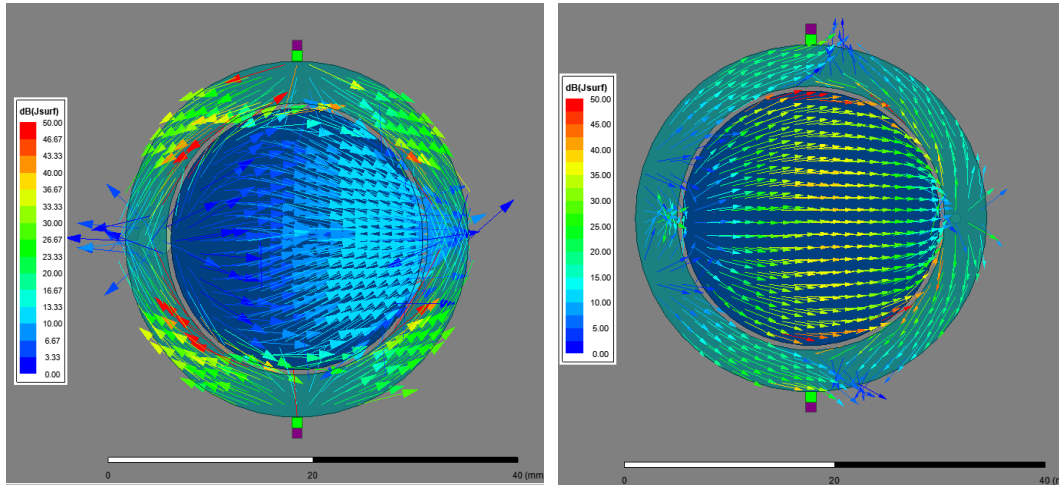


Figure 4.11 Current distributions (a) and resultant radiation pattern (b) when the phase difference between ports is 90° .



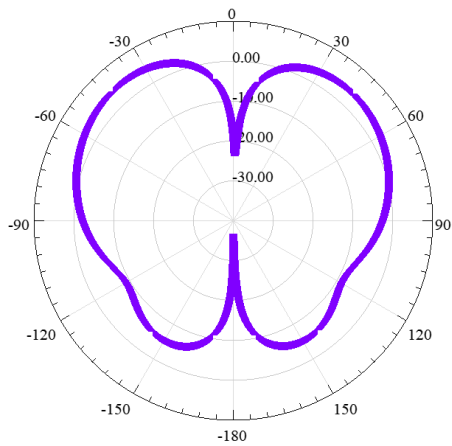
$$\beta = 30^{\circ} \text{ (a)}$$

$$\beta = 120^{\circ} \text{ (b)}$$

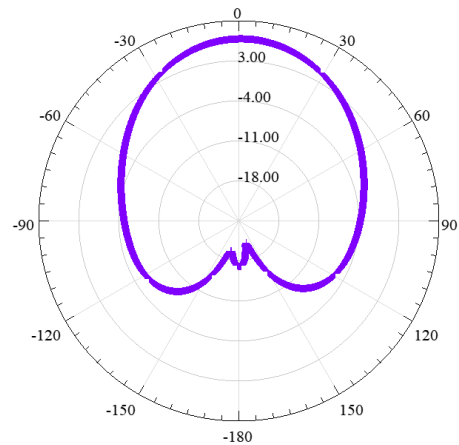
Figure 4.12: Current distributions of patches when different phase differences (β) are applied.

The antenna radiates close to the broadside direction if TM_{11} mode is excited more dominantly. This case occurs when applied phases from ports are between 90° and 180° degrees. One example of this case can be seen in Figure 4.12b. In this case, 120° degrees of phase difference is applied between ports. As this phase is closer to 180° degrees, the dominant mode is TM_{11} mode. The dominance of TM_{11} can be understood by inspecting strong currents in the circular patch. Although there are diagonal currents at the ring structure representing TM_{21} mode, the currents in the circular patch that represent the TM_{11} mode dominate. Therefore, the beam is steered to 15° , which is closer to the broadside direction than the maximum of the conical beam. This phenomenon also applies in the reverse direction. When the applied phase difference is closer to 0° , the TM_{21} mode on the ring patch dominates. An example of this situation is given in Figure 4.12a. In this case, a 30° phase difference is applied. This phase difference is close to 0° , and thus it excites TM_{21} mode stronger than the TM_{11} mode. As a result, the beam is steered to 30° , which is closer to the maximum radiation direction of the conical beam.

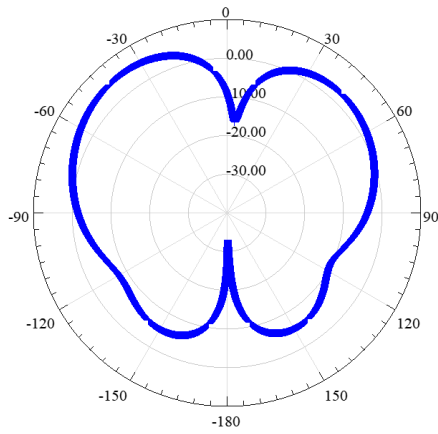
As mentioned before, by applying phase difference, the radiation beam can be scanned toward each direction within $\theta = \pm 40^\circ$ range. In order to scan the beams towards a positive θ direction, the phase difference must be reversed. In these operations, the excitation from SMA#2 port must lag. The simulation results of radiation patterns are given in Figure 4.13 for various phase difference (β) values.



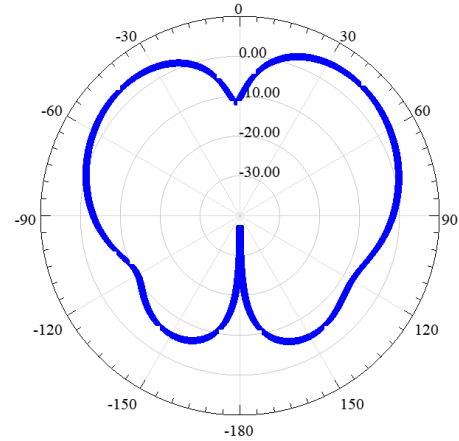
$\beta = 0^\circ$ (a)



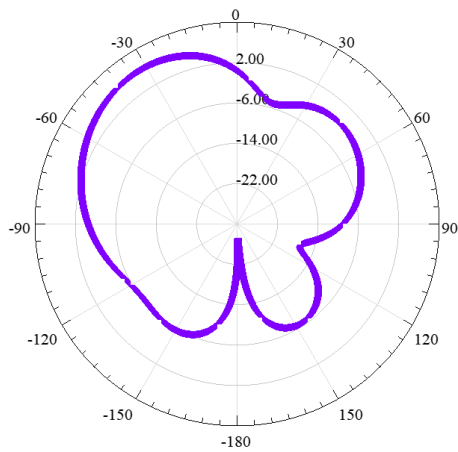
$\beta = 180^\circ$ (b)



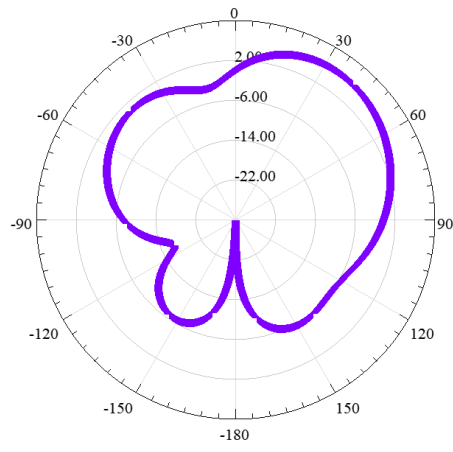
$\beta = 30^\circ$ (c)



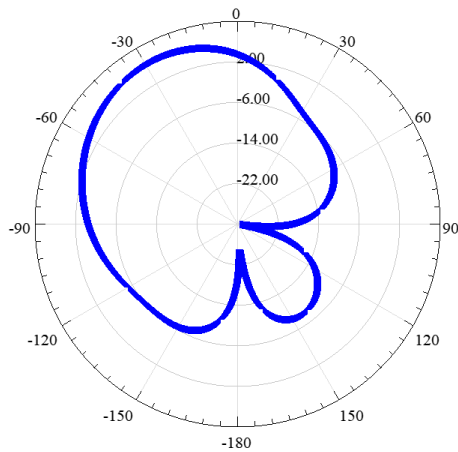
$\beta = -30^\circ$ (d)



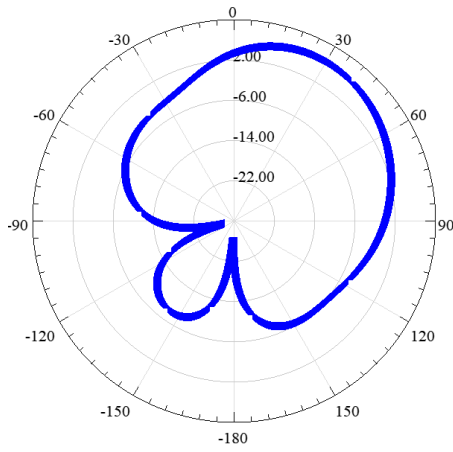
$\beta = 90^\circ$ (e)



$\beta = -90^\circ$ (f)



$\beta = 120^\circ$ (g)



$\beta = -120^\circ$ (h)

Figure 4.13 Radiation patterns of the antenna at $\phi = 0^\circ$ plane for various β values.

4.5 Isolation Considerations and Enhancement

The miniaturized antenna design employs two SMA ports as an excitation. These two ports are connected to the same ring-shaped radiator. As two ports have a direct electrical link, the isolation between ports becomes poor. The lack of isolation of ports can be observed from S_{21} graph of the design. In Figure 4.14, the S parameters of the antenna can be seen.

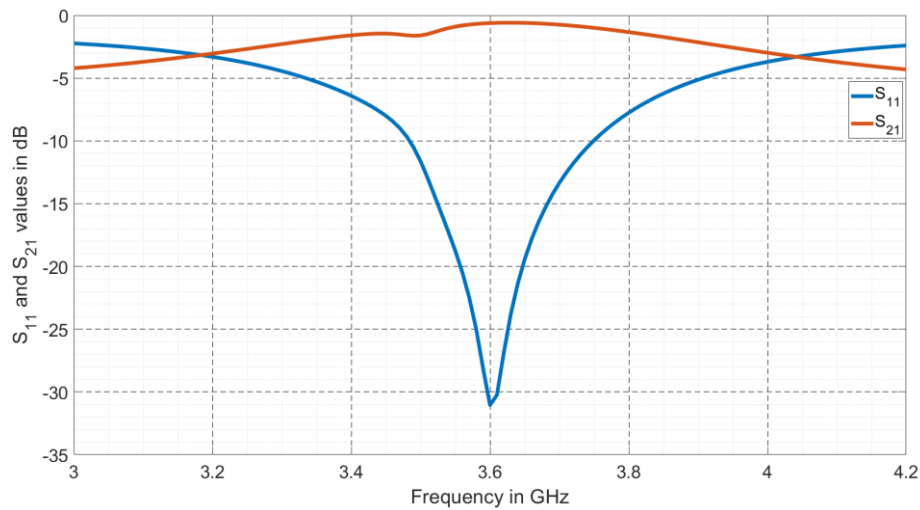


Figure 4.14 S_{11} and S_{21} parameters of the antenna.

To understand the isolation performance between ports, one must investigate S_{21} values of the antenna. When Figure 4.14 is investigated, the S_{21} value is obtained as -0.62 dB at 3.6 GHz. This value is not sufficient to prevent the coupling between ports. The high value of S_{21} creates an isolation problem in the antenna. As the ports create a direct link between them, a considerable portion of the input power travels to the other port. This phenomenon reduces the radiation efficiency of the antenna and results in reductions in the realized gain of the antenna.

As the isolation problem reduces the gain of the designed antenna, it needs to be improved. In the following parts, three different methods developed to reduce coupling between ports will be discussed. The idea of these methods is to disturb

current densities on the ring structure without changing the radiation pattern of related TM_{21} mode. As the primary constraint is not to disturb the radiation pattern of the TM_{21} mode, the dominant characteristics of the currents on the ring structure should not change. Therefore, the modifications in the ring structure are applied at the current null locations of the ring.

To increase the isolation between ports, creating ground connections to the ring structure is considered as the first method. In this structure, small conducting plates are placed at current null locations of the ring-shaped patch structure. The visualization of this antenna is illustrated in Figure 4.15.

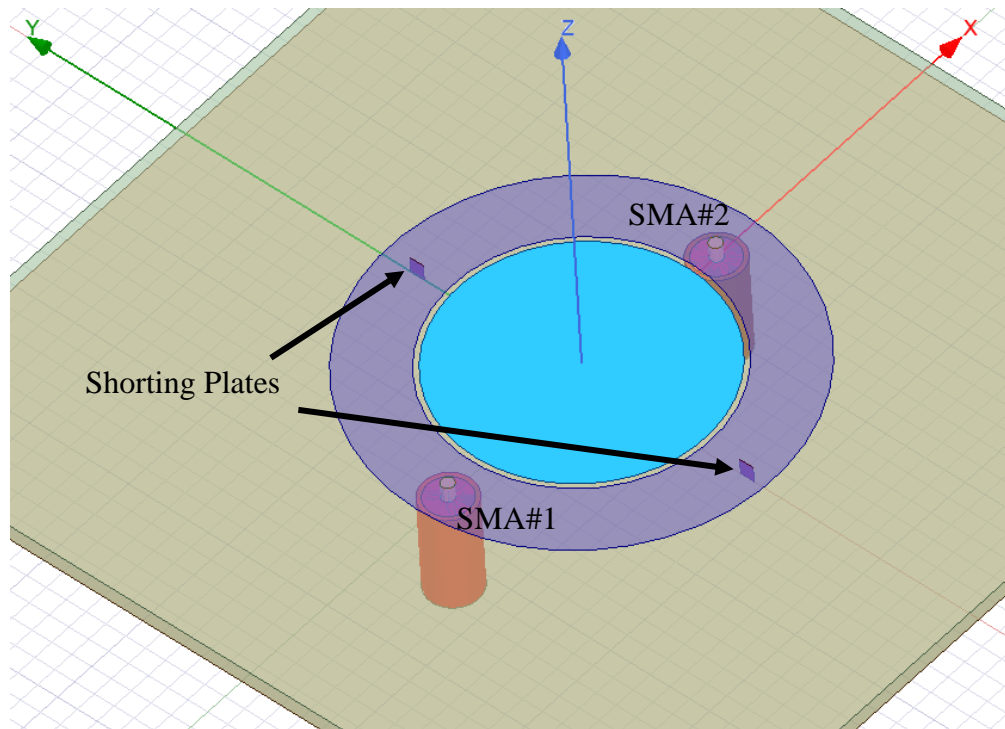


Figure 4.15 Isometric view of the shorted antenna.

This method slightly improved the isolation performance of the antenna. However, as the surface currents have small amplitudes on the shorting plates, the provided isolation is insufficient to improve antenna gain.

The first method to increase isolation highlights the necessity of the surface current disturbance. In the second isolation method, surface currents on the ring-shaped patch are tried to be reduced by employing slot structures. The purpose of the slots in this design is to minimize the direct current paths between ports. The slots are placed so that they only prevent the current leakage between ports. Slots are located on the y axis. Therefore, the current distribution of TM_{21} mode is not disturbed.

In the third method, the idea of slots is improved. In this design, slots are enlarged so that the ring-shaped structure is divided into two arc-like radiators. The top view visuals of these two methods can be seen in Figure 4.16.

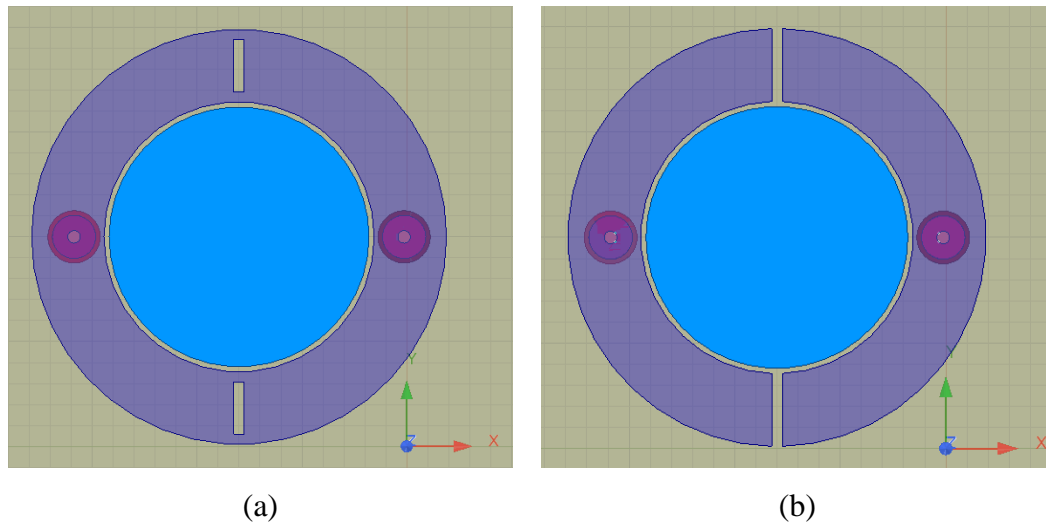


Figure 4.16 Top view of the antennas studied in the second and third isolation methods.

The third method reduces the leakage currents between ports. In this study, the distance between two arc-shaped conductors is arranged as 2 mm. This distance must be kept small to preserve the conical-shaped radiation pattern of the TM_{21} mode.

The performances of three different isolation methods can be compared by inspecting S_{21} performances. The graph that presents the comparison between isolation enhancement methods can be seen in Figure 4.17.

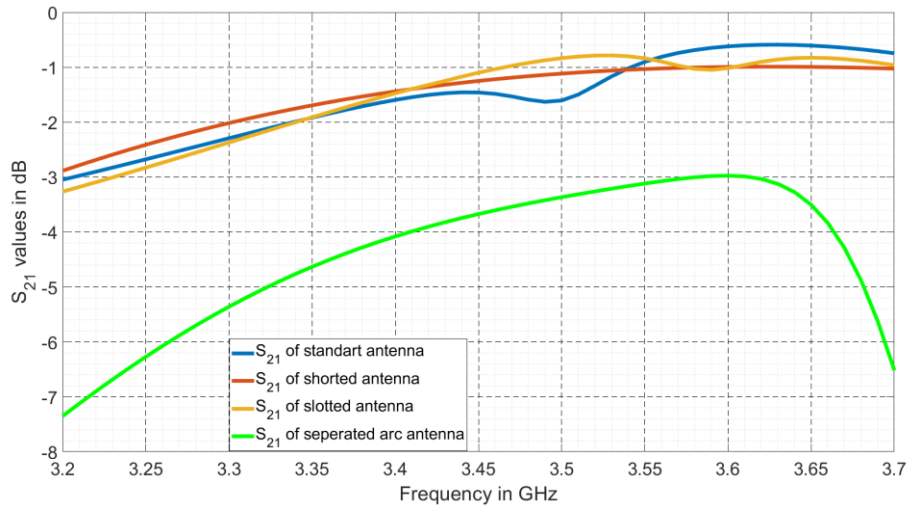


Figure 4.17 Comparison of S_{21} values of different isolation enhancement methods.

As it can be observed from the figure, the lowest S_{21} value at 3.6 GHz can be achieved by separating the ring-shaped structure into two arc-shaped structures. However, the lowest possible S_{21} is still -3 dB. This value could not be reduced further.

4.6 Fabrication of a Prototype Antenna

In the fabricated prototype, Rogers 4003 dielectric substrate with 1.524 mm thickness and 35 μ m thick conductor is used. The geometry that is illustrated in Figure 4.3 is fabricated with dimensions given in Table 4.2, as shown in Figure 4.18.

The radius of circular patch and the distance between the circular and ring patch structures significantly impact resonance frequency. Therefore, the accuracy of fabrication is a crucial part of the process. In the milling process, the LPKF needle plays an important role. Due to the conical shape of the needle, substrate thickness may change at the edges of the patches. These thickness changes at the patch sides also have an essential effect on the resonance frequency as thickness changes affect the effective permittivity of the substrate. Considering the limitations of the LPKF machine, the fabrication errors are simulated to see the effect of extra milling thickness. The visualization of the simulated parameter can be seen in Figure 4.19.

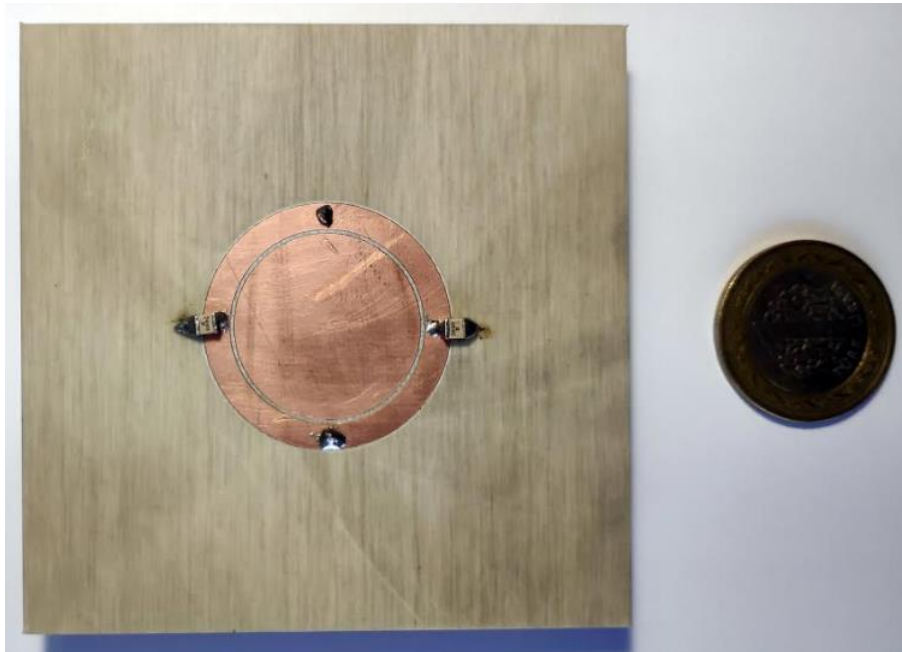


Figure 4.18 Fabricated prototype of the ringed circular patch antenna.

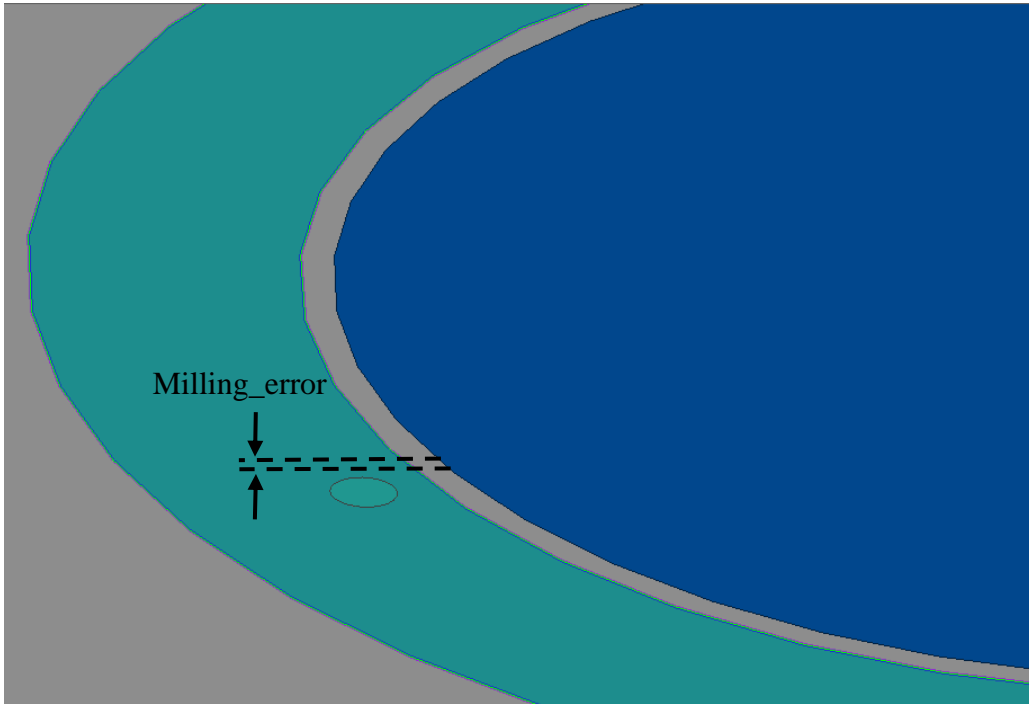


Figure 4.19 Representation of milling_error between circular and ring-shaped radiators.

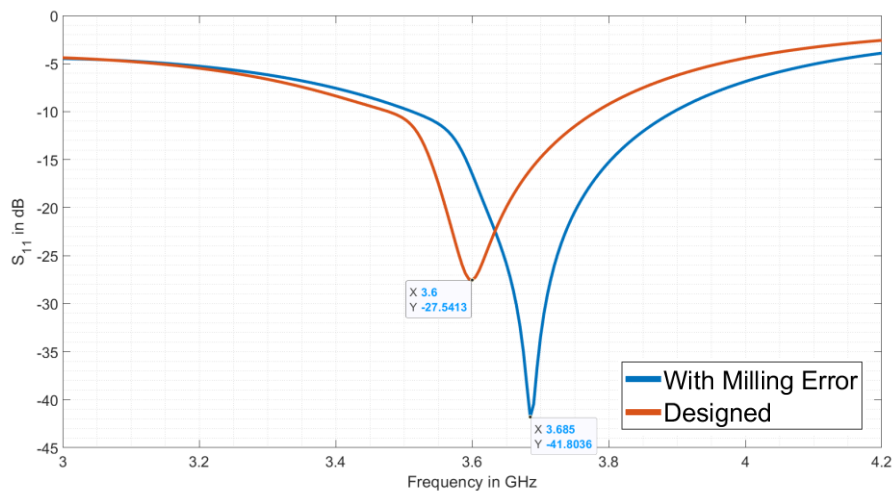


Figure 4.20 Input return loss of the designed antenna and the antenna with 0.5 mm milling error.

Milling error is selected as 0.5 mm, as this value is the maximum possible error of the process. The possible frequency shift due to this error can be seen in Figure 4.20.

A fabricated antenna involves two chip capacitors. These capacitors are soldered to a via to enable a capacitive path between the upper ring patch and the lower ground plane. This process involves soldering via hand; thus, it introduces a critical fabrication issue. The position of the soldering point and its homogeneity plays an essential role in the resonance point of the ring patch.

As a connector, panel type coaxial SMA connector is preferred. The outer conductor of this connector is soldered to the ground plane, while the inner conductor is soldered to the upper ring patch.

4.7 Measurement Results

Reflection coefficients of the fabricated antenna are measured at Microwave and Antennas Laboratory of Middle East Technical University. The scattering parameters are measured by employing a network analyzer (Keysight E5071C). The graph that compares simulation and measurement results of the scattering parameters is given in Figure 4.21. In this figure, only S_{11} parameters are illustrated. As the geometry of the antenna is symmetrical, it illustrates similar results when the second port is measured.

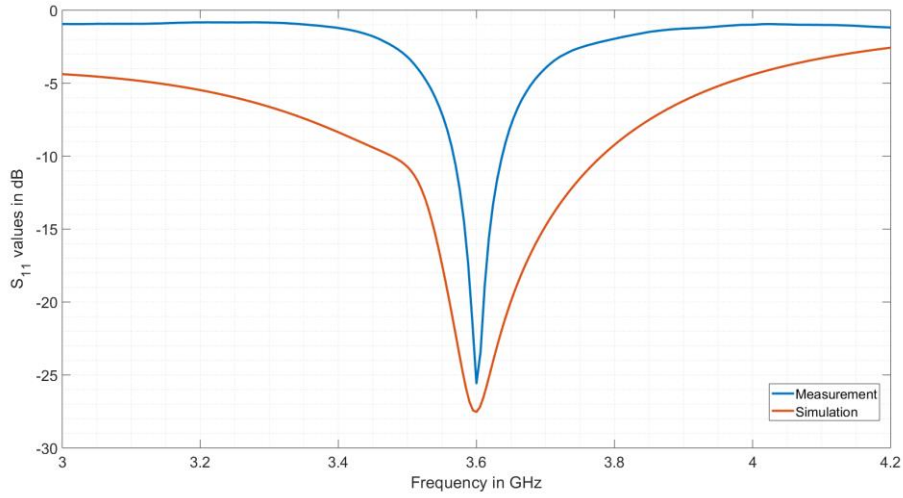


Figure 4.21: Comparison of simulated and measured S_{11} values.

As shown in Figure 4.21, the resonance frequency of the fabricated prototype is same as the simulated antenna. Simulation results cover a larger frequency band compared to the measurement. This phenomenon occurs due to the fabrication effects such as rough milling of the substrate.

Radiation pattern measurements of the fabricated antenna are done in an anechoic chamber at Microwave and Antennas Laboratory of Middle East Technical University. The measurement setup of the prototype antenna can be seen in Figure 4.22.

The comparison graphs of the radiation patterns in different main beam directions are given in Figure 4.23- Figure 4.27. The list of main beam directions when different phase differences are applied can be seen in Table 4.3. In the measurement setup illustrated in Figure 4.22, the antenna is placed in zx -plane. Therefore, radiation towards $\theta = 90^\circ$ direction corresponds the broadside radiation pattern.

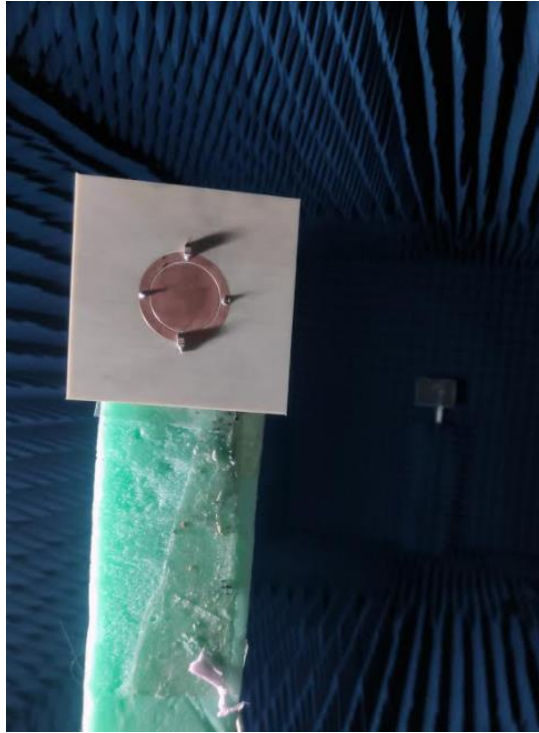


Figure 4.22 Measurement setup of the fabricated antenna.

Table 4.3: List of steered beam directions

Applied phase difference (deg)	Measured maximum radiation direction in elevation plane (deg)	Beam Steer Angle (deg)
0	130	40
30	120	30
90	111	21
120	105	15
180	90	0

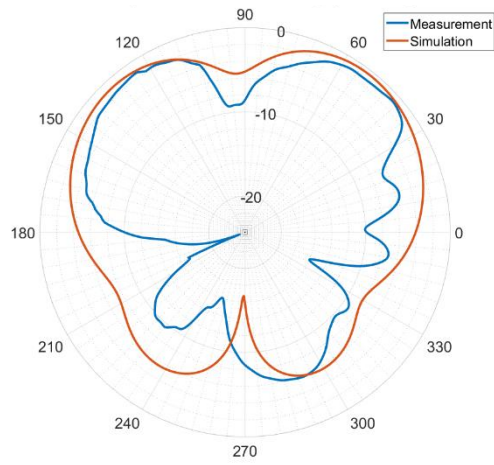


Figure 4.23: Radiation Pattern Results of the Antenna at $\phi = 0^\circ$ Plane When 0° Phase Difference is Applied.

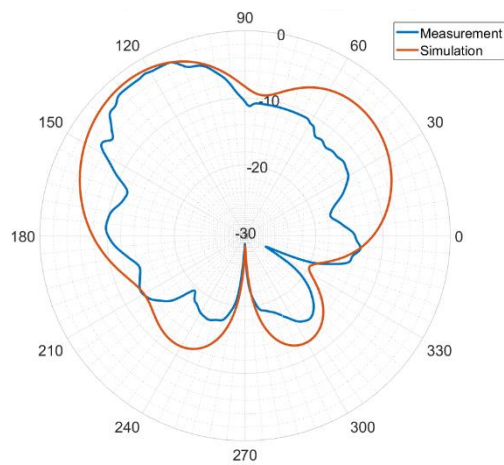


Figure 4.24: Radiation Pattern Results of the Antenna at $\phi = 0^\circ$ Plane When 30° Phase Difference is Applied.

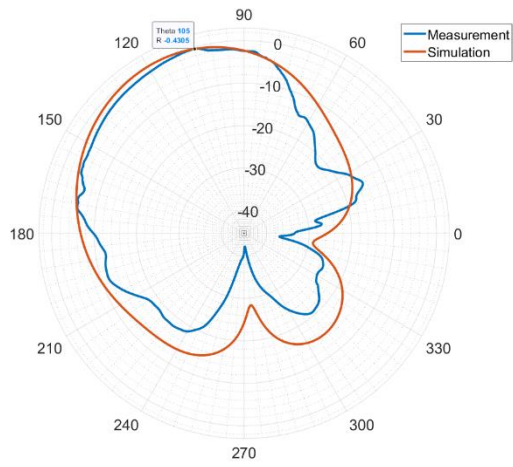


Figure 4.25: Radiation Pattern Results of the Antenna at $\phi = 0^\circ$ Plane When 90° Phase Difference is Applied.

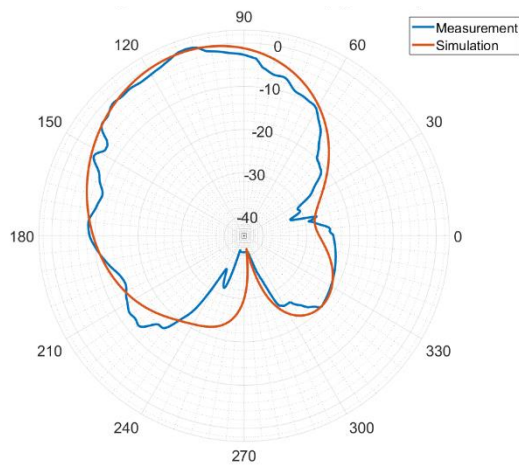


Figure 4.26: Radiation Pattern Results of the Antenna at $\phi = 0^\circ$ Plane When 120° Phase Difference is Applied.

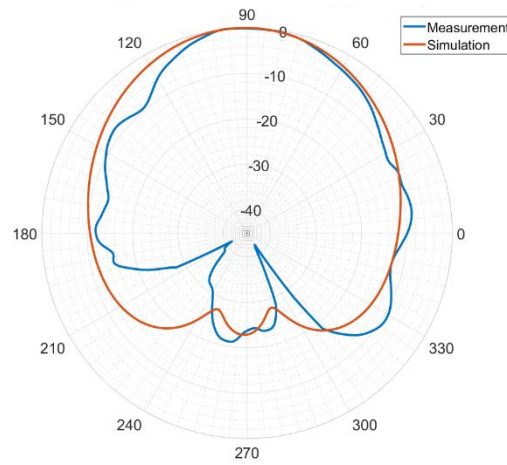


Figure 4.27: Radiation Pattern Results of the Antenna at $\phi = 0^\circ$ Plane When 180° Phase Difference is Applied.

The antenna gives linear polarization along the x-axis for all phase difference values.

When the measurement results in Figure 4.23 to Figure 4.27 are investigated, a remarkable similarity with the simulation results is observed. The maximum radiation direction of each measurement is aligned with the simulation predictions. As an error, fluctuations in the measurement results can be highlighted. These fluctuations occur due to unwanted vibrations introduced by the rotating motor of the anechoic chamber setup.

Apart from radiation pattern measurements, the gains of the antenna are measured. The measurement results and their comparison with the realized gain simulations can be seen in Table 4.4.

Table 4.4 Comparison of measured gain, simulated gain, and directivity values

	Measured Gain (dB)	Realized Gain Simulation (dB)	Directivity Simulation (dB)
Conical Beam	-3.24	-3.04	5.1
Broadside Beam	-2.85	-2.75	8.08

When the gain measurements are investigated, a close agreement between measurement and simulation results can be seen. However, due to lack of isolation, the measured gain values are significantly smaller than simulated directivity values.

4.8 Summary and Discussion

In this chapter, the ringed circular microstrip antenna is analyzed, simulated, fabricated, and measurement results are discussed. The primary purpose of this antenna is to perform radiation pattern diversity within an antenna element that is small enough to form a linear array. Different cavity mods are employed to create pattern diversity. In this study, the superposition of these TM modes is employed to create radiation pattern diversity. To excite TM_{11} and TM_{21} modes at the same frequency, the antenna requires two different resonating bodies. These resonators are selected as ring-shaped and circular patch structures. The idea of employment of different cavity modes is taken from [21]. This study only suggests the possibility of employment of TM modes individually. This thesis work introduces superposition techniques, so the study [21] is improved to create pattern diversity. Also, in this chapter antenna is improved in a physical size manner. The antenna is miniaturized to fit in an array of structures. In addition to these improvements, a large number of excitation points in [21] are reduced by parasitic excitation. Also, this chapter studies the isolation problem between its excitation ports.

The fabrication process and measurement results of the antenna are shared. Possible errors and their consequences are highlighted during the fabrication process. When the measurement results are investigated, it is seen that the measurement results of the antenna are consistent with the simulation results. Pattern reconfiguration is achieved successfully. Also, the antenna proves its capability to steer radiation beam in $-40^{\circ} < \theta < 40^{\circ}$ range. However, due to low isolation between its ports, antenna suffers from severe losses in its radiated power. As the RF power transfers between its ports due to poor isolation, radiated power reduces, and drops are observed in its realized gain. Although some methods are proposed to reduce the coupling between ports, this issue is an open research topic that needs attention as future studies.

CHAPTER 5

DESIGN AND SIMULATION OF FOUR ELEMENT COMBINED TRIANGULAR PATCH ANTENNA

In this chapter, a microstrip patch antenna that contains four sub-elements is examined. The main performance criteria of the antenna is the radiation pattern diversity, as in the slotted patch and ringed circular patch antenna designs. The proposed antenna employs four independent radiators to meet these criteria. Unlike previous designs, in this antenna, all subsections operate under fundamental cavity mode. This antenna does not rely on the different TM modes in its operation. Pattern reconfigurability is obtained thanks to the reflector behavior of the parasitic metallic structures and the array configuration of the elements.

This antenna is inspired by the study in [27]. In this study, the antenna was designed at 2.4 GHz resonance frequency by employing four different radiators. Reference study also investigates the element pattern reconfigurable antenna. In this thesis chapter, fundamental concepts illustrated in [27] are followed. However, the scanning in the reference study was limited. Array-like operations of the sub-elements enhance the pattern reconfiguring ability of the antenna. In addition to the improvement of pattern diversity, the practical implementation of the reference study is improved. As the size of the antenna given at [27] was enormous, it was impossible to employ the antenna in the linear array structures. In this thesis study, the size of the antenna is reduced by changing the feeding structure and radiator geometries.

This chapter investigates the design procedure of the antenna by illustrating different feeding and termination combinations. The chapter consists of an introductory section that illustrates the geometric structure of the antenna. This section is followed by inspections of the performance measures of the antenna. After characterizing the

antenna, antenna miniaturization techniques are introduced, and the performance of these techniques are discussed.

5.1 Antenna Structure and Performance Analysis

The designed antenna can be modeled as a combination of four triangular sub-elements. These sub-elements are connected to each other to form a square patch. As seen in Figure 5.1, each triangular sub-element is rotated 90° to obtain a square patch. Each sub-element is fed by a separate probe.

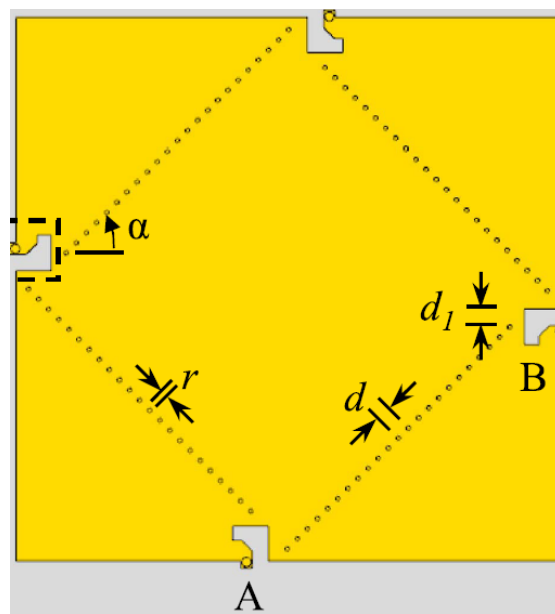


Figure 5.1 Top view of the antenna with four sub-elements in its corners [27].

5.1.1 Triangular Element

A single triangular element can be seen in Figure 5.2. The triangular part employed in the radiator is an isosceles triangle. The antenna is divided by a conducting wall that separates the antenna into two triangular parts. In this figure, the triangle on the upper hand side is the radiator, while the lower triangular part behaves like a parasitic element with reflector properties.

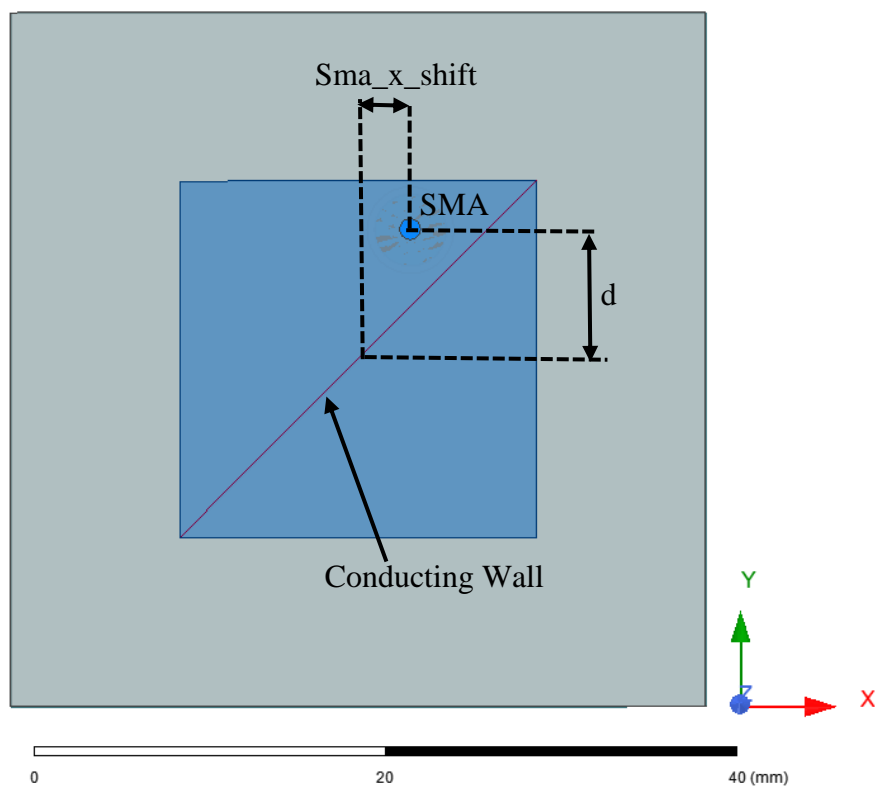


Figure 5.2 Geometry of the triangular element.

In Figure 5.2, conducting wall is soldered between the top plate of the antenna and the ground plane of the antenna. The lower triangular patch always remains as a parasitic element. Dimensions of the antenna illustrated in Figure 5.2 can be seen in

Table 5.1. The dimensions illustrated in the table are given for the optimized antenna, which radiates at 3.6 GHz.

Table 5.1 Physical dimensions of the antenna with the triangle radiator

Quantity	Dimension (in mm)
Top plate	20.5 x 20.5
Sma_x_shift	3
d	6
Substrate Size	80 x 80
Substrate Thickness	1.524
Substrate Material	Rogers 4003 ($\epsilon_r = 3.38$)

The triangular antenna has broadside radiation characteristics. The current distributions of a single triangular element and resultant radiation pattern in $\phi = -45^\circ$ plane can be found in Figure 5.3.

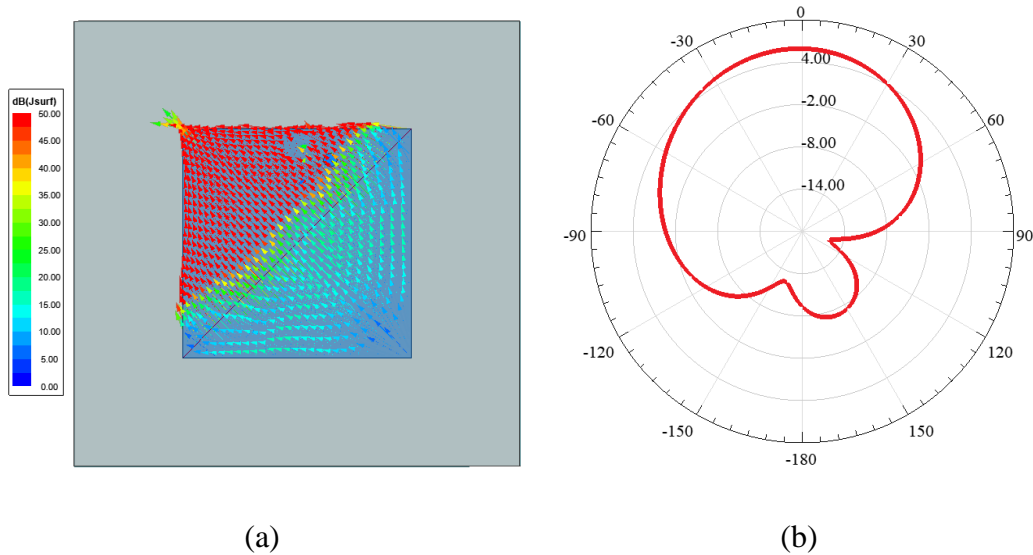


Figure 5.3 Surface current distribution (a) and radiation pattern at $\phi = -45^\circ$ plane (b) of the single triangular element.

The operation principle of the antenna can be understood by inspecting its surface current distributions. When the current distribution of the element is investigated, a shift in the radiation pattern is expected. The asymmetric current distribution results in a rotation in the radiation pattern. The behavior of the parasitic triangle as a reflector also distorts the symmetry of the radiated beam. Therefore, the radiated power is spread toward $-\theta$ direction. However, the sources of the unsymmetric pattern are not sufficient enough to steer the maximum radiation direction of the beam. Although the radiated beam is shaped towards $-\theta$ direction, the maximum radiation direction of the antenna stays at $\theta = 0^\circ$ direction (boreside).

One of the essential design considerations at the triangular element is the placement of the SMA port. The position of the SMA port has a significant impact on the current distributions on the patch in addition to its essential role in input matching. The triangular patch radiates from its edges; therefore, the surface currents are denser at the edges. A proper feeding should not distort the pronounced currents at the edge of the antenna, so the SMA port cannot be placed too close to the edges. However, placing the SMA port away from the edges causes another problem. While the port is kept away from the edges, it becomes closer to the shorting plane located diagonally in the middle. Reduction in the distance between the port and the shorting plane increases the reflections.

As the location of the port has limitations from both sides, the optimized location is determined after conducting a parametric study. The reflection coefficients when the SMA port is located at different positions can be found in Figure 5.4.

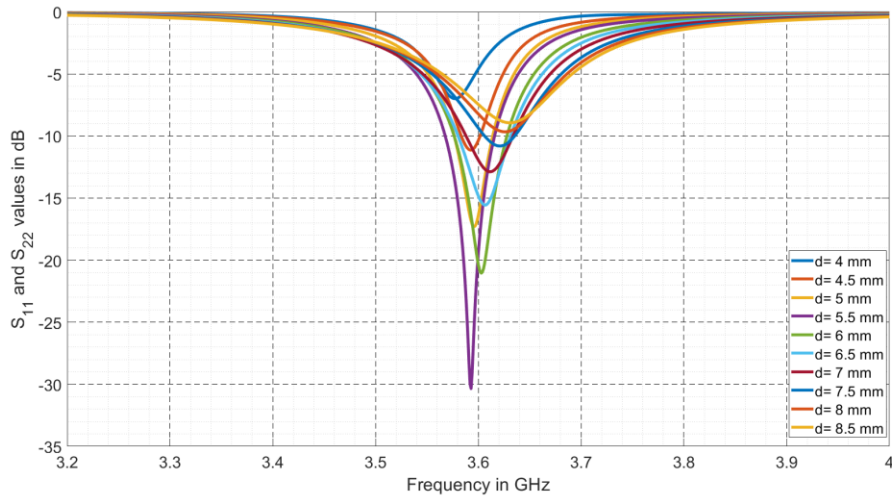


Figure 5.4 Input return loss of the triangular antenna element when the SMA port is located at different locations.

The optimal point for SMA location is found as $d=6$ mm. As shown in Figure 5.4, when the distance is increased or decreased from $d=6$ mm location, the reflections increase. This feed point is also appropriate for surface current density. Although position $d=5.5$ mm has a better S_{11} result, it causes a shift in the resonance frequency. Therefore $d=6$ mm is selected. The surface currents with this feeding location are illustrated in Figure 5.3a. As shown in this figure, the existence of the SMA port does not affect current distributions at the edges.

5.1.2 Four Element Antenna

The principal aim of this thesis is to investigate the microstrip antenna elements that possess beam steering ability with a single antenna element. In order to have pattern reconfiguration ability, the employment of multiple radiators is one of the possible options. In this part, an antenna that employs multiple radiators simultaneously will be studied. The triangular radiating element illustrated in the previous section is used

as a building block. Four of these building blocks are concatenated. In this unification process, building blocks are connected in a 90^0 rotated fashion. The resultant geometry can be seen in Figure 5.5.

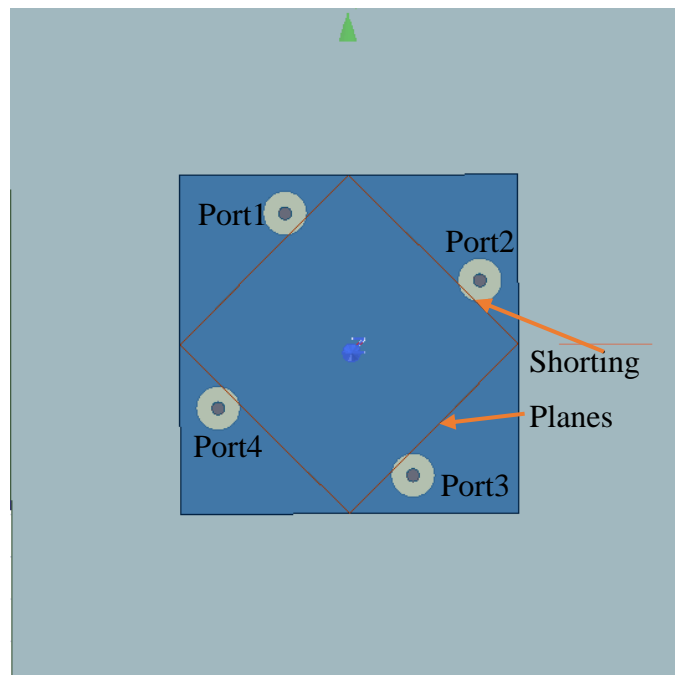


Figure 5.5 Top view of the antenna.

As can be seen from the geometry, the triangular antennas are placed so that their surface currents make 90^0 angles with respect to each other. Also, the shorting planes of sub-elements are connected to each other. This combined antenna enables the user to operate by applying different excitations while providing satisfactory isolation values between ports.

The antenna analysis procedure involves several different excitation cases. In several cases, some of the ports may not be excited. At these unused ports, matched termination is connected. Matching termination isolates the unused triangular patches and enables them to behave as a reflector type parasitic element. The radiation pattern can be investigated in four prominent cases depending on the

combinations and applied phases from the operating ports. These cases consist of operations with a single port, neighboring two ports, opposite two ports, and four ports operation.

The antenna aims to form sub-arrays or create proper constructive interferences that result in a beam steering towards the desired direction. In this operation, the reflector type behavior of the middle section also plays a role in beam steering.

5.1.2.1 Single Port Excitation

In this section, antenna performance with single port excitation is studied. As the antenna is not supported with an additional resonator, beam steering degrees would be small. Since the antenna structure is similar to a planar array, beam steering is observed at different ϕ planes.

The locations of the excited triangular patch define the radiation steering plane. The radiation pattern is steered in $\phi = 45^\circ$ or $\phi = -45^\circ$ planes depending on the excited triangle. The steered beam directions concerning excited ports are listed in Table 5.2.

Table 5.2 Main beam directions by employing different ports

Excited Ports	Plane of Beam Steering (ϕ)	Beam steering angle (θ)
1 st	$\phi = -45^\circ$	$\theta = -10^\circ$
2 nd	$\phi = 45^\circ$	$\theta = 10^\circ$
3 rd	$\phi = -45^\circ$	$\theta = 10^\circ$
4 th	$\phi = 45^\circ$	$\theta = -10^\circ$

As can be seen from Table 5.2, beam steering angles can be $\pm 10^\circ$. Since the number of active elements is one, only the reflective effect of the parasitic elements are

observed in beam steering. This effect, on its own, has the capability of 10^0 beam steering. The radiation patterns of cases that are investigated in Table 5.2 are visualized in Figure 5.6. Radiation patterns are illustrated in the $\phi = -45^0$ plane for Figure 5.6a and Figure 5.6c where, the $\phi = 45^0$ plane is employed in Figure 5.6b and Figure 5.6d.

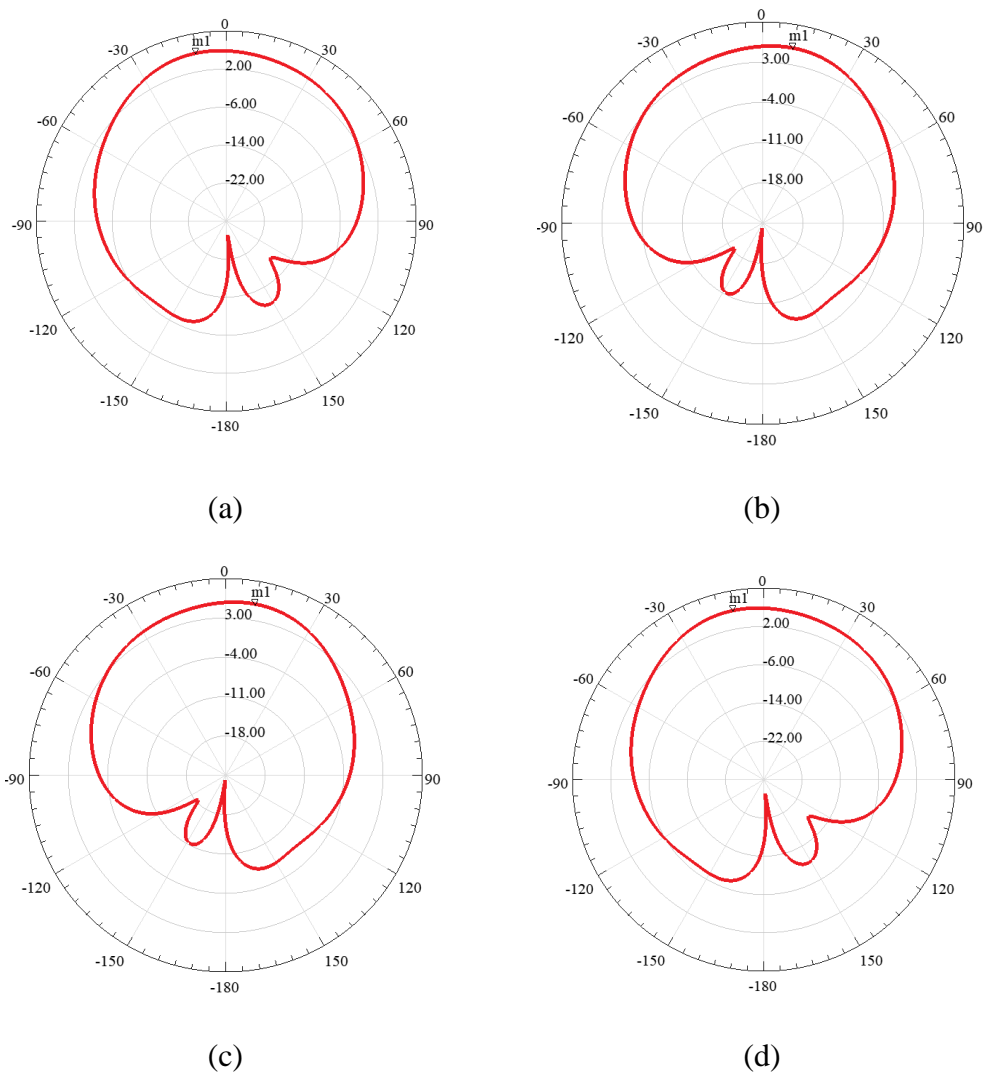


Figure 5.6 Radiation patterns of the antenna when only Port1(a), Port2(b), Port3(c), or Port4(d) is excited.

As shown in Figure 5.6, a radiation pattern that faces towards four different directions can be obtained by just exciting a single element.

5.1.2.2 Excitation of Two Neighboring Ports

When two neighboring ports are excited simultaneously with the same amplitude and phase, reconfiguration at radiation pattern is achieved. The locations of operating ports determine the radiation pattern direction. A neighboring double port excitation case enables the user to steer the beam towards higher elevation angles than a single port excitation case. However, these angles are still limited. Four possible port combination yields this type of feeding. These feeding combinations and their related main beam directions can be found in Table 5.3.

Table 5.3 Main beam directions by employing neighboring port combinations

Operating Ports	Plane of Beam Steering (ϕ)	Beam steering angle (θ)
1 st & 2 nd	$\phi = 90^0$ plane	$\theta = 15^0$
2 nd & 3 rd	$\phi = 0^0$ plane	$\theta = 15^0$
3 rd & 4 th	$\phi = 90^0$ plane	$\theta = -15^0$
4 th & 1 st	$\phi = 0^0$ plane	$\theta = -15^0$

The neighboring double port excitation technique combines two concepts to steer the radiation beam. One of these concepts can be defined by the reflector effect of the parasitic rectangle located in the middle of the antenna. The other issue that contributes to beam steering is explained by superposition. Two neighboring triangular structures create their own radiation beam. The interference of these two independent beams rotates the direction of the maximum radiated power. This effect

increases the beam steering angle compared to the single excitation cases presented in the previous part.

The illustration of the radiated fields for cases that are listed in Table 5.3 can be found in Figure 5.7. The plots in Figure 5.7 employ different ϕ planes. Figure 5.7a and Figure 5.7c visualize radiation pattern in $\phi = 90^\circ$ plane while Figure 5.7b and Figure 5.7d visualizes radiation pattern in $\phi = 0^\circ$ plane.

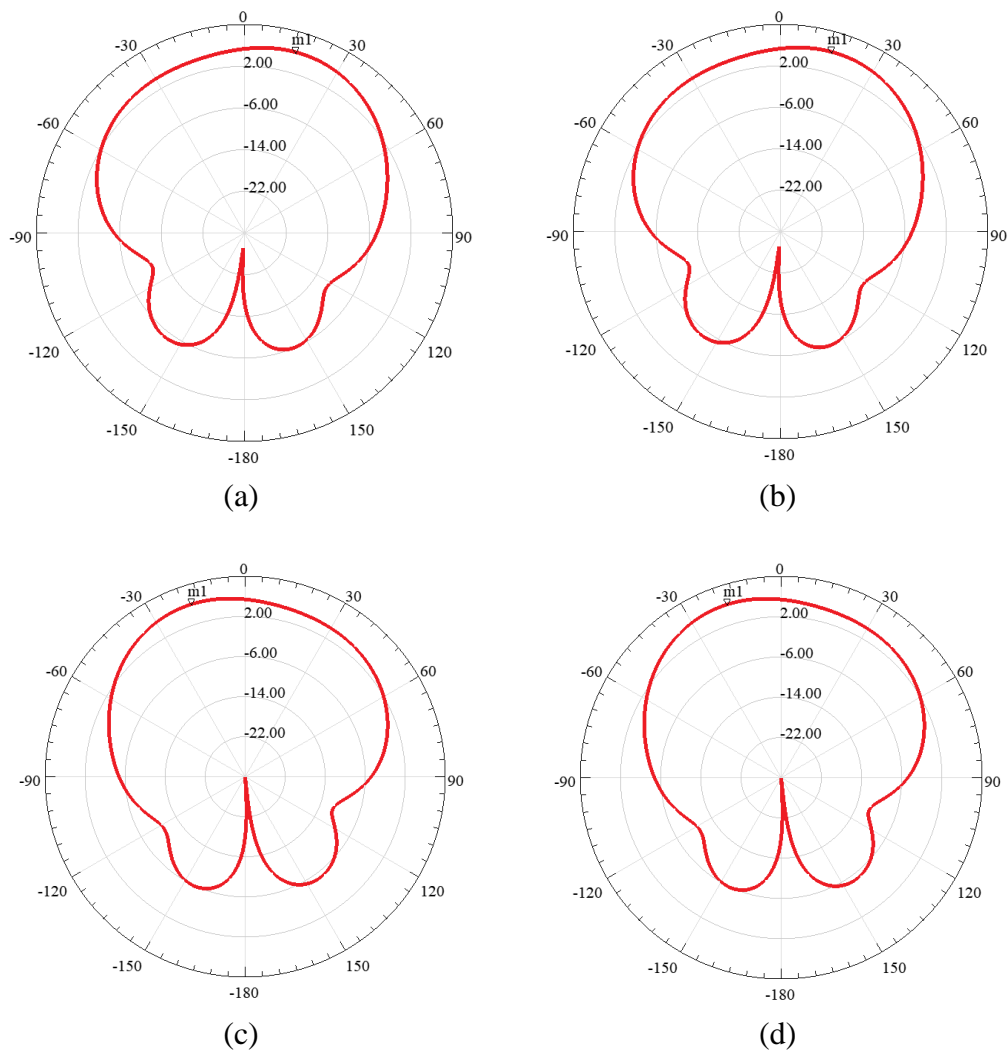


Figure 5.7 Radiation pattern at $\phi=90^\circ$ plane when ports 3 and 4 are excited.

In two ports excitation of neighboring elements, excited surface currents are orthogonal to each other with $\mp 45^\circ$ slant polarization. The superposition of these currents results in polarized fields depending on which two elements are excited. For example, when ports 1 and 2 are operated, the equivalent E-field is seen in the y-direction. So the linear polarization is observed. The polarization purity of the antenna can be understood by examining the radiation patterns of co and cross-polarized fields. The radiation patterns can be seen in Figure 5.8.

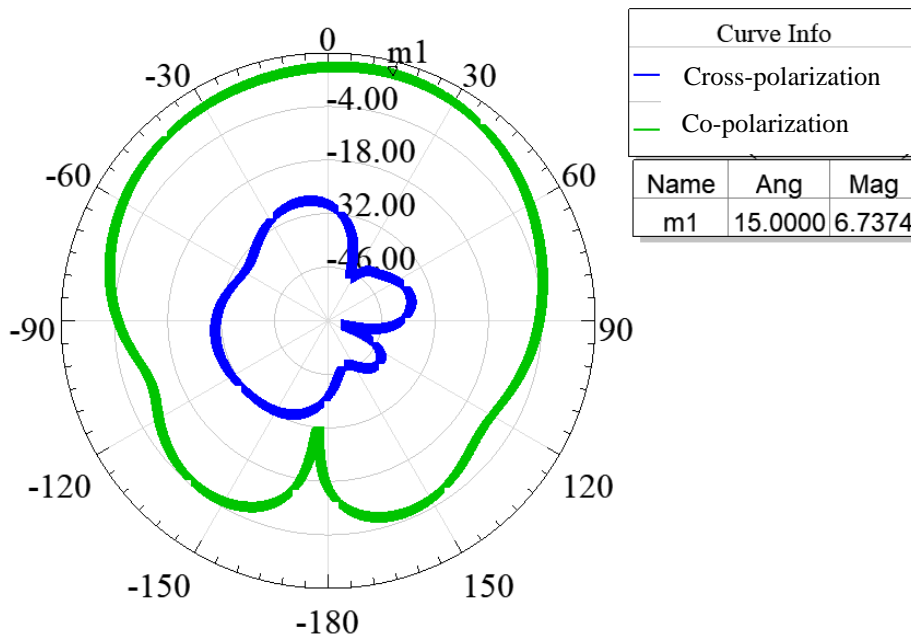


Figure 5.8 Radiation patterns of co-polarized and cross-polarized fields when ports 1 and 2 are excited.

5.1.2.3 Excitation of Opposite Two Ports

In this excitation case, the triangular elements that face each other are excited simultaneously. The radiation pattern of this feeding pair has an interesting heart shape. A heart-shaped radiation pattern refers to a deformed form of the conical beam. This radiation pattern focuses its radiation toward $\theta = 40^\circ$ for only two constant ϕ planes. (The conical beam focuses its power towards $\theta = 40^\circ$ for all ϕ values). An example of a heart-shaped pattern in the third-dimensional space (3D) can be seen in Figure 5.9.

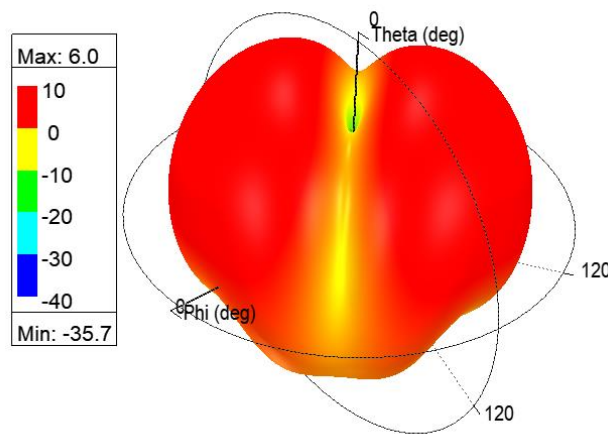


Figure 5.9 Heart shape 3D radiation pattern when ports 1&3 are fed in-phase.

In our design, when two ports that face each other are excited in-phase, the heart shape pattern occurs. This pattern yields maximum radiation at $\phi = -45^\circ$ and $\phi = 45^\circ$ cuts, depending on the selected ports. This type of feeding combination has two possibilities. These possibilities and their resultant radiation pattern directions are tabulated in Table 5.4.

Table 5.4 Main beam directions of different feed combinations

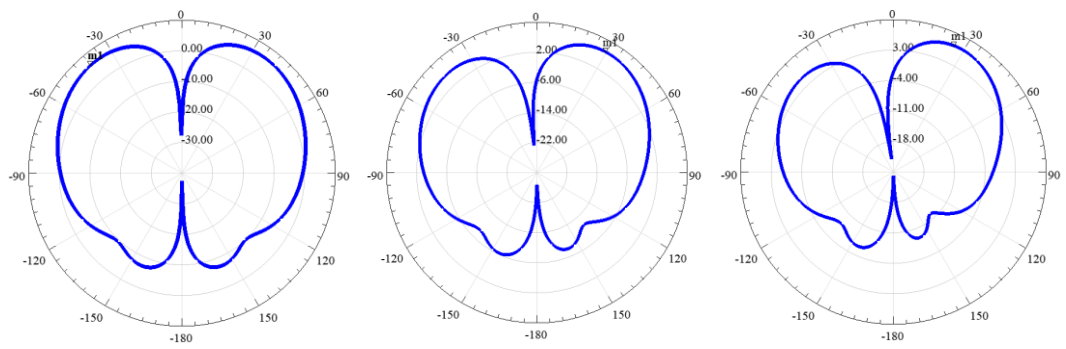
Operating Ports	Plane of Beam Steering (ϕ)	Beam steering angle (θ)
1 st & 3 rd	$\phi = -45^0$	$\theta = \pm 40^0$
2 nd & 4 th	$\phi = 45^0$	$\theta = \pm 40^0$

Apart from having a heart shape pattern, beam steering can be achieved by applying a phase difference between ports. Table 5.5 shows simulation results when ports 1 and 3 are excited with a phase difference. It can be observed that the beam can be steered from 0^0 to 40^0 .

Table 5.5 Main beam directions when different phase differences applied between ports 1 and 3

The phase difference between ports	Maximum radiation direction (at elevation)
0^0	40^0
20^0	30^0
30^0	26^0
45^0	25^0
60^0	22^0
90^0	17^0
120^0	12^0
150^0	5^0
180^0	0^0

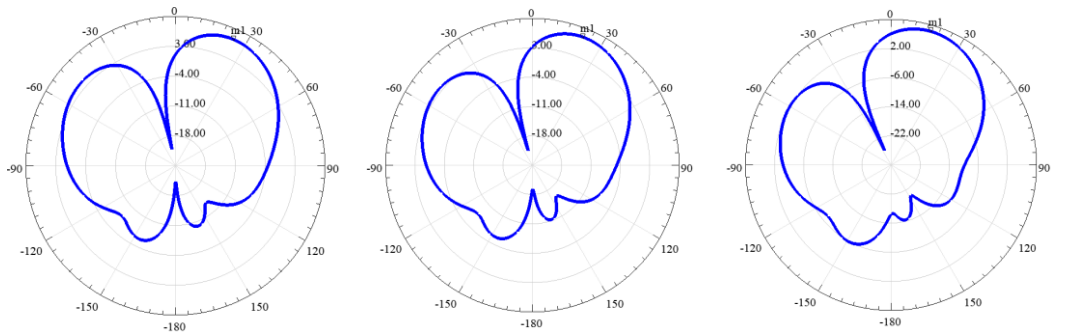
The radiation pattern at $\phi = -45^0$ plane for different phase differences can be seen in Figure 5.10. While obtaining these plots, the phase difference is applied so that port 3 lags port 1 with values given in Table 5.5. The beam is steered towards the lagging element, as array theory implies.



$\beta = 0^\circ$ (a)

$\beta = 20^\circ$ (b)

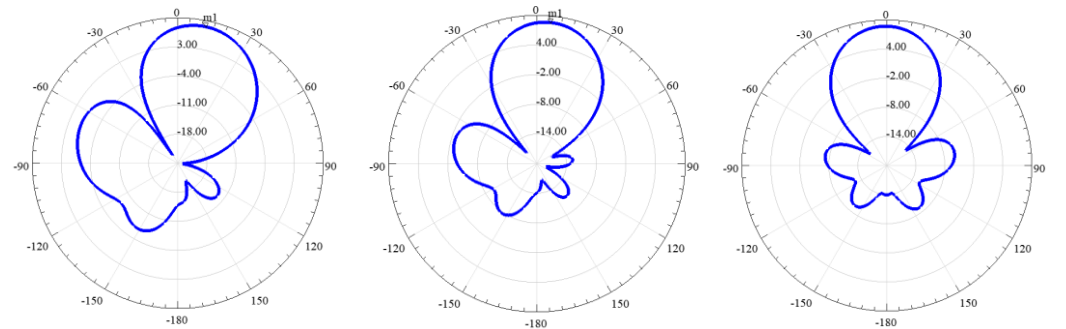
$\beta = 30^\circ$ (c)



$\beta = 45^\circ$ (d)

$\beta = 60^\circ$ (e)

$\beta = 90^\circ$ (f)



$\beta = 120^\circ$ (g)

$\beta = 150^\circ$ (h)

$\beta = 180^\circ$ (i)

Figure 5.10 Radiation patterns for different phase differences (β) 0° (a), 20° (b), 30° (c), 45° (d), 60° (e), 90° (f), 120° (g), 150° (h) and 180° (i).

5.1.2.4 Four Ports Excitation

In this feeding configuration, all triangular patches are excited simultaneously. When all ports are excited with the same amplitude and same phase, a conical beam occurs whose maximum radiation direction is $\theta = 40^\circ$ at each ϕ plane.

A different radiation pattern is obtained if a phase difference is introduced at the excitations of each port. When four ports are fed so that consecutive ports will have 90° phase difference (0, 90, 180, 270 degrees phase sequence), radiation pattern occurs at broadside direction. However, this excitation sequence changes the polarization type of the antenna. The excitation creates four current sources, which are orthogonal to each other. When 90° phase difference is applied to these elements, circular polarization is obtained. When the axial ratio (AR) of the antenna is simulated, the AR value is found as 0.3 dB.

Note that other feeding combinations like feeding three ports, using different phases at three ports, and using different phases at four ports yield unsatisfactory results in beam steering capability; thus, they are not presented.

5.1.2.5 Summary of Different Feed Structures

In this section, the design steps of the antenna and geometry of the final design are introduced. After the introduction of the geometry, different feed mechanisms were investigated. In this design, the parasitic square section in the center of the antenna plays a vital role in beam-steering. This part behaves like a parasitic element and reflects the radiated beam away from it. The antenna can achieve beam steering towards eight different directions without any phase difference application at excitations. Although the beam-steering angles are small, beam-steering ability to eight different directions gives remarkable results. The beam steering ability of the antenna allows usage of the antenna in 2D array applications.

The beam steering directions when ports are excited in-phase fashion are summarized in Figure 5.11. In this figure, yellow checks next to SMA ports determine which ports are excited, and green arrows denote the main beam direction for the corresponding excitation. It can be observed that it is possible to steer the beam in 2D.

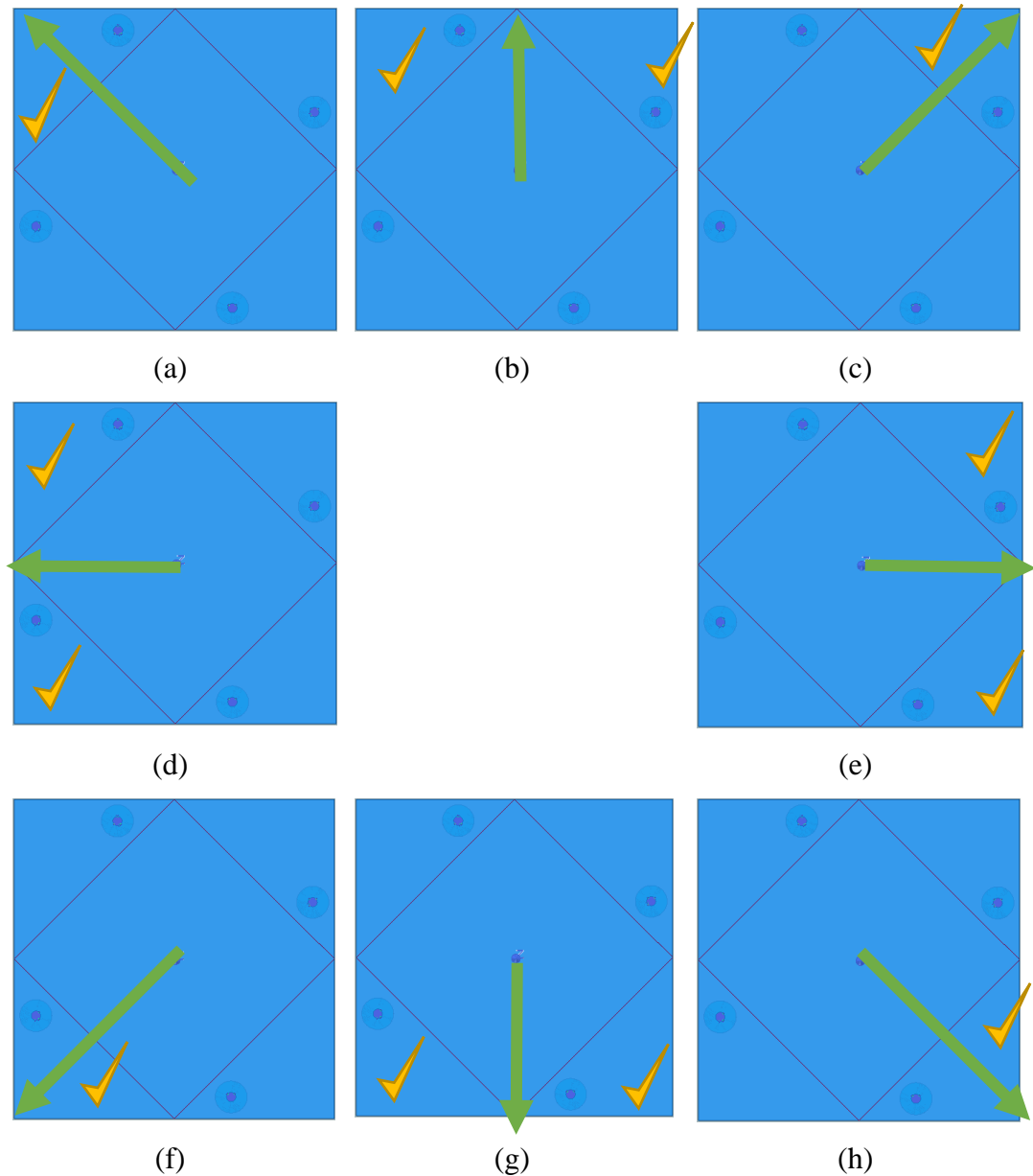


Figure 5.11 Beam steering directions when single and neighboring two ports are excited.

The main advantage of the four-element combined triangular patch antenna was operating antenna sub-sections independently. This independence is supported by the vertical conducting walls inside the substrate as the conducting wall isolates feed ports from each other. This isolation can be observed when surface current distributions of different excitations are investigated. Surface current distributions observed at different feed combinations can be seen in Figure 5.12.

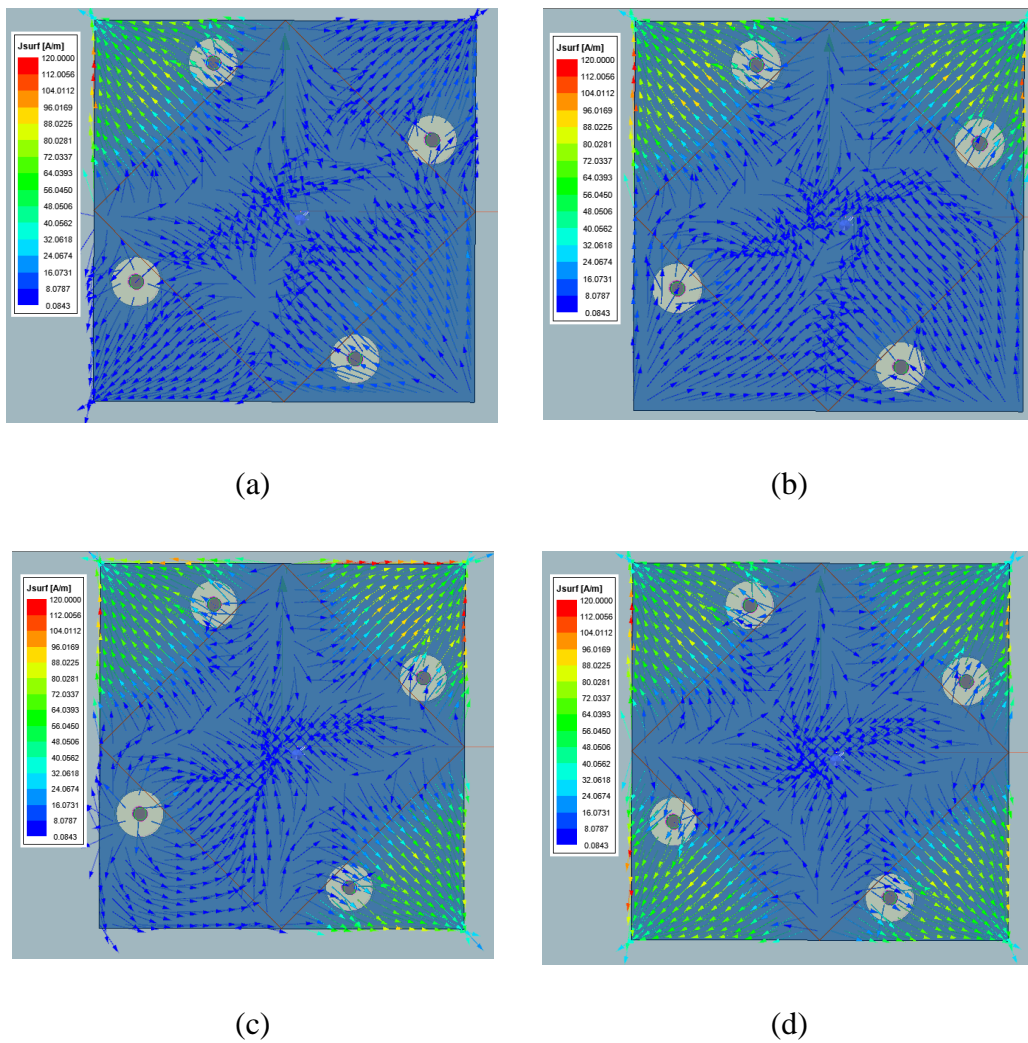


Figure 5.12 Surface current distributions when different ports are excited together; only port1 (a); ports 1&2 (b); ports 1,2 &3 (c) and all four ports (d).

As can be seen from the figures, all sub-elements operate independently without interfering with each other. The isolation between excitation ports can also be seen by inspecting S_{21} , S_{31} , and S_{41} values. The illustration of these S parameters can be seen in Figure 5.13.

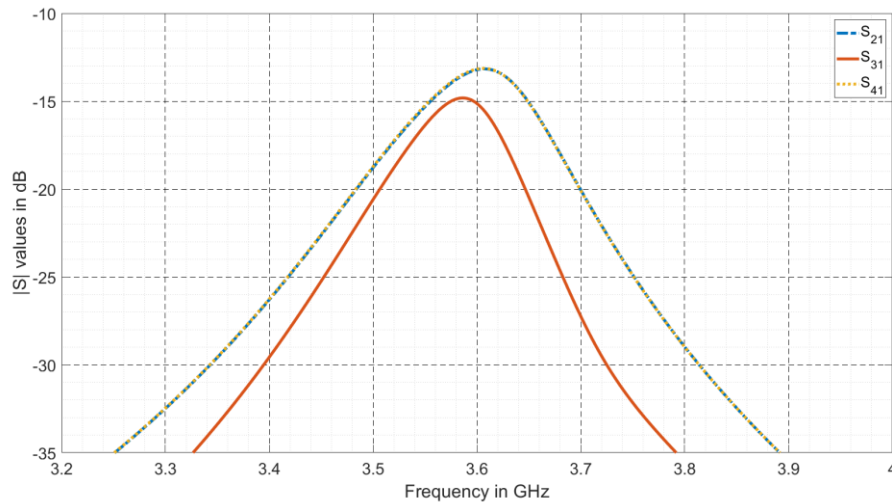


Figure 5.13 S_{21} , S_{31} , and S_{41} values of the antenna.

As can be seen in Figure 5.13, the coupling between ports are less than -10 dB. This S value is sufficient enough to model radiators as isolated and independent parts. Sine the neighboring ports are closer to each other, they tend to couple more compared to the elements facing each other. This phenomenon explains the small difference between S_{21} and S_{31} .

5.2 Antenna Miniaturization Techniques

The four triangular element patch antenna is designed to operate in array structures. To operate in a conventional array structure, the size of the antenna in the arraying direction is preferred to be smaller than $0.5\lambda_0$. When the designed antenna is measured, the length of its edge is found to be $0.48\lambda_0$ while the largest dimension of the antenna is $0.68\lambda_0$. These values prevent the formation of the array structure by employing this antenna. In order to be able to form an array structure, antenna miniaturization is a necessity. In this study, two different antenna miniaturization methods are applied to reduce its dimensions. These techniques can be presented in the following parts.

5.2.1 Miniaturizing the Inner Parasitic Rectangle

Changing the path of the surface current is one of the popular approaches concerning antenna miniaturization. Surface currents follow a path starting at conducting wall towards the opposite corner. Increasing the length of the diagonal current path results in a reduction in antenna size.

In this design, the inner square does not directly contribute to the radiation mechanism; therefore, it can be shrunk to provide more space to enlarge the antenna. To increase the antenna size, conducting walls are curved towards the origin. The curved walls provide longer current paths while keeping the parasitic properties of the inner part available. As the parasitic part still exists, the radiation pattern characteristics of the miniaturized antenna illustrate the same behavior as the non-miniaturized one. The geometry of the antenna with curved walls can be observed from the top view of the antenna illustrated in Figure 5.14.

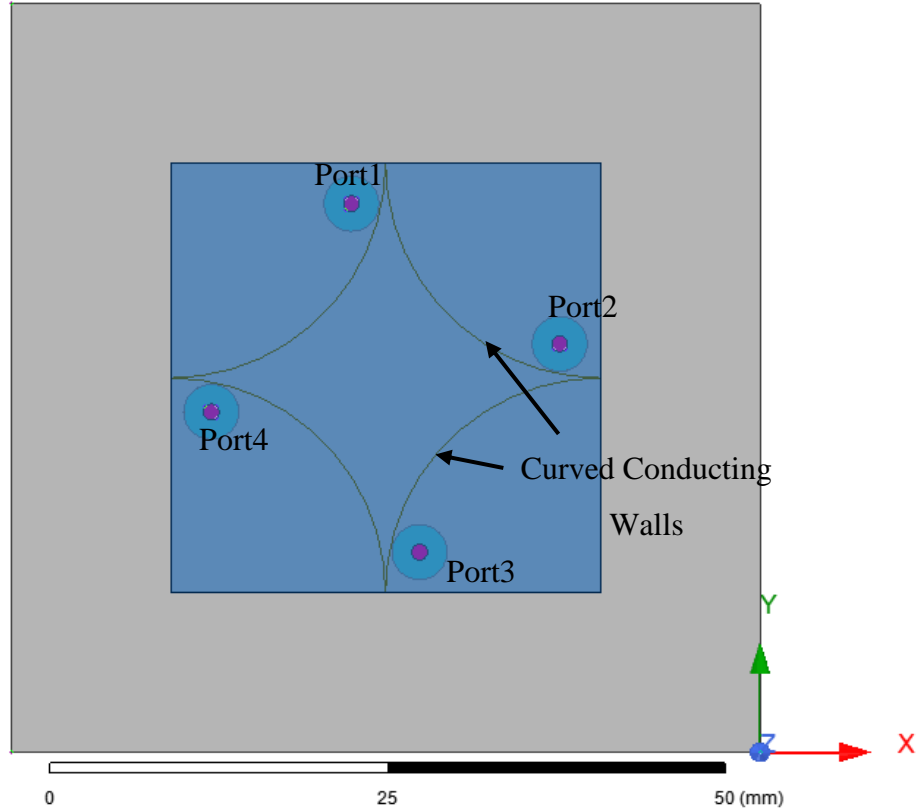


Figure 5.14 Top view of the miniaturized antenna with curved shorting plates.

The miniaturized antenna has the same operating principle as the original design. However, thanks to miniaturization, the length of this antenna is reduced to 78%.

Although the idea behind this reduction mechanism holds, there is a drawback to this mechanism. When the conducting plates are placed in a curved manner, the radiating sub-elements start interacting. This behavior can be understood by investigating the current distributions of the patch. The surface current distributions of different feed combinations are given in Figure 5.15. In these simulations, the unused ports are connected to 50 Ohm.

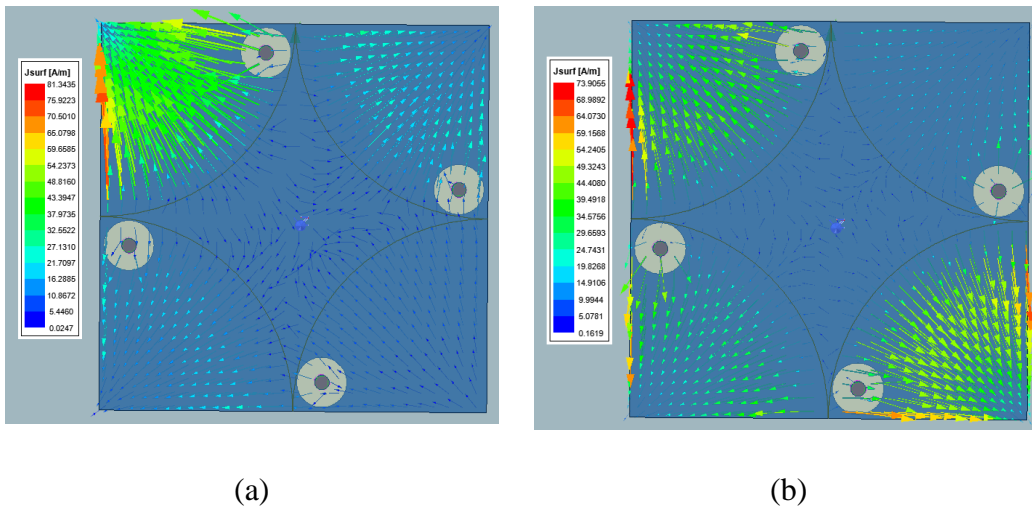


Figure 5.15 Surface current distributions when port1 (a) and port 1&3 (b) are excited.

As the sub-elements interact with each other, residual currents are induced at neighboring sub-elements. This coupling results in reductions in radiation efficiencies. The coupling can also be observed by inspecting scattering parameters between two neighboring ports. The S_{21} characteristic of the miniaturized antenna is compared with the original antenna in Figure 5.16.

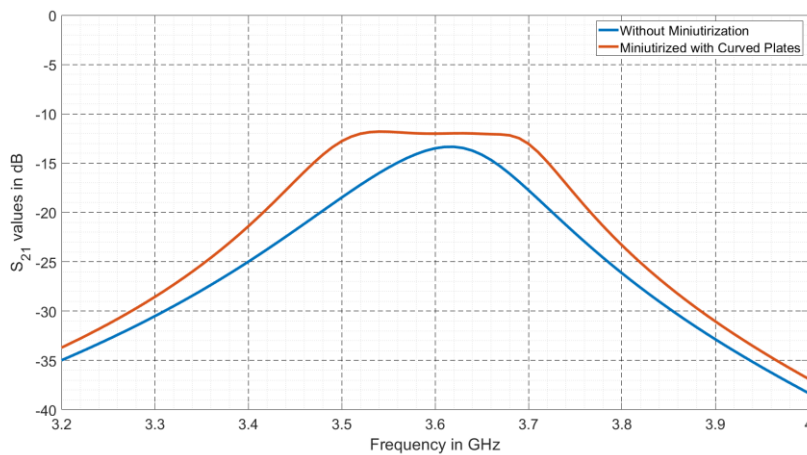


Figure 5.16 S_{21} Plots of the non-miniaturized and miniaturized antenna with curved planes.

As seen in Figure 5.16, the S_{21} value is increased by 2 dB when miniaturization is applied. Apart from the magnitude change in the S_{21} , its frequency behavior also changes. In the miniaturized antenna, the coupling is observed at a broader band compared to the original antenna. The shape of the shorting plane can explain this behavior. In the previous design, there was a larger separation between two shorting planes; therefore, it was more difficult for the currents to reach the neighboring radiator.

In order to minimize interaction between radiating elements, maximum current paths are investigated. It is found that maximum current leakage occurs from the edges of the rectangular patch. To prevent leakage, small rectangular slots are etched from the edges at the interference with the neighboring sub-elements. The resultant patch and its current distribution under one port excitation can be seen in Figure 5.17. When the structure in Figure 5.17 is compared with the structure in Figure 5.15, a reduction of induced surface currents at neighboring radiators can be seen.

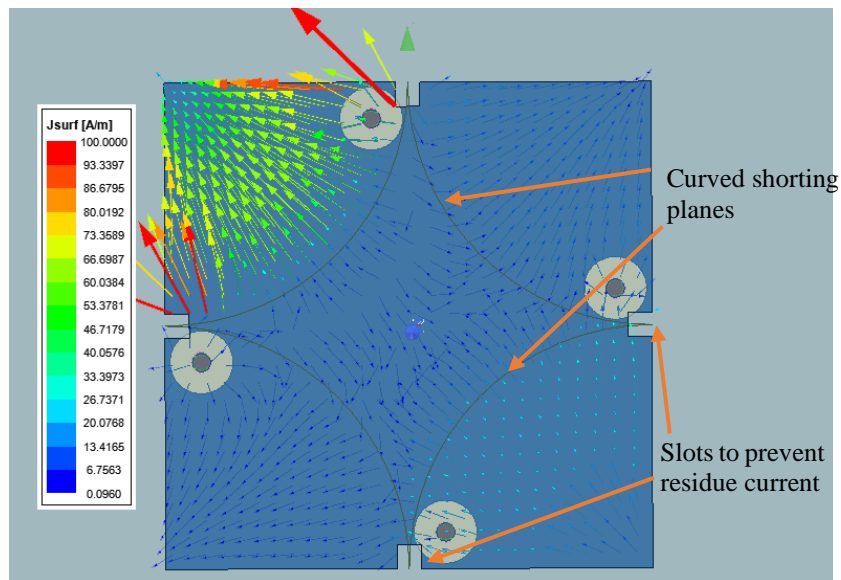


Figure 5.17 Surface current distributions when only port 1 is excited.

The reduction of the coupling between ports can also be understood by inspecting the S_{21} parameters of the antenna. In Figure 5.18, the comparison of the S_{21} values can be seen. As shown in the figure, the larger coupling is reduced by etching slots, and S_{21} values illustrate the same values with the non-miniaturized antenna at the resonance frequency.

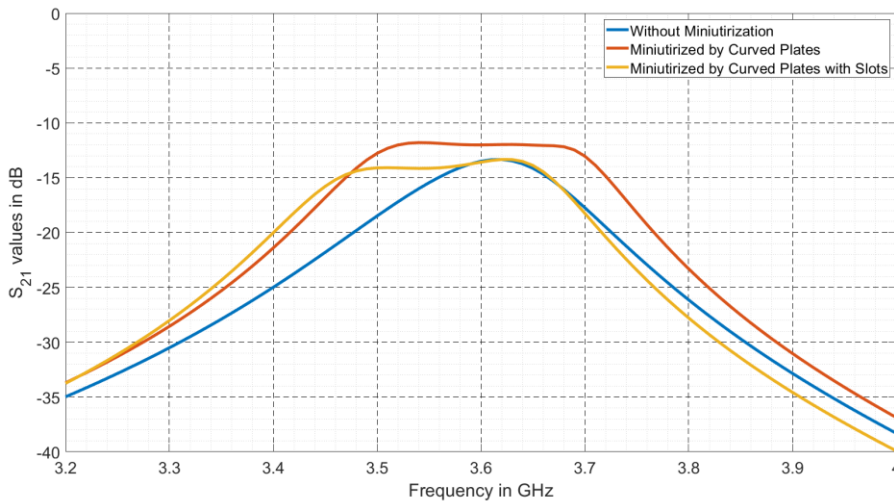


Figure 5.18 S_{21} plots of the non-miniaturized, miniaturized antenna with curved planes and miniaturized antenna with slot application.

The antenna with curved conductor walls, illustrated in Figure 5.17, can be evaluated as a miniaturized version of the antenna discussed in the previous section. This antenna provides same radiation characteristics as the non-miniaturized antenna. The radiation patterns of the miniaturized antenna are same as the non-miniaturized one. The reflection parameters of the miniaturized antenna can be found in Figure 5.20. This miniaturization technique reduced the largest dimension of the antenna to $0.51\lambda_0$ while the dimension of the antenna length reduces to $0.38\lambda_0$. These reduced dimensions enables designer to use this antenna in a conventional linear array structure.

5.2.2 Slot Employment

This method reduces antenna size by increasing the path that is traveled by the surface currents. This method changes the linear path of the current to a curved path; therefore, it increases the path length that the current travels. The top view and surface currents for port1 excitation case can be seen in Figure 5.19. Unlike the previous method, slot employment does not change the parasitic element's shape that is located in the middle of the antenna.

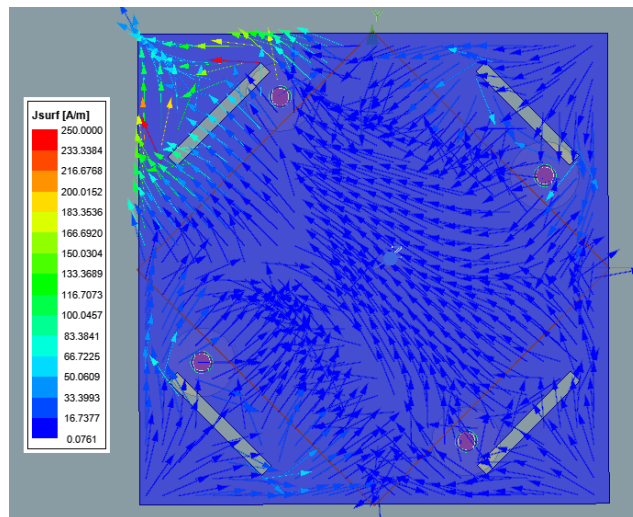


Figure 5.19 Top view of the antenna with slot and the surface current distribution when only port 1 is excited.

This method requires slot etching at each of the radiating elements. Slots will be perpendicular to the current direction to provide longer current paths, as seen in Figure 5.19. By this method, the maximum dimension of the antenna is reduced to $0.57\lambda_0$ while its length is reduced to $0.42\lambda_0$. As the miniaturization ratio is smaller than the previous method, the slot employment method may not be preferred as a single application. This miniaturized antenna also has the same pattern reconfiguring capabilities as the non- miniaturized antenna. As this structure employs shorting

walls in a linear shape, it has the same isolation performance as the original antenna. Therefore, the coupling between ports is not an issue as in the previous miniaturization technique.

The original antenna and its miniaturized versions have a resonance at 3.6 GHz frequency. This resonance behavior can be understood by inspecting the S_{11} values given in Figure 5.20.

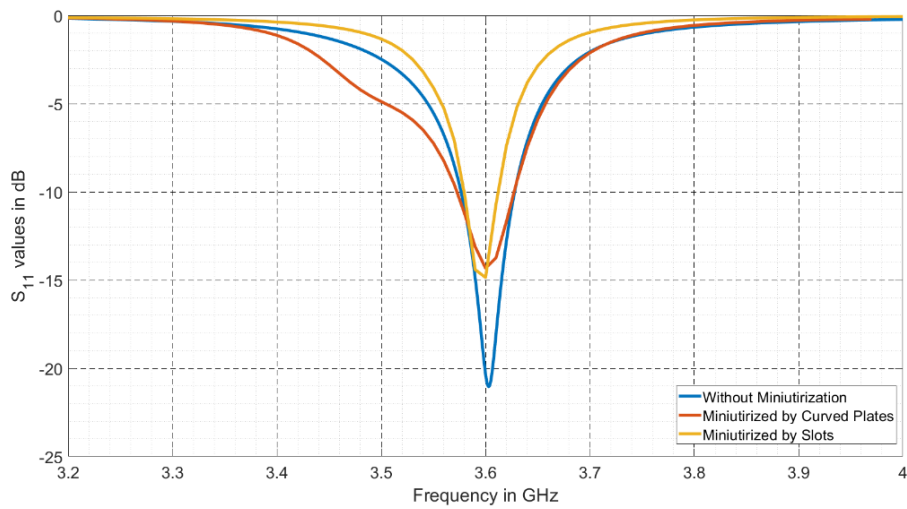


Figure 5.20 S_{11} parameters of original and miniaturized antenna designs.

5.3 Summary and Discussions

The antenna that combines four triangular microstrip patch structures is a successful pattern reconfigurable antenna candidate. This antenna introduces beam steering ability in different ϕ planes. Therefore, this antenna can be employed in 2D beam steering.

The geometry of the antenna is inspired by [27]. At that study, a four-element antenna was studied. The differences between the antenna studied in this chapter and [27] can be listed as feeding structure, isolation of the sub-elements, antenna miniaturization, and operating frequency. As the thesis work is concentrated on the sub-6 GHz band of the 5G protocol, the resonance frequency of the antenna is selected as 3.6 GHz. As the operation frequency increases, the size of the antenna is reduced; therefore, the fancy feeding structure illustrated at [27] changed to coaxial probe-type feeding. In [27], multiple vias are employed to provide isolation between triangles. This solution is converted to the conducting walls in our design. The conductor wall design is chosen as it can be shaped to provide antenna miniaturization. The curved conduction wall increases the surface area of the triangular patch; therefore, it increases the length of the radiating surface currents. This phenomenon reduces the size of the antenna element. Another improvement on the antenna is made at enhanced isolation between neighboring triangular radiators. After applying the miniaturizing techniques, the excitation ports of the antenna become closer to each other. Reduction in geometrical separation increases the coupling between triangular radiators. This coupling phenomenon is prevented by the introduction of the rectangular slots on the patch.

In the study [27], the operating frequency is selected as 2.4 GHz. This frequency band results in a larger antenna and also larger parasitic elements. The beam steering performance of the [27] is slightly more successful than the design illustrated in this chapter when only one port is excited. The large size of the parasitic elements can explain the differences at the scan angles when only one port is excited.

When the simulation results are investigated, a small beam steering angle is observed when only a single port is excited. In this case, the parasitic structures are responsible for rotation in the beam. As the radiator and parasitic reflector parts are close to each other, beam steering can only be achieved in small degrees. The excitation of two ports provides more satisfying results at steered beam angles. When two neighboring elements are excited simultaneously, the beam is steered towards $\theta = 15^\circ$ direction.

The beam steering performance of the antenna can be further enhanced by exciting opposite ports. This excitation combination provides larger scan angles. When the antenna is excited by opposite ports, the radiation pattern becomes heart-shaped. This heart-shaped radiation pattern occurs due to the parasitic elements.

When different phase differences are applied from excitations, pattern diversity is obtained. Depending on the phase shift between excitations, the radiation pattern can be scanned between $\pm 40^\circ$ in elevation.

Another operation mode of the triangular patch antenna is observed when all the feed ports are excited simultaneously. In this configuration, the parasitic effect of the antenna is minimized as four of the triangles are excited. As the parasitic effect is reduced, the radiation pattern of the antenna occurs in a conical beam fashion. In this feeding system, if a progressive 90° phase shift is applied from ports, radiation at broadside can be achieved. When all the array elements have the same phase of excitation, the fields radiated by opposite sub-elements cancel each other at broadside direction; so the conical beam occurs. However, when the elements are excited with 90° phase difference, the opposite elements would be out of phase, this time a constructive interference will be observed at broadside direction; so radiated beam will be in broadside. However, broadside operation provides circular polarization, while all the other operations achieve linear polarization.

CHAPTER 6

CONCLUSIONS AND FUTURE WORKS

Throughout the thesis study, pattern reconfigurable antennas that have the capability to steer their main beam are discussed. The primary motivation is to overcome the gain reduction in the conventional array structures in large scan angles. The gain reduction at large scan angles is tried to be balanced by rotating the maximum radiation direction of the array element towards the scan direction. This application requires an antenna element that has pattern reconfiguration ability.

The antennas covered in the scope of this thesis operate at 3.6 GHz. This operating frequency is selected to meet the demands of the sub-6GHz region of the 5G protocol.

The antennas covered in the thesis are single-layered microstrip type antennas. The microstrip antenna's low profile structure makes it a good candidate. Also, having a planar structure makes the fabrication process to be inexpensive and practical. Because of these benefits, the microstrip structure is selected.

Pattern reconfigurability means the ability to steer the radiation beam of the antenna towards different directions. As the study mainly focuses on linear arrays, the scan angle at $\phi = 0^\circ$ plane is prioritized. Several different ideas are studied on microstrip antennas to achieve pattern reconfigurability. One of these ideas is employing even and odd modes of the rectangular patch antennas. This antenna is a modified version of a rectangular patch antenna. A shorting wall is soldered in the middle section of the antenna. Therefore, it is divided into two independent portions. By exciting these portions separately, different mods can be observed. In these modes, the rectangular antenna is excited so that the E-field beneath its top plate has two different

distributions, which may be in-phase or out of phase manner. Depending on the E-field distribution, the main beam occurs in broadside direction or in conical beam shape. These two radiation patterns illustrate the range of the element pattern scan capability. By arranging phase difference between excitations, the antenna operates in an intermediate mode that cannot be named either even or odd. This intermediate mode can be modeled as a superposition of the even and odd mode operations with different weights. Therefore, by applying the phase difference between excitations, multiple steering angles can be achieved.

Another design that governs pattern reconfigurability includes multiple resonators. The resonators that are used in this study are circular disk and ring-shaped patch structures. These resonators do not have direct contact, but they are placed close so that they induce current on each other. Thanks to this phenomenon, only the ring-shaped patch antenna is connected to the ports. Radiators are placed in a concentric manner. Dimensions of the resonators are arranged so that the circular patch operates in TM_{11} mode while the ring-shaped patch operates at TM_{21} mode. These different cavity modes yield different radiation beams, which are in broadside direction and in conical beam shape. Like the first design, this design also requires a phase difference between its excitation ports. Applied phase difference combines radiation characteristics of TM_{11} and TM_{21} modes. This operation phenomenon enables beam scanning between -40° and $+40^\circ$ from the broadside.

Two designs mentioned above are fabricated and measured. Reflection coefficient, radiation pattern, and gain measurements are taken from the fabricated prototypes. The measurement results of the rectangular shorted patch antenna and ringed circular patch antenna illustrate a remarkable agreement with the simulation values.

The final design explained in the thesis operates with pattern reconfigurability ability in two-dimensional space. The antenna is a combination of the four sub-elements. The sub-elements are in a triangular shape with their hypotenuse shorted by conducting walls.

The antenna is formed when four of these triangular elements are connected such that they are rotated 90° with respect to each other. Therefore its beam scanning capabilities are not limited to a single plane. The antenna can steer its beam in 2D. This antenna employs the superposition of different sub-elements to steer its beam. A two-element array operation can explain the beam steering performance. To operate array structure, different phase differences are employed from excitation ports. As in the case of previous designs, this antenna can scan angles between -40° and $+40^{\circ}$ from the broadside.

As future work, the antenna illustrated in Chapter 4 can be improved. This antenna suffers poor isolation performance between ports. Due to the coupling between excitation ports, a considerable amount of input power is not radiated, which reduces the realized gain values of the antenna. As a future work, the coupling between excitations can be studied.

REFERENCES

- [1] ‘Why Do We Need 5G?’ “<https://www.etsi.org/technologies/5g>.” <https://www.etsi.org/technologies/5g> (accessed Jan. 12, 2021).
- [2] ‘What Frequency Spectrum Will 5G Technology Use?’ “<https://www.arrow.com/en/research-and-events/articles/what-frequency-spectrum-will-5gtechnology-use-and-how-does-this-compare-to4g#:~:text=The%205G%20frequency%20band%20plans,GHz%20to%2086%20GHz%20range.>” .
- [3] C.A.Balanis, *Antenna Theory: analysis and design*, 3rd ed. Wiley-Interscience, 2005.
- [4] S. Zhang, G. H. Huff, J. Feng, and J. T. Bernhard, “A pattern reconfigurable microstrip parasitic array,” *IEEE Transactions on Antennas and Propagation*, vol. 52, no. 10, pp. 2773– 2776, Oct. 2004, doi: 10.1109/TAP.2004.834372.
- [5] F. Lm Luo, S. Preston, D. Thiel, J. Lu, and T. Bird, “Electronic beam steering using switched parasitic patch elements,” 1996.
- [6] Y. Cao, Y. Cai, W. Cao, Z. Qian, and L. Zhu, “Wideband microstrip patch antenna loaded with parasitic metal strips and coupling slots,” 2018, doi: 10.1109/JPROC.
- [7] C. D. Erbas, “Parametric Analysis of Angular Rotation for Microstrip Patch Antenna with Elliptical Patch and Parasitic Elements,” Jun. 2020, doi: 10.1109/ICECCE49384.2020.9179237.
- [8] L. Sun, G. X. Zhang, B. H. Sun, W. D. Tang, and J. P. Yuan, “A Single Patch Antenna with Broadside and Conical Radiation Patterns for 3G/4G Pattern Diversity,” *IEEE Antennas and Wireless Propagation Letters*, vol. 15, pp. 433–436, 2016, doi: 10.1109/LAWP.2015.2451132.

- [9] S. Liu, W. Wu, and D. G. Fang, "Wideband monopole-like radiation pattern circular patch antenna with high gain and low cross-polarization," *IEEE Transactions on Antennas and Propagation*, vol. 64, no. 5, pp. 2042–2045, May 2016, doi: 10.1109/TAP.2016.2536418.
- [10] N. Nguyen-Trong, L. Hall, and C. Fumeaux, "A dual-band dual-pattern frequencyreconfigurable antenna," *Microwave and Optical Technology Letters*, vol. 59, no. 11, Nov. 2017, doi: 10.1002/mop.30815.
- [11] N. Nguyen-Trong, L. Hall, and C. Fumeaux, "A frequency- and pattern-reconfigurable centershorted microstrip antenna," *IEEE Antennas and Wireless Propagation Letters*, vol. 15, pp. 1955–1958, 2016, doi: 10.1109/LAWP.2016.2544943.
- [12] X. Jiang, Z. Zhang, Y. Li, and Z. Feng, "A novel null scanning antenna using even and odd modes of a shorted patch," *IEEE Transactions on Antennas and Propagation*, vol. 62, no. 4, pp. 1903–1909, 2014, doi: 10.1109/TAP.2014.2298884.
- [13] S. H. Chen, J. S. Row, and K. L. Wong, "Reconfigurable square-ring patch antenna with pattern diversity," *IEEE Transactions on Antennas and Propagation*, vol. 55, no. 2, pp. 472–475, Feb. 2007, doi: 10.1109/TAP.2006.889950.
- [14] J. Liu, Q. Xue, H. Wong, H. W. Lai, and Y. Long, "Design and analysis of a low-profile and broadband microstrip monopolar patch antenna," *IEEE Transactions on Antennas and Propagation*, vol. 61, no. 1, pp. 11–18, 2013, doi: 10.1109/TAP.2012.2214996.
- [15] X. Tong, C. Liu, X. Liu, H. Guo, and X. Yang, "Switchable ON-/OFF-Body Antenna for 2.45 GHz WBAN Applications," *IEEE Transactions on Antennas and Propagation*, vol. 66, no. 2, pp. 967–971, Feb. 2018, doi: 10.1109/TAP.2017.2780984.

- [16] I. Lim and S. Lim, "Monopole-Like and boresight pattern reconfigurable antenna," *IEEE Transactions on Antennas and Propagation*, vol. 61, no. 12, pp. 5854–5859, 2013, doi: 10.1109/TAP.2013.2283926.
- [17] W. Lin, H. Wong, and R. W. Ziolkowski, "Wideband Pattern-Reconfigurable Antenna with Switchable Broadside and Conical Beams," in *IEEE Antennas and Wireless Propagation Letters*, Aug. 2017, vol. 16, pp. 2638–2641, doi: 10.1109/LAWP.2017.2738101.
- [18] Ó. Quevedo-Teruel and E. Rajo-Iglesias, "Design of short-circuited ring-patch antennas working at TM₀₁ mode based on neural networks," *IEEE Antennas and Wireless Propagation Letters*, vol. 5, no. 1, pp. 559–562, 2006, doi: 10.1109/LAWP.2006.889559.
- [19] J. S. Row and Y. J. Huang, "Reconfigurable Antenna with Switchable Broadside and Conical Beams and Switchable Linear Polarized Patterns," *IEEE Transactions on Antennas and Propagation*, vol. 66, no. 7, pp. 3752–3756, Jul. 2018, doi: 10.1109/TAP.2018.2820325.
- [20] K. Wei, Z. Zhang, W. Chen, and Z. Feng, "A novel hybrid-fed patch antenna with pattern diversity," *IEEE Antennas and Wireless Propagation Letters*, vol. 9, pp. 562–565, 2010, doi: 10.1109/LAWP.2010.2051402.
- [21] T. Q. Tran and S. K. Sharma, "Radiation characteristics of a multimode concentric circular microstrip patch antenna by controlling amplitude and phase of modes," *IEEE Transactions on Antennas and Propagation*, vol. 60, no. 3, pp. 1601–1605, Mar. 2012, doi: 10.1109/TAP.2011.2180305.
- [22] Q. Hou, C. Li, G. Sun, and X. Zhao, "Effective Magnetic-Loop Array Antennas with Enhanced Bandwidth," *IEEE Transactions on Antennas and Propagation*, vol. 64, no. 8, pp. 3717–3722, Aug. 2016, doi: 10.1109/TAP.2016.2570806.

- [23] S. J. Shi and W. P. Ding, "Radiation pattern reconfigurable microstrip antenna for WiMAX application," *Electronics Letters*, vol. 51, no. 9, pp. 662–664, Apr. 2015, doi: 10.1049/el.2015.0568.
- [24] A. Pal, A. Mehta, D. Mirshekar-Syahkal, P. Deo, and H. Nakano, "Dual-Band low-profile capacitively coupled beam-steerable square-loop antenna," *IEEE Transactions on Antennas and Propagation*, vol. 62, no. 3, pp. 1204–1211, 2014, doi: 10.1109/TAP.2013.2294866.
- [25] G. M. Zhang, J. S. Hong, B. Z. Wang, G. Song, and P. Li, "Design and time-domain analysis for a novel pattern reconfigurable antenna," *IEEE Antennas and Wireless Propagation Letters*, vol. 10, pp. 365–368, 2011, doi: 10.1109/LAWP.2011.2146225.
- [26] H.-W. Yu, Y.-C. Jiao, D.-Y. Li, and Z.-B. Weng, "A TM₃₀ -/TM₄₀ -Mode PatternReconfigurable Microstrip Patch Antenna for Wide Beam Coverage," *IEEE Transactions on Antennas and Propagation*, vol. 67, no. 11, Nov. 2019, doi: 10.1109/TAP.2019.2930131.
- [27] A. Pal, A. Mehta, D. Mirshekar-Syahkal, and H. Nakano, "A Twelve-Beam Steering LowProfile Patch Antenna with Shorting Vias for Vehicular Applications," *IEEE Transactions on Antennas and Propagation*, vol. 65, no. 8, pp. 3905–3912, Aug. 2017, doi: 10.1109/TAP.2017.2715367.
- [28] R.Garg, P.Bhartia, I.J.Bahl, and A.Ittipiboon, *Microstrip Antenna Design Handbook*. Artech House, 2001.
- [29] Bancroft Randy, *Microstrip and Printed Antenna Design*, 2nd ed. Scitech, 2009.